EVOLUTION OF MOLYBDENUM DISULFIDE ON METAL SURFACES

A Dissertation

by

FANGLUE WU

Submitted to the Office of Graduate and Professional Studies of
Texas A&M University
in partial fulfillment of the requirements for the degree of

DOCTOR OF PHILOSOPHY

Chair of Committee,	James D. Batteas
Committee Members,	Karen L. Wooley
	Sarbajit Banerjee
	Xiaofeng Qian
Head of Department,	Ibrahim Karaman

May 2021

Major Subject: Materials Science and Engineering

ABSTRACT

Molybdenum disulfide (MoS_2) has attracted tremendous attention over the past decade due to their exciting mechanical, electronic and frictional properties. Heterostructures of semiconductors and metals are the fundamental components of modern electronics. The atomically thin MoS_2 sheets, offer unique opportunities for heterostructure devices since they are chemically homogenous, but illustrate electronically distinct semiconducting (1H phase) and metallic (1T phase) characteristics with matched lattices.

Here, Au substrates were used to introduce phase transition inside single layer MoS_2. The formation of 1T-MoS_2 phase could be initiated by the charge transfer and the built-in strain from Au substrates. Because the unavoidable aging and degradation of MoS_2, significantly affected the desired performance in semiconductors, catalysts and tribological applications, the structural and chemical evolution of MoS_2 under accelerated aging conditions was investigated under UV-ozone condition. We found that, the aging varied strongly with the layer thickness of MoS_2 sample. To systematically tune the electronic properties of MoS_2, diacetylenethiolate-based molecules could be implemented to dope MoS_2 *via* defect engineering since the thiol groups could bond to sulfur vacancies and the diacetylene thiols could form relatively stable polymers on MoS_2 surfaces through UV-induced crosslinking. The mechanical and electronic properties of diacetylene and poly-diacetylene monolayers on Au(111) were fully investigated. The monolayers were found to exhibit higher friction following polymerization due to structural changes in the films. Electronically, size-dependent differences in the electronic properties were found to arise for poly-diacetylene islands of around 10 nm when embedded into a dodecanethiolate matrix, which could be attributed to the Coulomb blockade. The knowledge revealed here will guide future designs and applications of MoS_2-based electronic devices and tribological systems.

DEDICATION

I dedicate this dissertation to all the surface scientists for their knowledge and inspiration in my adventurous surface journey.

ACKNOWLEDGMENTS

I would like to thank my committee chair, Dr. James D. Batteas, for his guidance in research, life, and professional development. I also want to thank my committee member Dr. Karen L. Wooley, Dr. Sarbajit Banerjee and Dr. Xiaofeng Qian for their advice and support.

I want to express my tremendous appreciation to Dong Hee Son, Doyun Kim, Charles Michael Drain, Naga Venkata Satya Dinesh Kumar Bhupathiraju, Michael Chandross, Nicolas Argibay, John F. Curry, Andrew Levine, and Adam Braunschweig, for all the wonderful collaborative opportunities.

I am also very grateful for the supportive, and family-like vibes from my colleagues and labmates: Alison Pawlicki, Meagan Elinski, Zhuotong Liu, Cody Chalker, Nathaniel Hawthorne, Quentarius Moore, Maelani Negrito, Xinyuan Chen, Noah Sheehan, Mckenzie Pedley, Meredith Buzbee, Ben Menard, Thomas Reyes, Abhijeet Gujrati, Maya Costales, Erik Straume, Piyashi Sengupta, and Jennifer Belcik. I also want to thank Andrew Brown, for allowing me to guide him during the Research Experience for Undergraduate (REU) Program. This is definitely the best summer I ever had in my Ph.D. life.

I want to shout out to my friends, Dr. John York, Kris Wang, Dali Huang, Daodao, Yangyang, Han Leng, Jijie Huang, and Leigang Li. Although they are all scattered around world now, I will always remember those old good time we have spent together.

Lastly but most importantly, I would like to express my thanks to Mei and my family for their love.

CONTRIBUTORS AND FUNDING SOURCES

Contributors

This work was directed by a dissertation committee consisting of Professor James D. Batteas (chair), joint appointed in the Department of Materials Science and Engineering and the Department of Chemistry, Professor Sarbajit Banerjee (member), joint appointed in the Department of Materials Science and Engineering and the Department of Chemistry, Professor Karen L. Wooley (member), joint appointed in the Department of Materials Science and Engineering, the Department of Chemical Engineering, and the Department of Chemistry, and Professor Xiaofeng Qian (member) in the Department of Materials Science and Engineering.

The included Raman Spectra in Chapter 3, Chapter 4 and Chapter 5 were provided by Zhuotong Liu and Nathaniel Hawthorne in the Department of Chemistry. The AFM data colleted in Chapter 3 was provided by Zhuotong Liu in the Department of Chemistry. The simulated work for Chapter 3 was conducted by Quentarius Moore in the Department of Chemistry and Dr. Michael Chandross from the Sandia National Laboratories. The Diacetylenethiol molecules were synthesized by Dr. NVS Dinesh K Bhupathiraju from Dr. Charles Michael Drain's group from the City University of New York. All other work conducted for this dissertation was completed by myself independently.

Funding Sources

Graduate study was supported by a National Science Foundation under CHE-1611119 (to J.D.B), CHE-1610755 (to C.M.D.), National Science Foundation under CMMI-1436192, NTESS, LLC-National Technology and Engineering Solutions of Sandia, under contracts 1919201 and 2021982 and the Texas AM University President's Excellence Fund X-Grants Program.

NOMENCLATURE

2D	Two-Dimensional
AFM	Atomic Force Microscopy
AO	Atomic Oxygen
BLM	Bi-layer MoS_2
CVD	Chemical Vapor Deposition
DATs	Diacetylenethiols
DBTJ	Double Barrier Tunneling Junction
DFT	Density Functional Theory
DOS	Density of States
FFT	Fast Fourier Transform
FTIR	Fourier transformed infrared spectroscopy
HOMO	Highest Occupied Molecular Orbital
LDOS	Local Density of States
LEO	Low Earth Orbit
LUMO	Lowest Unoccupied Molecular Orbital
MLM	Milti-Layer MoS_2
MoS_2	Molybdenum Disulfide
Poly-DATs	Poly-Diacetylenethiols
REU	Research Experience for Undergraduate
RSF	Relative Sensitivity Factor
SAMs	Self-Assembled Monolayers
SLM	Single Layer MoS_2

SPIP	Scanning Probe Image Processor
STM	Scanning Tunneling Microscopy
STS	Scanning Tunneling Spectroscopy
TLM	Tri-layer MoS_2
TMDCs	Transition Metal Dichalcogenides
UHV	Ultra High Vacuum
UV	Ultraviolet
WKB	Wentzel-Kramers-Brillouin
XPS	X-Ray Photoelectron Spectroscopy

TABLE OF CONTENTS

Page

LIST OF FIGURES

FIGURE Page

1. INTRODUCTION AND LITERATURE REVIEW

1.1 Structure-Function Properties of 2D Transition Metal Dichalcogenides

Two-dimensional (2D) transition metal dichalcogenides have shown promising potential over the past decade due to the exciting mechanical and electronic properties [1–8]. Different from graphenes single layer structure, 2D-TMDs consist of a transition metal M layer, sandwiched between two layers of chalcogen atoms. Fabricating single and few-layer TMDs not only preserves some of their bulk properties, but additionally leads to exciting novel properties due to the quantum confinement and surface effect.

Molybdenum disulfide (MoS_2), one of the most representative TMDs, can form two common polymorphs, *i.e.*, 2H phase and 1T phase, based on the atomic combination and stacking ordering. These two polymorphs exhibit considerable difference in their electronic properties as a result of the difference in their crystal symmetry. Additionally, when the thickness of, for example, 2H-MoS_2 is reduced from a bulk to a single layer, the nature of the electronic structure switches from an indirect bandgap to a direct bandgap, opening up new opportunities in optoelectronics, spintronics and valleytronics [9–13]. The 1T phase (distorted variation is called 1T') is thermodynamically unstable, which has received great attentions recently, for its topological properties, such as the quantum spin Hall effect, dipolar ferroelectricity and Wely semi-metallicity in several 2D-TMDs, *i.e.*, MoS_2, $MoTe_2$ and WTe_2 [14, 14–17].

1.2 Strategic Fabrication of 2D-MoS_2

To date, 2D-MoS_2 can be fabricated strategically mainly *via* three approaches, *i.e.*, mechanical exfoliation, liquid exfoliation, and vapor deposition method.

Mechanical exfoliation implementing scotch tapes can be used to obtain high quality single- and few-layer MoS_2 [1, 18]. In this method, MoS_2 flakes are peeled off from their bulk crystal and then transferred on a silica surface. The advantage of this method is that, it's very simple and inexpensive. The disadvantage is that, due to the weak van der Waals forces between the oxidized

silicon surface and the MoS_2 flakes, the monolayer yield is extremely low. Recently, a new method has been developed to achieve a high yield with centimeter-sized MoS_2 monolayer exfoliation [19, 20]. The key step in this method was, instead of using a SiO_2 substrate, the exfoliation yield could be significantly improved by enhancing the adhesion between the basal plane of the MoS_2 flakes and the substrate. In this case, a freshly prepared gold substrate was employed. Because of the lack of any chemicals involved in the mechanical exfoliation process, the structural integrity and crystallinity of MoS_2 are conserved, which serves a decent platform for fundamental studies of the structure-function relationships of 2D-MoS_2.

Usually, liquid exfoliation can be categorized into two classes, *i.e.*, liquid phase ultrasonic exfoliation and chemical exfoliation. In liquid phase ultrasonic exfoliation, bulk dispersion of single- and few-layer MoS_2 flakes can be easily exfoliated in organic solvents (*e.g.*, N-methyl-pyrrolidone) with moderate polarity [21]. To improve the yield of the exfoliation, surfactant-assisted ultrasonic exfoliation can be carried out by utilizing chemicals such as sodium cholate and bovine serum albumin [22]. The liquid phase ultrasonic exfoliation not only enables large scale production but also allows a great number of liquid-based techniques for photovoltaics and tribology applications [23–25]. The disadvantage of this technique is that the exfoliated MoS_2 flakes are mainly in the form of multi-layers and thus, require further treatment. To improve the yield, chemical exfoliation can be implemented to produce single-layer MoS_2 *via* lithium ion intercalation [26]. In this method, lithium ions intercalate and weaken the interlayer interaction in the bulk MoS_2. Then, with the support of ultrasonication, Li_xMoS_2 monolayers are formed and stably disperse within the solvent (*e.g.*, hexane). The advantage of chemical exfoliation is that the yield can be as high as 100% while the disadvantage is that, the lateral size produced by this method is limited to 200 to 800 nm as well as a partial transformation in phases from 2H to 1T [7].

2D-MoS_2 can also be synthesized by vapor deposition. In fact, chemical vapor deposition (CVD) has proved to be a reliable and widely used technique for growing 2D materials with a controllable manner. Based on the variations of growth conditions, the CVD-grown of MoS_2 can be classified into three categories: decomposition of Mo and S containing vapor precursors separately

and formation of MoS_2 on specific substrates [27–29], direct sulfurization of Mo containing thin films [30], and hydrothermal-solvothermal reaction [31–35].

2D-MoS_2 sheets can be directly synthesize on silica substrates *via* MoO_3 and S precursors. The growth of 2D-MoS_2 is very sensitive to the pre-treatment of the substrate. The employment of graphene-like molecules, such as perylene-3,4,9,10-tetracarboxylic, enhance growth of MoS_2 [27]. Sørensen and coworkers have also reported synthesizing single-layer MoS_2 on metal substrates. In their approach, Mo and H_2S were deposited simultaneously on a Au(111) surface. High quality MoS_2 monolayers were produced in the form of a characteristic moiré pattern due to the lattice mismatch between the MoS_2 and the substrate Au [28]. In the direct sulfurization case, 2D-MoS_2 flakes can be obtained by direct sulfurization of Mo-based thin films, *e.g.*, MoO_3 [30]. The lateral dimension and the layer thickness of the resulting MoS_2 films are determined by the Mo-based films, which makes it a highly controllable and scalable technique. Besides the in-plane growth, the MoS_2 flakes can also grow vertically via a rapid sulfurization at elevated temperature (550 °C) [36]. The advantage of the kinetic-driven vertical growth process is that, it maximizes the low-coordinate surface sites (*e.g.*, edges and kinks), and promotes various catalytic reactions [37]. In the last case the hydrothermal-solvothermal approach, Mo containing precursors and S containing precursors are dissolved in water or other solvents. After applying a high temperature and high pressure, 2D-MoS_2 can be formed with different structures (nanoflower or nanotube). Particularly, the MoS_2 flakes prepared by this method contain a large density of surface defects as well as a partial 2H-to-1T phase transformation. Besides the simplicity and wide range of applications, the hydrothermal-solvothermal method demonstrates attractive potential as a facile way for MoS_2 hybridization with other advanced functional materials (*e.g.*, nano-Fe_3O_4) [38].

Given the multiple synthesis options, a facile way to fabricate high quality 2D-MoS_2 is therefore the key in this dissertation. Considering the difficulty of handling alkali metals in liquid exfoliation and the extensive time and cost in CVD method, mechanical exfoliation yields the highest quality of MoS_2 nanosheets. Because of the strong affinity between Au and S atoms of the basal plane of MoS_2, it is possible to further enhance the exfoliation yield by utilizing a gold

substrate instead of a silica wafer. Therefore, in this work three questions have been researched to gain a more comprehensive understanding of the structural evolution of MoS_2 on metal surfaces. I) How does the structure of 2D-MoS_2 evolve after deposited on a gold substrate. II) How does the structure of 2D-MoS_2/Au(111) evolve under accelerated aging conditions. III) How to systematically tune the electronic properties of 2D-MoS_2/Au(111) *via* defect engineering. By addressing these questions, the work here provides a fundamental understanding of the structural evolution of MoS_2 on metal surfaces, under accelerated aging conditions as well as a systematic way to tune the electronic properties of MoS_2 *via* defect engineering of chemisorption.

1.3 Deposition of MoS_2 on Au(111)

The deposition of MoS_2 on metal surfaces is critical for fabricating and designing MoS_2-based electronic and catalysis systems. The research of MoS_2 on gold substrates was first initiated by F. Besenbacher and coworkers earlier this century [39–41]. In their studies, they demonstrated the formation of the one-dimensional metallic edge states in single-layer MoS_2 nanoclusters, which could potential serve as active sites for catalysis process (*e.g.*, hydrodesulfurization catalysis).

Recently, growth of high quality large MoS_2 monolayers on Au(111) has been reported using CVD method under UHV environment [28]. A complete characterization including scanning tunneling microscopy (STM) and x-ray photoelectron spectroscopy (XPS) has been carried out showing the topographical and electronic properties of the MoS_2 monolayers on Au surfaces. Due to the periodic modulation of the films induced by the lattice mismatch, a characteristic moiré pattern is observed. While the Au(111) surfaces give rise to the out-of-plane strain for single-layer MoS_2, no strain or periodic modulation is observed for MoS_2 on polycrystalline Au or silica surfaces [42]. In addition, XPS results show that the MoS_2 is n-dope due to the electron donation from the Au substrates. Scanning tunneling spectroscopy (STS) further indicates a strong hybridization between the Au states and the valence band of MoS_2.

Besides the CVD synthesis of MoS_2/Au(111) in UHV, mechanical exfoliation of large-area (hundreds of micron) MoS_2 monolayers was reported due to the strong chemical affinity of the S atoms to the Au as compared to the neighboring layers in the bulk MoS_2 [43]. Later, centimeter-

sized MoS_2 was reported and the MoS_2-Au interaction was confirmed to be a strong van der Waals force rather than covalent bond [19]. Native defect density of the exfoliated MoS_2 has been investigated [44]. The defect concentration has been imaged and analyzed in the order of 10^{-13} cm^{-2}. However, a combined studies using low-temperature non-contact atomic force microscopy (AFM) and STM, and ab initio density functional theory (DFT) and GW calculations showed controversial results [45]. They suggested that the common defects usually found in 2D-MoS_2 sheets, are oxygen substitutional defects, instead of point defects or sulfur vacancies. Complementary qPlus studies by Nils indicated that, in additional to the oxygen substitutional defects, nanometer-sized patches commonly observed in STM are due to the Au vacancy islands underneath the MoS_2 layers [46].

1.4 Evolution of MoS_2/Au(111) under Accelerated Aging Conditions

Because of the promising potential in a wide range of applications, one of the major goals in this work is to understand the degradation and stability of 2D-MoS_2 under accelerated aging conditions. Since there is a great overlap between the controlled etching and the aging on MoS_2, in this section, we will mainly focus on the literature on oxygen related aging studies, particularly, the oxidation of MoS_2 under pure O_2, O_2 plasma and UV-ozone conditions. We will not cover the discussion on sputtering, electron irritation, charged particle irritation, Gamma-ray irradiation and x-ray irradiation.

2-D MoS_2 nanosheets are generally considered to be stable in air. However, Jian and his team [47] showed that, contract to this current understanding, MoS_2 monolayers grown by CVD method demonstrated relatively poor air stability. The MoS_2 monolayers exhibited extensive cracking and significant changes in morphology and photoluminescence spectroscopy when exposed in air at room temperature for several months. They attributed such an aging effect to the oxidation of MoS_2 along the grain boundaries and the adsorption of organics from the environment. Similar to this result, a systematic investigation of oxidation for two MoS_2 films (amorphous and highly ordered) before and after exposure to atomic oxygen and high temperature annealing in molecular oxygen reveals that, the ordered MoS_2 films showed a considerably higher resistance to both atomic and molecular oxygen at elevated temperature, comparing to the amorphous MoS_2 films [48]. To

understand the degradation and aging of ordered MoS_2 films at elevated temperature, Yamamoto *et al.* exposed mechanically exfoliated MoS_2 on silica substrates to oxygen in air at 300-340 °C. They observed an anisotropic etching behavior of MoS_2 which was initiated at native defect sites. Raman spectroscopy confirmed that no oxidative form (MoO_3) was produced in this temperature range [49]. Similar anisotropic etching results have also been reported by Jumiati textitet al. around the same time [50]. However, their XPS spectra indicated that parts of the MoS_2 films were oxidized to form MoO_3. Besides the temperature effect on the accelerated aging of 2D-MoS_2 flakes, the partial pressure of O_2 can also affect the oxidation process of MoS_2. By utilizing ambient pressure XPS and TEM, Dooyong textitet al. measured the work-function variation during the transformation of MoS_2 to MoO_3 [51]. They showed that by annealing MoS_2 in 1 mbar O_2 + 1 mbar Ar at 350 °C, MoS_2 could be fully converted to MoO_3 without any anisotropic etching occurred.

2D-MoS_2 flakes can also be oxidized *via* oxygen plasma treatment. After oxidation, the photoluminescence was quenched [52]. However, detailed studies by Zhenhuas group showed that, instead of being quenched, the photoluminescence was actually enhanced by thousands of times at crack and defect sites. They concluded that this was due to the p-doping at crack and defect sites as the oxygen adsorbed and the suppression of nonradiative recombination of excitons at defect sites [53]. Later, Suhhyun *et al.* reported the O_2 plasma could also be used to etch and control the layer thickness of 2D-MoS_2, which was similar to thermal annealing in air at elevated temperature [54]. In contrast to this findings, Wen *et al.* demonstrated that by carefully controlling (lowering) the energy applied in O_2 plasma treatment, oxygen species could just be physically adsorbed without oxidizing or etching away 2D-MoS_2 flakes [55].

2D-MoS_2 nanosheets can also be accelerated aged under UV-ozone conditions. Similarly, by lowering the UV power, the oxidation of MoS_2 could be eliminated, while the surface energy was increased due to physical adsorption of oxygen species. To better understand the UV-ozone process and better serve further functionalization of MoS_2 with dielectrics (*e.g.*, Al_2O_3), Wallace *et al.* investigated the UV-ozone oxidation of MoS_2 in situ with additional controls of the oxidation factors involved in the UV-ozone oxidation [56]. They found that there was no reaction or oxidation

occurred to MoS_2 by leaking O_3 solely into the reaction chamber. UV was essential, not only because it could increase the reactivity of O_3, but also to generate atomic oxygen that could react and oxidize MoS_2.

1.5 Systematically Tuning the Electronic Properties of MoS_2 by Defect Engineering of Molecular Doping

Based on the surface defects discussion above, these undercoordinated surface sites can be identified as potential synthetic starting points for surface modification. Particularly, surface defects containing sulfur vacancies can provide enormous possibilities when functionalized with thiol molecules to tune the properties of MoS_2 comparing to the inertness of complete MoS_2 sheets [57, 58]. In addition, the surface vacancies in MoS_2 can be created by thermal annealing at 250 °C and serve as the starting reaction sites for thiol-terminated organic molecules. However, the major challenge now is that the surface functionalization is not stable, the dissociation of the S-C bond can be induced by subtle environmental perturbation, which has been reported as the self-repairing mechanism of vacancy defects [59]. Here, thiol-terminated diacetylenes, especially the polymerized diacetylene thiols was examined on Au(111) surfaces. The highly conjugated structures, combined with covalent bonds to the MoS_2 substrates, will result in a more rigid feature compared to typical alkanethiols or other thiol-containing molecules. Such a rigidity has been reported previous that the poly-diacetylene thiols exhibit excellent stability to repeated electrochemical cycling at extreme conditions, high temperature annealing up to 200 °C, and long-time exposure to hot base solutions [60].

1.6 Summary

In conclusion, a fundamental understanding of structural evolution of 2D-MoS_2 on metal surfaces is critical for fabricating and designing MoS_2-based electronic, catalysis and tribological systems. Following in Chapter 2, the advanced surface characterization techniques studying the 2D-MoS_2/Au(111) system are discussed. In Chapter 3-5, three main questions are addressed accordingly, with the purpose to understand and design novel MoS_2/Au(111) system: I) How does

the structure of 2D-MoS_2 evolve after deposited on Au(111) substrates. II) How does the structure of 2D-MoS_2/Au(111) evolve under accelerated aging conditions. III) How to systematically tune the electronic properties of 2D-MoS_2/Au(111) *via* defect engineering of chemisorption. Lastly, Chapter 6 summarizes and concludes this dissertation.

2. ADVANCED SURFACE ANALYSIS TECHNIQUES

In this chapter, we discuss the theoretical consideration of the major instrumental techniques employed in our experiments.

2.1 Scanning Tunneling Microscopy (STM)

Back to 1959, R. P. Feynman first postulated the potential of nanotechnology in his visionary presentation entitled There is Plenty of Room at the Bottom. More than 60 years later with the advancements in microscopy technology, imaging structures at nanoscale become possible. Among those, scanning probe microscope represents a unique tool, which can not only image, but also manipulate structure on surface [61].

The first model of scanning probe microscopy, the scanning tunneling microscopy (STM) was first invented by Binnig and Rohrer in 1981. They received the Nobel Prize in physics for their invention five years later in 1986. In STM, a bias is implemented between a metal tip and a conducting sample. The tip is approached toward the sample until a tunneling current is detected. The tip is controlled and positioned with a very high accuracy using piezoelectric actuator materials. The mechanical expansion or contraction of piezoelectric actuator is proportional to the voltage applied to their electrodes. While the tip is scanned across the sample surface in x and y directions, a feedback loop constantly adapts the tip in z direction by approaching or retracting the tip to maintain a constant tunneling current between the tip and the sample. Recording the tip height (z signal) as a function of the x and y coordinates, generates a STM image corresponding to the topography of the sample surface.

2.1.1 Theoretical Models for Tunneling in STM

The tunneling junction (tip-gap-sample) can be handled in different ways. The simplest case is the one-dimensional potential barrier model (Figure 2.1). For one-dimensional model, a square potential barrier $V(z)$ (height $= V_0$) is considered within the region between $z = 0$ and $z = d$. E is the energy of a tunneling electron. The time-dependent Schrödinger equation can be written as:

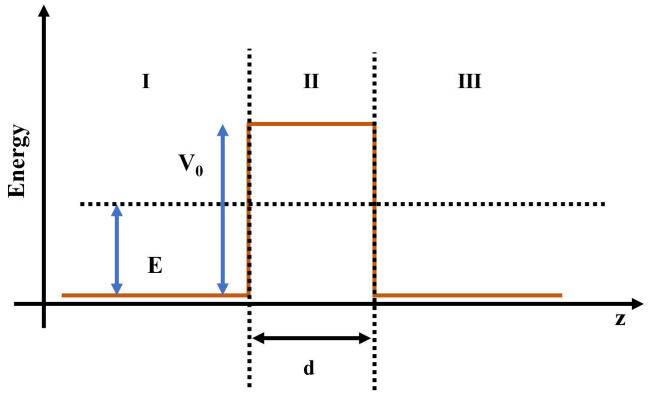

Figure 2.1: Graphical illustration for one-dimensional tunneling junction.

$$\hbar\frac{\partial}{\partial t}\Psi(\mathbf{r},t) = \left(-\frac{\hbar^2}{2m}\Delta + V(\mathbf{r},t)\right)\Psi(\mathbf{r},t). \tag{2.1}$$

The time-dependent part of the solution can be written as $\phi(t) = exp(-\frac{i}{\hbar}Et)$, and the solution of this time-dependent Schrödinger equation can be written as: $\Psi(\mathbf{r},t) = exp(-\frac{i}{\hbar}Et)\psi(\mathbf{r})$. Then we can get

$$\frac{\hbar^2}{2m}\frac{\partial^2}{\partial z^2}\psi(z) = [V(z) - E]\psi(z). \tag{2.2}$$

The solutions for this in all three regions is

$$\psi(z) = \begin{cases} Ae^{ik_1 z} + Be^{-ik_1 z} & z < 0 \text{ (Zone I)} \\ Ce^{-k_2 z} + De^{k_2 z} & 0 \leq z \leq d \text{ (Zone II)} \\ Fe^{ik_1 z} & z > d \text{ (Zone III)} \end{cases} \tag{2.3}$$

Where

$$k_1 = \sqrt{\frac{2m}{\hbar^2}E} \tag{2.4}$$

$$k_2 = \sqrt{\frac{2m}{\hbar^2}(V_0 - E)}. \tag{2.5}$$

The coefficients A, B, C, D, F can be calculated from continuity and boundary conditions. Using a computer algebra system, we can calculate the these coefficients. Particularly, the absolute square of the coefficient F is

$$T = |F|^2 = \frac{4k_1^2 k_2^2}{(k_1^2 + k_2^2)^2 \sinh^2(k_2 d) + 4k_1^2 k_2^2}. \tag{2.6}$$

Note that F represents the possibility of find an electron past the barrier, and thus we can also call it the transmission Factor. By using the mathematical approximation when $k_2 d \gg 1$,

$$\sinh^2 k_2 d \approx \frac{1}{4} e^{2k_2 d} \tag{2.7}$$

and another approximation (neglecting the last term in the denominator), the transmission factor T becomes

$$T = \frac{16k_1^2 k_2^2}{(k_1^2 + k_2^2)^2} e^{-2k_2 d} = \frac{16E(V_0 - E)}{V_0^2} exp\left[-2d\sqrt{\frac{2m}{\hbar^2}(V_0 - E)}\right]. \tag{2.8}$$

The discussion here shows the transmission factor when $E \leq V_0$. In the other scenario when $E > V_0$, then the constant term k_2 becomes imaginary. By defining $k_2 = ik_3$, the transmission factor is now

$$T = |F|^2 = \frac{4k_1^2 k_3^2}{(k_1^2 - k_3^2)^2 \sin^2(k_3 d) + 4k_1^2 k_3^2}. \tag{2.9}$$

In this case ($E > V_0$), the transmission factor has an oscillatory character approaching unity at particular energy ($k_3 d = n\pi, k_3 = 2\pi/\lambda, n\lambda/2 = d$).

Although the one-dimensional potential model proves to be quite straightforward and helpful, several problems remain in this method. First, the wave function is not normalized. Second, no voltage potential difference between the electrodes (tip and sample) is discussed. Third, instead of density of states, only one electron state is considered here which deviates significantly from the real tunneling situations [62]. Because of these limitation, the Wentzel-Kramers-Brillouin

approximation is used to solve a general one-dimensional potential barrier.

For a free electron, the general wave function of the time-independent Schrödinger equation is

$$\psi(x) = Ce^{\pm ikz}, \tag{2.10}$$

where C is a normalized constant and $k = \frac{1}{\hbar}\sqrt{2m(E-V)}$. Note that k varies as the potential V changes (as discussed in the previous section). To solve the transmission factor for a one-dimensional potential varying spatially, first we can write the wave function at position z_1 as

$$\psi(z_1) = \psi(z_0)\, exp\left[\pm i \int_{z_0}^{z_1} k(z)dz\right]. \tag{2.11}$$

When $E - V(z) < 0$, and eliminating the pre-exponential factor in Equation 2.8, the transmission factor is

$$T = \left|\frac{\psi(z_1)}{\psi(z_0)}\right|^2 = exp\left[-\frac{2\sqrt{2m}}{\hbar}\int_{z_0}^{z_1}\sqrt{(V(z)-E)}dz\right]. \tag{2.12}$$

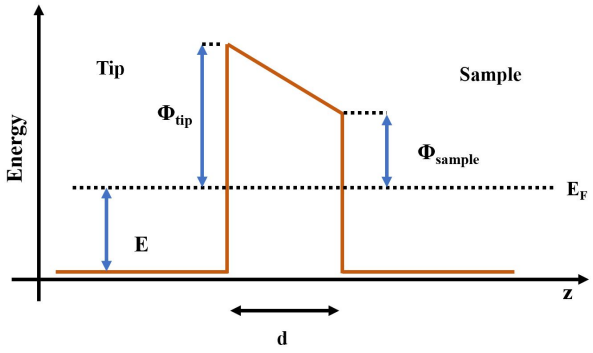

Figure 2.2: Trapezoidal potential barrier for WKB model approximation in a STM tunneling junction.

Therefore, we have shown that the transmission factor can be calculated for a general form of a potential barrier. One typical case of applying the WKB approximation is considering a trapezoidal

potential barrier (Figure 2.2). The potential can be written as $V(z) = E+\psi_{tip}-z/d(\psi_{tip}-\psi_{sample})$ and the T can is now written as

$$T = exp\left[-\frac{4d\sqrt{2m}}{3\hbar(\psi_{tip}-\psi_{sample})}(\psi_{tip}^{3/2}-\psi_{sample}^{3/2})\right]. \tag{2.13}$$

Next, we will discuss the Bardeen approach for tunneling in solid. Before our discussion, a few concepts need to be clarified. First, we need to know the concept of density of states (DOS). The definition for DOS $\rho(E)$ is

$$\rho(E) = \frac{dN(E, E+dE)}{dE}, \tag{2.14}$$

or

$$\rho(E) = \sum_n \delta(E-E_n). \tag{2.15}$$

The next concept is the local density of states (LDOS). The definition of LDOS is the DOS with additional consideration of spatial distribution

$$\text{LDOS} = \rho(E, r) = \sum_n |\psi_n(r)|^2 \delta(E-E_n). \tag{2.16}$$

Now, we can start discussing Bardeen's model. To apply his model in STM, the tip-barrier and the sample-barrier are considered as two separate systems [63]. The wave functions in these two subsystems can be obtained, again by solving the time-independent Schrödinger equation. A simplified energy diagram showing the tunneling process is illustrated in Figure Figure 2.3. A few conditions need to be fulfilled in this model. First, the potential in this system is $V_{total}(\mathbf{r}) = V_{tip}(\mathbf{r}) + V_{sample}(\mathbf{r})$. Next the tip potential is zero inside the sample region and *vice versa*. Third, the vacuum level is set as zero energy. The time-dependent Schrödinger equation for the tip and

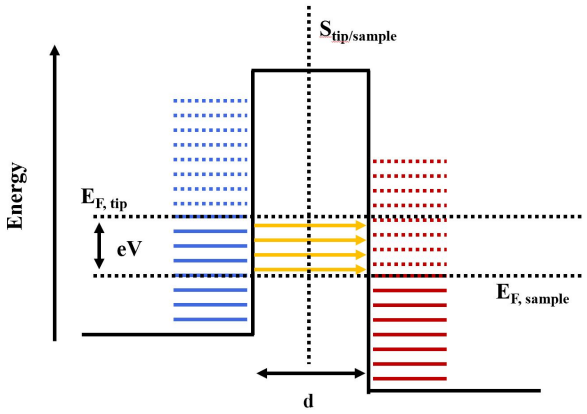

Figure 2.3: Energy diagram of a typical tunneling process when a positive bias is applied to the sample or a negative bias is applied to the tip (zero temperature limit).

the sample can be written as

$$i\hbar\frac{\partial\Psi_{tip,i}(\mathbf{r},t)}{\partial t} = \left[-\frac{\hbar^2}{2m}\Delta + V_{tip}(\mathbf{r})\right]\Psi_{tip,i}(\mathbf{r},t), \tag{2.17}$$

and

$$i\hbar\frac{\partial\Psi_{sample,j}(\mathbf{r},t)}{\partial t} = \left[-\frac{\hbar^2}{2m}\Delta + V_{sample}(\mathbf{r})\right]\Psi_{sample,j}(\mathbf{r},t). \tag{2.18}$$

The solution for the tip equation at state i is

$$\Psi_{tip,i}(\mathbf{r},t) = \psi_{tip,i}(\mathbf{r})\, exp\left(-\frac{iE_i t}{\hbar}\right). \tag{2.19}$$

The solution for the sample equation at state j is

$$\Psi_{sample,j}(\mathbf{r},t) = \psi_{sample,j}(\mathbf{r})\, exp\left(-\frac{iE_j t}{\hbar}\right). \tag{2.20}$$

The time-independent Schrödinger equation for the tip at state i can be written as

$$\left(-\frac{\hbar^2}{2m}\Delta + V_{tip}(\mathbf{r})\right)\psi_{tip,i}(\mathbf{r}) = E_i\psi_{tip,i}(\mathbf{r}). \tag{2.21}$$

The time-independent Schrödinger equation for the sample at state j can be written as

$$\left(-\frac{\hbar^2}{2m}\Delta + V_{sample}(\mathbf{r})\right)\psi_{sample,j}(\mathbf{r}) = E_j\psi_{sample,j}(\mathbf{r}). \tag{2.22}$$

Now we consider an electron tunnels from its initial state i of the tip to the final state j of the sample. The time-dependent wave function of the whole system is

$$\Psi_{final}(\mathbf{r},t) = \Psi_{tip,i}(\mathbf{r},t) + \sum_j a_j(t)\Psi_{sample,j}(\mathbf{r},t). \tag{2.23}$$

Now we can write the time-dependent Schrödinger equation of the wave function $\Psi_{final}(\mathbf{r},t)$ as

$$i\hbar\frac{\partial\Psi_{final}(\mathbf{r},t)}{\partial t} = \left[\frac{-\hbar^2}{2m}\Delta + V_{tip}(\mathbf{r}) + V_{sample}(\mathbf{r})\right]\Psi_{final}(\mathbf{r},t). \tag{2.24}$$

Applying the wave function (Equation 2.23) into the equation of the whole system above, we can get

$$\begin{aligned} &i\hbar\tfrac{\partial\Psi_{tip,i}(\mathbf{r},t)}{\partial t} + i\hbar\sum_j \tfrac{da_j(t)}{dt}\Psi_{sample,j}(\mathbf{r},t) + i\hbar\sum_j a_j(t)\tfrac{\partial\Psi_{sample,j}(\mathbf{r},t)}{\partial t} \\ &= \left[-\tfrac{\hbar^2}{2m}\Delta + V_{tip}(\mathbf{r})\right]\Psi_{tip,i}(\mathbf{r},t) + V_{sample}(\mathbf{r})\Psi_{tip,i}(\mathbf{r},t) \\ &+ \left[-\tfrac{\hbar^2}{2m}\Delta + V_{tip}(\mathbf{r}) + V_{sample}(\mathbf{r})\right]\sum_j a_j(t)\Psi_{sample,j}(\mathbf{r},t). \end{aligned} \tag{2.25}$$

We can cancel out some terms in this equation and thus we can rewrite it as

$$i\hbar\sum_j \frac{da_j(t)}{dt}\Psi_{sample,j}(\mathbf{r},t) = V_{sample}(\mathbf{r})\Psi_{tip,i}(\mathbf{r},t) + V_{tip}(\mathbf{r})\sum_j a_j(t)\Psi_{sample,j}(\mathbf{r},t). \tag{2.26}$$

By replacing the $\Psi_{tip,i}(\mathbf{r},t)$ and $\Psi_{sample,j}(\mathbf{r},t)$, we can get

$$i\hbar \sum_j \frac{da_j(t)}{dt}\psi_{sample,j}(\mathbf{r})\, exp\left(-\frac{iE_j t}{\hbar}\right) = V_{sample}(\mathbf{r})\psi_{tip,i}(\mathbf{r})\, exp\left(-\frac{iE_i t}{\hbar}\right) \\ +V_{tip}(\mathbf{r}) \sum_j a_j(t)\psi_{sample,j}(\mathbf{r})\, exp\left(-\frac{iE_j t}{\hbar}\right). \tag{2.27}$$

Next, by multiplying this equation by the wave function $\Psi^*_{sample,f}$ at a specific sample state f, and perform a spatial integration, we can get

$$i\hbar \frac{da_f(t)}{dt}\, exp\left(-\frac{iE_f t}{\hbar}\right) = \int \psi^*_{sample,f}(\mathbf{r})V_{sample}(\mathbf{r})\psi_{tip,i}(\mathbf{r})d^3\mathbf{r}\, exp\left(-\frac{iE_i t}{\hbar}\right) \\ +V_{tip}(\mathbf{r})a_f(t)\, exp\left(-\frac{iE_f t}{\hbar}\right). \tag{2.28}$$

Since the a_f terms are small, we can neglect the last term in the equation above and thus the differential equation of a_f can be written as

$$\frac{da_f(t)}{dt} = \frac{1}{i\hbar}\int \psi^*_{sample,f}(\mathbf{r})V_{sample}(\mathbf{r})\psi_{tip,i}(\mathbf{r})d^3\mathbf{r}\, exp\left[\frac{i(E_f - E_i)t}{\hbar}\right]. \tag{2.29}$$

The expression

$$M_{fi} = \int\limits_{\Gamma_{sample}} \psi^*_{sample,f}(\mathbf{r})V_{sample}(\mathbf{r})\psi_{tip,i}(\mathbf{r})d^3\mathbf{r} \tag{2.30}$$

is called the matrix element. By integrating the differentiation equation above, we can get

$$a_f(t) = \frac{1}{i\hbar}M_{fi}\int\limits_0^t exp\left[\frac{i(E_f - E_i)t'}{\hbar}\right]dt' = -M_{fi}\frac{exp\left[i(E_f - E_i)t/\hbar\right] - 1}{E_f - E_i} \\ = -2iM_{fi}exp\left[i(E_f - E_i)t/2\hbar\right]\frac{\sin[(E_f - E_i)t/2\hbar]}{E_f - E_i}. \tag{2.31}$$

Using this equation, the probability of finding an electron in the sample state f which originates

from the tip state i is

$$|a_f(t)|^2 = -4|M_{fi}|^2 \frac{\sin^2[(E_f - E_i)t/2\hbar]}{(E_f - E_i)^2} = |M_{fi}|^2 \frac{2t}{\hbar} \frac{\sin^2[(E_f - E_i)t/2\hbar]}{(E_f - E_i)^2 t/2\hbar}. \tag{2.32}$$

From this equation, we can see the probability of finding an electron in a final state f is high when E_f is close to E_i. The probability of finding an electron $|a_f(t)|^2$ becomes infinitely narrow and tall with increasing t. By applying Dirac delta function, we can get the

$$|a_f^\infty(t)|^2 = \frac{2\pi}{\hbar}|M_{fi}|^2 \delta(E_f - E_i)t, \tag{2.33}$$

in the limit of large-scale times. Therefore, the tunneling from an initial tip state to a final sample state results a transition rate of

$$w_{tip,i\to sample,f} = |a_f^\infty(t)|^2/t = \frac{2\pi}{\hbar} |M_{fi}|^2 \, \delta(E_{sample,f} - E_{tip,i}), \tag{2.34}$$

where the matrix element $M_{f,i}$ is (inserting the expression from Equation 2.22)

$$\begin{aligned} M_{f,i} = \; M_{fi} \;&=\; \int\limits_{\Gamma_{sample}} \psi^*_{sample,f}(\mathbf{r}) V_{sample}(\mathbf{r}) \psi_{tip,i}(\mathbf{r}) d^3\mathbf{r} \\ &=\; \frac{\hbar^2}{2m} \int\limits_{S_{tip/sample}} \left[\psi_{tip,i}(\mathbf{r}) \nabla \psi^*_{sample,f}(\mathbf{r}) - \psi^*_{sample,f}(\mathbf{r}) \nabla \psi_{tip,i}(\mathbf{r})\right] d\mathbf{S}. \end{aligned} \tag{2.35}$$

To calculate the total transition rate, the sum needs to be applied as

$$w_{tip,i\to sample,f} = \frac{2\pi}{\hbar} \sum_{i,f} |M_{fi}|^2 \, \delta(E_{sample,f} - E_{tip,i}). \tag{2.36}$$

Then the tunneling current is (consider the spin and the electron charge)

$$I = \frac{4\pi e}{\hbar} \sum_{i,f} |M_{fi}|^2 \, \delta(E_{sample,f} - E_{tip,i}). \tag{2.37}$$

Since the sum over the tip and the sample states in Equation 2.37 is an abstract entity, we can replace it by the energy-dependent DOS of the tip and the sample in the form of the energy-dependent approximation of the Bardeen model. Here, the wave-function dependent matrix element can be replaced by the energy-dependent matrix element as

$$M_{f,i}\left(\psi^{*}_{sample,f}(\mathbf{r}),\, \psi_{tip,i}(\mathbf{r})\right) = M(E_f, E_i) = M(E_f). \tag{2.38}$$

Note that the last term in Equation 2.38 results from the co-appearance of the matrix element with the delta function. Before we replace the wave-function dependent matrix element to the energy-dependent matrix element, the following form of Dirac delta function needs to be introduced as

$$\int_{-\infty}^{\infty} f(\varepsilon)\delta(\varepsilon - E_f)d\varepsilon = f(E_f), \tag{2.39}$$

by inserting $f(\varepsilon) = |M(\varepsilon)|^2\delta(\varepsilon - E_i)$, we can get

$$|M(E_f)|^2\delta(E_f - E_i) = \int_{-\infty}^{\infty} |M(\varepsilon)|^2\delta(\varepsilon - E_i)\delta(\varepsilon - E_f)d\varepsilon. \tag{2.40}$$

Replacing this of the portion in equation (2.36) and only integrate over the bias window gives us

$$\begin{aligned} w_{tip\to sample} &= \frac{2\pi}{\hbar}\sum_{i,f}\int_{E_F,sample}^{E_F,tip} |M(\varepsilon)|^2\delta(\varepsilon - E_i)\delta(\varepsilon - E_f)d\varepsilon \\ &= \frac{2\pi}{\hbar}\int_{E_F,sample}^{E_F,tip} |M(\varepsilon)|^2 \sum_i \delta(\varepsilon - E_i)\sum_f \delta(\varepsilon - E_f)d\varepsilon. \end{aligned} \tag{2.41}$$

The sum over the initial state i and the final state f can be replaced by Equation 2.15 and thus leads to the following equation as

$$w_{tip\to sample} = \frac{2\pi}{\hbar} \int_{E_F,sample}^{E_F,tip} |M(\varepsilon)|^2 \rho_{tip}(\varepsilon)\rho_{sample}(\varepsilon)d\varepsilon. \tag{2.42}$$

The corresponding current is now written as

$$I = 2e\, w_{tip\to sample} = \frac{4\pi e}{\hbar} \int_{E_F,sample}^{E_F,tip} |M(\varepsilon)|^2 \rho_{tip}(\varepsilon)\rho_{sample}(\varepsilon)d\varepsilon. \tag{2.43}$$

From the equation Equation 2.43 we can see the tunneling current is a convolution of the tip states and the sample states which also means to obtain the information about the sample states, the electronic structure of the tip need to be known. Now let's choose the sample Fermi level as zero energy and the tip Fermi level as the reference energy for the tip states, the equation Equation 2.43 can be rewritten as

$$I = \frac{4\pi e}{\hbar} \int_0^{eV} \rho_{tip}(\varepsilon - eV)\rho_{sample}(\varepsilon)|M(\varepsilon)|^2 d\varepsilon, \tag{2.44}$$

and the $M(\varepsilon)$ is

$$M(\varepsilon) = \frac{\hbar^2}{2m} \int_{S_{tip/sample}} \left[\psi_{tip}(\mathbf{r},\varepsilon)\nabla\psi^*_{sample}(\mathbf{r},\varepsilon) - \psi^*_{sample}(\mathbf{r},\varepsilon)\nabla\psi_{tip}(\mathbf{r},\varepsilon)\right] d\mathbf{S}. \tag{2.45}$$

We can further approximate Bardeen matrix element in the one-dimensional rectangular barrier case. If we only consider elastic tunneling ($E_i = E_f = E$, $thus\, E_{f,i} = M(E)$), and a simplified model as one-dimensional rectangular barrier, then the matrix elements can be written as

$$M(E) = \frac{\hbar^2}{2m} \int_{z=z_s} \left[\psi_{tip}(z,E)\frac{\partial\psi^*_{sample}(z,E)}{\partial z} - \psi^*_{sample}(z,E)\frac{\partial\psi_{tip}(z,E)}{\partial z}\right] d\mathbf{S}. \tag{2.46}$$

The schematic illustration of tip and sample wave functions are shown in Figure 2.4. For the

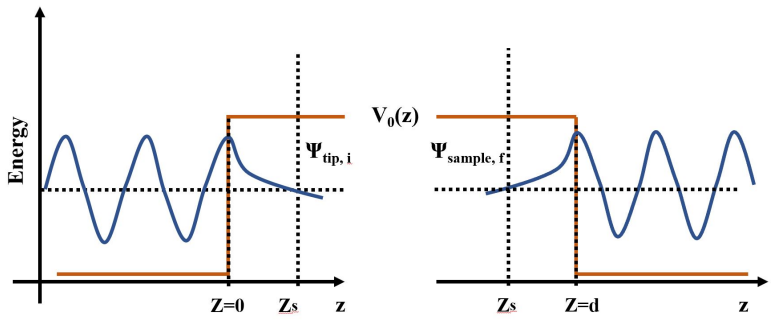

Figure 2.4: The Schematic of Bardeen Matrix Elements for a One-Dimensional Barrier.

individual tip and sample system, the wave functions for each can be written as

$$\psi_{tip}(z) = \psi_{tip}(0)e^{-k_2 z}, \tag{2.47}$$

and

$$\psi_{sample}(z) = \psi_{sample}(d)e^{k_2(z-d)}, \tag{2.48}$$

where the decay constant is $k_2 = \sqrt{2m(V_0 - E)}/\hbar$. By inserting equation Equation 2.47 and Equation 2.48 into equation Equation 2.46, we can get

$$\begin{aligned} M(E) &= \frac{\hbar^2}{2m} \int_{z=z_s} 2k_2 \psi_{tip,i}(0)\psi_{sample,f}(d)e^{-k_2 z_s} e^{k_2(z_s-d)} dS \\ &= \frac{\hbar^2}{2m} k_2 \psi_{tip,i}(0)\psi_{sample,f}(d)Ae^{-k_2 d} \\ &= \frac{\hbar^2}{2m}\sqrt{2m(V_0 - E)}/\hbar\,\psi_{tip,i}(0)\psi_{sample,f}(d)Ae^{d\sqrt{2m(V_0-E)}/\hbar} \\ &= \frac{\hbar^2}{2m}\sqrt{2m\Phi/\hbar^2}\,\psi_{tip,i}(0)\psi_{sample,f}(d)Ae^{d\sqrt{2m\Phi/\hbar^2}}. \end{aligned} \tag{2.49}$$

From this tunneling matrix we can see, the matrix element does not depend on the position z_s of the separation surface. The energy-dependent of $M(E)$ mainly dependent on k_2 in the exponent. The $T(\Phi, d) = |M(E)|^2$ in the one-dimensional rectangular barrier can be expressed as

$$T(\Phi, d) \propto exp(-2k_2 d) = exp\left(-2d\sqrt{\frac{2m}{\hbar^2}\Phi}\right), \tag{2.50}$$

which is the same energy-dependent term of the $T(\Phi, d)$ in Equation 2.8.

Lastly, we will evaluate the matrix element and the transmission factor based on the effective barrier with the consideration of the difference in the sample and tip work functions, the bias employed, and the tunneling electron energy ε within the bias window.

When the work functions of the tip and sample are different, a trapezoidal potential barrier is generated as shown in Figure 2.5. To simplified this, an effective rectangular barrier is used to represent the trapezoidal barrier. In this case, the average effective barrier is now given as an average work as $\overline{\Phi} = (\Phi_{tip} + \Phi_{sample})/2$. Next, we include the voltage-dependent barrier height into our consideration. Then, the effective tunneling barrier for the states at the sample Fermi level now increases to $\overline{\Phi} + \frac{eV}{2}$ and the effective tunneling barrier for the states at the tip Fermi level decreases to $\overline{\Phi} - \frac{eV}{2}$. In general, the states at energy ε relative to the sample Fermi level now have the tunneling barrier height as $\overline{\Phi} + \frac{eV}{2} - \varepsilon$ as shown in Figure 2.5. Taking together, the effective barrier for an electron tunneling at energy ε relative to the sample Fermi level can be written as

$$\overline{\Phi} = \frac{\Phi_{tip} + \Phi_{sample}}{2} + \frac{eV}{2} - \varepsilon. \tag{2.51}$$

Inserting Equation 2.51 into Equation 2.50, the transmission factor is now as

$$T(\varepsilon, V, d) \propto exp\left[-2d\sqrt{\frac{2m}{\hbar^2}(\frac{\Phi_{tip} + \Phi_{sample}}{2} + \frac{eV}{2} - \varepsilon)}\right]. \tag{2.52}$$

From this equation we can see the transmission factor decrease exponentially for electron at low energy states since the effective barrier height is greater to those electronic states as illustrated by the orange arrows (with different lengths) in Figure Figure 2.5.

If we neglect the pre-exponential factor in Equation 2.49, we can replace $|m(\varepsilon)|^2$ by $T(\varepsilon, V, d)$, and then I is

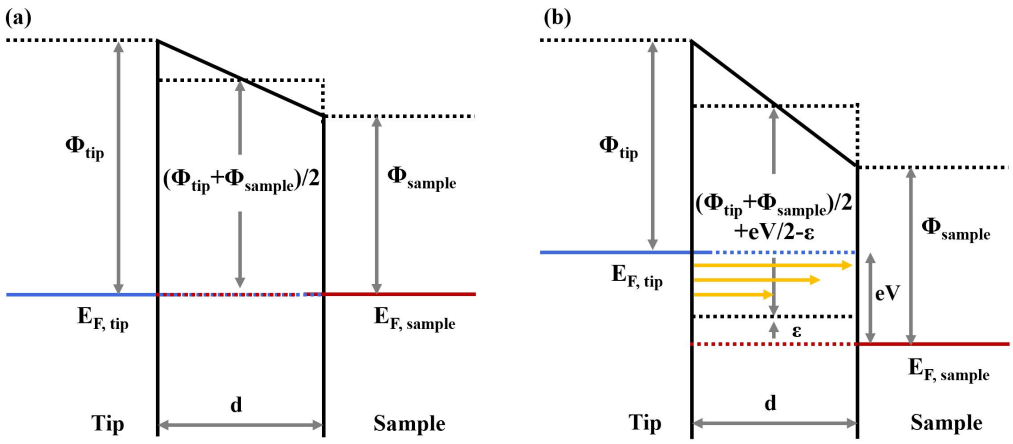

Figure 2.5: (a) Tunneling barrier when the work functions of the tip and the sample are different. (b) Tunneling barrier in (a) with additional bias applied.

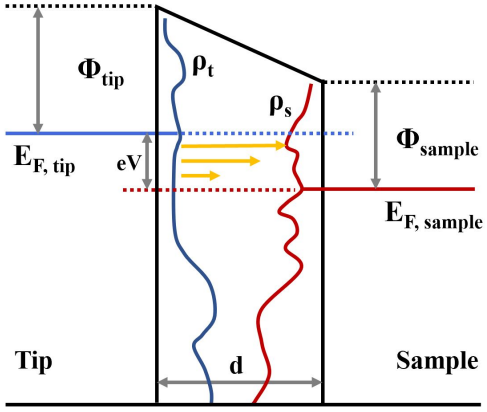

Figure 2.6: Bardeen's approximation for one-dimensional barrier at zero temperature.

$$I = \frac{4\pi e}{\hbar} \int_0^{eV} \rho_{tip}(\varepsilon - eV)\rho_{sample}(\varepsilon)T(\varepsilon, V, d)d\varepsilon. \tag{2.53}$$

This is the Bardeen approach for one-dimensional barrier at zero temperature (graphic shown as Figure 2.6). From this equation we can see I at certain energy ε is proportional to the DOS of both the tip and the sample. Second, the tunneling is energy conservative (only horizontal transition). Third, the tunneling current drops exponentially for states at lower energies because of

a larger effective barrier for at those lower energy states.

In the small voltage case ($eV \ll \Phi$), the ε can be changed by an average energy $\overline{\varepsilon} = (E_{F,tip} + E_{F,sample})/2 = eV/2$. In this case, $T(\varepsilon, V, d)$ does not depend on ε and the voltage applied. I is proportional to the integration of the DOS at both the tip and the sample. For a constant DOS (both tip and sample), this results a proportionality between the current and the voltage.

The discussions above are all at zero temperature. The Fermi-Dirac distribution $f(E - E_f)$ is

$$f(E - E_f) = \frac{1}{1 + exp[E - E_f]/k_B T}, \tag{2.54}$$

which shows the occupation of filled states at energy $(E - E_f)$ and temperature T. Then the unoccupied states can be defined as $1 - f(E - E_f)$. The current ($I^+(E)$) resulted from the electrons tunneling from the occupied states of the tip to the unoccupied states of the sample is

$$I^+(E) = I_{tip,filled \longrightarrow sample,empty} \propto f(E - E_{F,tip})[1 - f(E - E_{F,sample})]. \tag{2.55}$$

The current ($I^-(E)$) resulted from the electrons tunneling from the occupied states of the sample to the unoccupied states of the tip is

$$I^-(E) = I_{sample,filled \longrightarrow tip,empty} \propto f(E - E_{F,sample})[1 - f(E - E_{F,tip})], \tag{2.56}$$

so the total current due to the Fermi-Dirac distribution is

$$I^{total}(E) = I^+ - I^- \propto f(E - E_{F,tip}) - f(E - E_{F,sample}), \tag{2.57}$$

where $E_{F,sample} = 0$ and $E_{F,tip} = eV$. Taking this into account, the tunneling current is now written as

$$I = \frac{4\pi e}{\hbar} \int_{-\infty}^{+\infty} \{f(\varepsilon - eV) - f(\varepsilon)\} \rho_{tip}(\varepsilon - eV) \rho_{sample}(\varepsilon) T(\varepsilon, V, d) d\varepsilon. \tag{2.58}$$

Note that in our approach, the tip and the sample need to have the same temperature. If not, Fermi

functions with different temperature needs to be considered.

In the case of very small bias voltages, Tersoff-Hamann approximation of STM is implemented with additional consideration of surface wave functions. In Tersoff-Hamann model, the matrix element is only evaluated at small bias and at the Fermi level. In Equation 2.46, the wave functions of both tip and sample need to be inserted. A plane wave Fourier expansion is used for the wave function of the surface. However, since the tip structure is usually unknown, it is hard to evaluate the wave function of the tip. In Tersoff-Hamann approximation, the tip is assumed to be an ideal s-wave. A mathematical point source is implemented to represent the tip structure. They have shown that, by using the tip point source at the position $\mathbf{r_{tip}}$, the current at small voltage is now

$$I \propto \sum_n |\psi_n(\mathbf{r_{tip}})|^2 \delta(E_n - E_F), \tag{2.59}$$

which on the right side is the definition for the LDOS. The term $|\psi_n(\mathbf{r_{tip}})|^2$ describes the probability of finding a surface state electron at the position of the tip. In another way of saying, the tip probes the surface wave functions at the position $\mathbf{r_{tip}}$. Thus I can be rewritten as

$$I \propto \sum_n |\psi_n(\mathbf{r_{tip}})|^2 \delta(E_n - E_F) = \rho_{sample}(E_F, \mathbf{r_{tip}}) \tag{2.60}$$

For this reason, Tersoff-Hamann approximation is often employed to interpret STM images based on ab initio simulations.

2.1.2 Scanning Tunneling Spectroscopy (STS)

In STS, the goal is to measure the DOS of the sample. In the simplest approximation, the DOS of the tip and the transmission factor are treated to be voltage independent. Thus, the differential conductance can be written as

$$\frac{dI}{dV} \propto \rho_{sample}(eV). \tag{2.61}$$

In this case, the differential conductance dI/dV measures the DOS at eV relative to to the sample Fermi level.

It is often very helpful to normalize the dI/dV since $T(\varepsilon, V)$ introduces a exponential background with the bias (Equation 2.52). To remove this voltage-dependent exponential background, the normalization can be written as $(dI/dV)/(I/V)$. If we assume a constant DOS of the tip, the $(dI/dV)/(I/V)$ can be written as

$$\frac{dI/dV}{I/V} \approx \frac{\rho_{sample}(eV)T(\varepsilon = eV, V)}{\frac{1}{eV}\int_0^{eV} \rho_{sample}(\varepsilon)T(\varepsilon, V)d\varepsilon} = \frac{\rho_{sample}(eV)}{\frac{1}{eV}\int_0^{eV} \rho_{sample}(\varepsilon)\frac{T(\varepsilon,V)}{T(\varepsilon=eV,V)}d\varepsilon}. \tag{2.62}$$

The ratio of the transmission factors in the denominator is similar, and thus, the normalized differential conductance can be considered to be proportional to the DOS of sample at energy eV. To analyze the dI/dV in more details, we rewrite the Equation 2.53 as

$$I = \frac{4\pi e}{\hbar}\int_0^{eV} \rho_{tip}(\varepsilon - eV)\rho_{sample}(\varepsilon)T(\varepsilon, V)d\varepsilon. \tag{2.63}$$

The Leibniz integral rule is

$$\frac{d}{dx}\int_0^{b(x)} f(t,x)dt = \frac{db}{dx}f[b(x), x] + \int_0^{b(x)} \frac{\partial}{\partial x}f(t,x)dt. \tag{2.64}$$

If we assign $x = V$, $b(x) = eV$, $t = \varepsilon$, $and\, f(t,x) = f(\varepsilon, V) = \rho_{tip}(\varepsilon - eV))\rho_{sample}(\varepsilon)T(\varepsilon, V)$, then the equation Equation 2.64 can be written as

$$\begin{aligned}\frac{dI}{dV}\frac{\hbar}{4\pi e} &= e\rho_{tip}(0)\rho_{sample}(eV)T(eV,V) + \int_0^{eV}\frac{\partial}{\partial V}[\rho_{tip}(\varepsilon - eV)\rho_{sample}(\varepsilon)T(\varepsilon,V)]d\varepsilon \\ &= e\rho_{tip}(0)\rho_{sample}(eV)T(eV,V) \\ &\quad + \int_0^{eV}\frac{\partial\rho_{tip}(\varepsilon - eV)}{\partial V}\rho_{sample}(\varepsilon)T(\varepsilon,V)d\varepsilon \\ &\quad + \int_0^{eV}\rho_{tip}(\varepsilon - eV)\rho_{sample}(\varepsilon)\frac{\partial T(\varepsilon,V)}{\partial V}d\varepsilon.\end{aligned} \tag{2.65}$$

If the DOS for tip is constant, then the second term on the right part in Equation 2.65 disappears. Now the equation Equation 2.65 is

$$\begin{aligned}\frac{dI}{dV}\frac{\hbar}{4\pi e} &= e\rho_{tip}\rho_{sample}(eV)T(eV,V) \\ &\quad + \int_0^{eV}\rho_{tip}\rho_{sample}(\varepsilon)\frac{\partial T(\varepsilon,V)}{\partial V}d\varepsilon\end{aligned} \tag{2.66}$$

where $T(\varepsilon, V, d)$ is

$$T(\varepsilon,V,d) \propto exp\left[-2d\sqrt{\frac{2m}{\hbar^2}(\overline{\Phi} + \frac{eV}{2} - \varepsilon)}\right]. \tag{2.67}$$

Equation 2.67 can be further rewritten as

$$\frac{dI}{dV} = \frac{4\pi e}{\hbar}\left[e\rho_{tip}\rho_{sample}(eV)T(eV,V) - \int_0^{eV}\rho_{tip}\rho_{sample}(\varepsilon)T(\varepsilon,V)\frac{ed\frac{\sqrt{2m}}{\hbar}}{2\sqrt{\overline{\Phi} + (eV/2) - \varepsilon}}d\varepsilon\right]. \tag{2.68}$$

If the fraction part in the second term is approximated as $\frac{ed\sqrt{2m}}{2\hbar\sqrt{\overline{\Phi}}}$, then the Equation 2.68 can be

written as

$$\rho_{sample}(eV) = \frac{\hbar}{4\pi e^2 \rho_{tip} T(eV,V)} \left[\frac{dI}{dV} + \frac{ed\sqrt{2m}}{2\hbar\sqrt{\overline{\Phi}}} I(V) \right]. \tag{2.69}$$

Most of the studies until now focus on the one-dimensional barrier models. In reality, the momentum of an electron has components in all three directions. In the one-dimensional case, only the direction normal to the surface is considered as effective tunneling. This component is $E_\perp = E - E_\parallel$. Thus $T(E,V,d)$ can be written as

$$T(E,V,d) \propto exp\left(-2d\sqrt{\frac{2m}{\hbar^2}\overline{\Phi} + \frac{eV}{2} - (E - E_\parallel)} \right). \tag{2.70}$$

In addition to the $I-V$ spectroscopy, if I is measured as a function of Z between the tip and the sample, then the effective barrier $\overline{\Phi}$ can be measured. At low bias region, the tunneling current does not depend on the voltage and the energy, then I can be approximated as

$$I(\overline{\Phi}, d) \propto exp\left(-2d\sqrt{\frac{2m}{\hbar^2}\overline{\Phi}} \right). \tag{2.71}$$

2.2 Atomic Force Microscopy (AFM)

Another powerful scanning probe technique is the atomic force microscopy (AFM) which can resolve surface features with detailed information in many environmental conditions. In AFM (Figure 2.7), a sharp tip at the end of a cantilever is brought into contact with a sample surface. The interaction between the tip and the sample forces the cantilever to bend. On the backside of the cantilever, a laser spot is reflected to a quadrant photodiode detector. The position of the laser spot on the photodetector depends on the bending or twisting of the cantilever and thus, varies as a function of the tip-sample interaction. The tip-sample interaction is complex as multiple forces can participate into this playground. Generally, the forces can be separated into attractive and repulsive forces. In attractive region, there are van der Waals force, electrostatic force and chemical force. In repulsive region, there are hard sphere repulsion, Pauli-exclusion interaction

and Coulomb interaction [64].

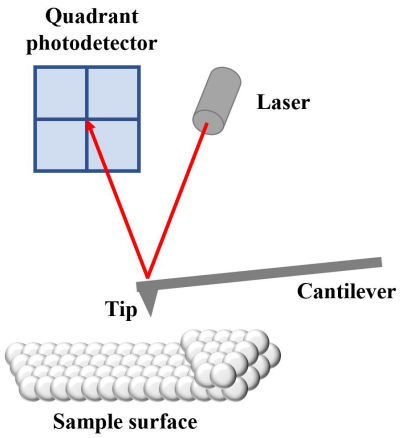

Figure 2.7: Basic model for AFM.

Based on the difference in the force regions, the two most commonly used AFM modes are contact mode and intermittent contact mode. In contact mode, the AFM tip is brought into contact with the sample and scanned across the surface. In response to the surface topography, a feedback loop is implemented to keep the deflection of the cantilever constant, and therefore keeping the tip-sample force constant as well. In intermittent contact mode, first, the cantilever is driven to oscillate near its resonance frequency. Next, the cantilever is brought into a close distance to the sample where both attractive and repulsive forces affect the motion of the cantilever and change the amplitude, phase and resonance frequency of the cantilever. Again, a feedback loop is implemented to maintain a constant oscillating amplitude of the cantilever. The topography is obtained correspondingly as the tip tapping across the surface. Besides imaging, AFM has also been employed for more advanced data acquisition on surface properties. During scanning, for example in contact mode, additional lateral information is obtained as the cantilever being twisted due to the frictional forces between the tip and the sample. Through standard normal and lateral cantilever calibration, quantitative frictional forces as a function of the applied loads can be measured and assessed for different samples. In addition to the frictional characterization, AFM can be employed

to measure the mechanical properties of the sample surfaces. In the method called force-distance curves or force-distance maps, the ATM tip is brought into contact, pressed, and retracted from the sample surface. In this process, the spatially resolved surface stiffness (Youngs modulus) is measured as well as the adhesion between the tip and the sample.

2.3 Raman Spectroscopy

In 1928, an Indian physicist C.V Raman, discovered the inelastic scattering behavior of certain molecules in response to visible photon radiation and three years later, he was awarded the Nobel Prize in physics for his discovery. However, until the last a few decades, Raman spectroscopy started to be widely used as a route technique due to the invention of laser, array detector and the commercialization of modern electronics [65].

The basic mechanism for Raman spectra is shown below. In Figure 2.8, a sample is irritated with a beam of photons. The sample in the ground vibrational state can be excited to a virtual state and then relax back to its ground state with additional photon emission. If the emitted photon has the same energy as the exciting photon, the scattering process is call Rayleigh scattering. If the emitted photon has a low energy compared to the radiation energy, the scattering process is called Stokes scattering. If the emitted photon is of a higher energy than the source energy, the scattering process is named as anti-Stokes scattering.

Next, lets discuss the wave model of Raman scattering. The electric field can be written as

$$E = E_0 \cos(2\pi v_{ex} t). \tag{2.72}$$

This electric field with induce a dipole moment m in the bond which is

$$m = \alpha E = \alpha E_0 \cos(2\pi v_{ex} t), \tag{2.73}$$

where α is the polarizability of the bond. The polarizability α is a function of nuclear distance

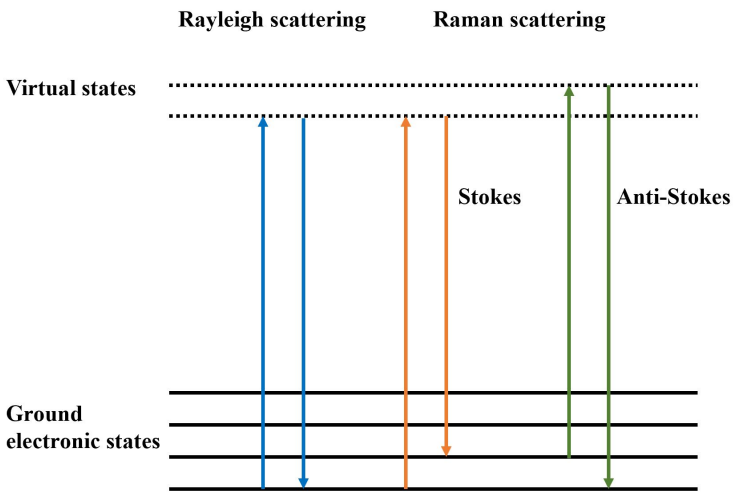

Figure 2.8: Schematic of Rayleigh, Stokes and anti-Stokes Raman scatterings.

which is

$$\alpha = \alpha_0 + (r - r_{eq}) \left(\frac{\partial \alpha}{\partial r} \right), \tag{2.74}$$

where the α_0 is the polarizability at equilibrium distance r_{eq}. The inter-nuclear distance as a function of vibration frequency is

$$r = r_{eq} + r_m \cos(2\pi v_v t), \tag{2.75}$$

where the r_m is the maximum nuclear distance minus the equilibrium separation. Inserting Equation 2.75 to Equation 2.74 gives,

$$\alpha = \alpha_0 + \left(\frac{\partial \alpha}{\partial r} \right) r_m \cos(2\pi v_v t). \tag{2.76}$$

By inserting Equation 2.76 into Equation 2.73, we can get the induced dipole moment which is

$$m = \alpha E = \alpha_0 E_0 \cos(2\pi v_{ex} t) + E_0 r_m \left(\frac{\partial \alpha}{\partial r} \right) \cos(2\pi v_v t) \cos(2\pi v_{ex} t). \tag{2.77}$$

Since

$$\cos x \cos y = [\cos(x + y) + \cos(x - y)]/2, \tag{2.78}$$

we can rewrite Equation 2.77 as

$$m = \alpha_0 E_0 \cos(2\pi v_{ex} t) + \frac{E_0 r_m}{2}\left(\frac{\partial \alpha}{\partial r}\right)\cos[2\pi(v_{ex} - v_v)t] + \frac{E_0 r_m}{2}\left(\frac{\partial \alpha}{\partial r}\right)\cos[2\pi(v_{ex} + v_v)t]. \tag{2.79}$$

The first term in Equation 2.79 corresponds to the Rayleigh scattering, the second term and the third term relate to the Stokes and anti-Stokes shifts separately. Note that in order to observe the Raman shift, the selection rule requires a change in the polarizability.

2.4 X-Ray Photoelectron Spectroscopy (XPS)

The history of x-ray photoelectron spectroscopy (XPS) could be traced back to nineteenth century, when Heinrich Hertz found that the ability for metals to spark could be improved greatly if exposed to light. In 1905, Albert Einstein explained this photoelectric effect which won him a Nobel Prize in Physics. However, not until the innovative work carried out by Kai Siegbahn and his coworkers in fifties, then the abilities of XPS were fully recognized. Kai Siegbahn was awarded a Noble Prize in Physics in 1981 for his dedicated work on it.

In a XPS spectrum, surface information for a sample can be revealed as the the binding energy positions, the intensities and the shapes of different peaks. Taking a metal sample surface as an example, the sample is electrically connected to the spectrometer. Therefore, the relationship between the kinetic energy and the binding energy is given by

$$E_{kin} = hv - E_B - e\Phi_{sp}, \tag{2.80}$$

where Φ_{sp} is the work function of the spectrometer, instead of the sample. The binding energy in the equation is thus, referred to the Fermi level of the spectrometer rather than the vacuum level (Figure 2.9).

In addition to the physical principle discussed above, detailed discuss about XPS is demonstrated below, particularly focusing on the shift in binding energies. After absorbing a photon with energy hv, an atomic system with N electrons is excited from an initial state into a final state ion

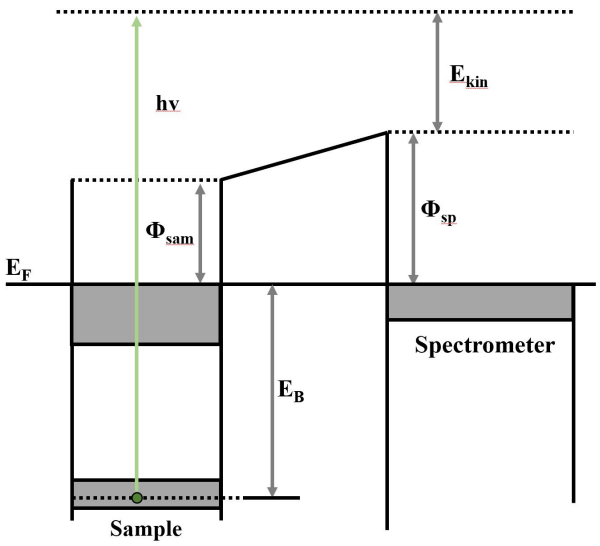

Figure 2.9: Energy level diagram for x-ray photoelectron process.

plus a photoelectron with a kinetic energy of E_{kin}. The N electrons system can be described by a set of wave functions and energy states. Consequently, the energy change during this process can be simply derived as:

$$E^i(N) + hv = E^f(N-1,k) + E_{kin}, \tag{2.81}$$

where k stands for the energy from which the electron has been removed. The simplified approach is to assume that the energy and spatial distribution of the $N-1$ electrons remain the same as initial before the excitation. Then the binding energy for the excited electron is equal to the negative orbital energy,

$$E_B(k) = -\varepsilon_k. \tag{2.82}$$

This is called the Koopmans' approximation. However, several effects are not considered in this model, for example, the neglect of relativistic and correlation effect as well as the associated relaxation energy which usually leads to a reduction of the binding energy for the ejected electron. The binding energy will be more accurate by taking these factors into account. In addition of identifying the position for binding energy, the peak intensity also need to be defined. The peak intensity is determined by the photoelectric cross section σ, which is proportional to the squared

matrix element $|M_{if}|$. However, the real scenario is far more complicated. The core-level binding energy of a certain atom may shift up or down depending on the oxidation state or lattice position. The change of the binding energy ΔE_B for a particular element in various chemical environments can be attribute to those from the initial state effect and final state effect [66].

Initial state effect describes the effect resulting in any change of the binding energy that is present prior to the photoelectron exciting process. There are two main contributions for the initial state effect: spin orbit splitting and Coulomb interaction. Spin orbit splitting describes the phenomenon that a spinning charge in a non-symmetrical orbit $(l > 0)$ will experience a splitting in its energy state depending on the spin up or the spin down separations.

Another contribution for the initial state effect is the Coulomb interaction which describes the influence of the local charge density on the binding energy of the excited photoelectron. This interaction is often seen in the forms of the oxidation states, coordination numbers or bonding lengths. The physical basis can be explained by the so-called charge potential model [67, 68]. The model describes that the ΔE_B of atom i is a function of its own charges and the charges from the surrounding atom j,

$$\Delta E_B \propto (k\Delta q_i + \Delta \sum_{i \neq j} q_j / d_{i-j}) \tag{2.83}$$

where k stands for the coupling constant and d_{i-j} stands for bond length. An example for the Coulomb interaction is when an atom is oxidized, its own electron charge density decreases, which will lead to a up-shift of the core-level binding energy.

Final state effect describes the effect that arises from photoelectron emission, particularly the perturbation of the electronic structure after the electron excitation. The core hole formation after the photoelectron emission affects the electron emitted in numerous ways including relaxation effect, multiplet splitting, and valence electron excitation.

Relaxation effect describes the phenomenon that, after the formation of the core hole, the remaining electrons relax in order to decrease system total energy. The reason behind is quite simple. The removal of an electron will increase the bonding for the rest electrons since the nucleus's attraction to all the remaining electrons is shared by less electrons. This will decrease the valence

electron radius and thus increase the screening effect for the ejected electron. In the end, the photoelectron binding energy will decrease. Usually the relaxation effects can be separated into two parts [69–71]: an intra-atomic term and an inter-atomic term. For metals, the inter-atomic term can be as large as 5 to 10 eV which tends to neutralize the core hole by screening electrons from the conduction band. The multiplet splitting, which is similar to the spin orbit splitting, stems from the interaction between the unpaired remaining core-level electron and the unpaired valence electrons. This will lead to the splitting of peaks at higher binding energy. Lastly, the core hole formation can also lead to the excitation of valence electrons. If the relaxation process of the excited electron is beyond the time scale of the photoelectron emission, the ejected photoelectron will have less kinetic energy and therefore, higher binding energy. If an electron in the valence band is excited to a higher orbital, the corresponding peaks are referred as "shake-up" satellites. If an electron is excited from valence band into free continuum bands, the corresponding lines in spectrum are called "shake-off" satellites. If high density of electron-hole pairs are excited around the Fermi level, the corresponding process is named as plasma, which usually shows an oscillation feature in the satellite lines.

3. FORMATION OF COHERENT 1H-1T HETEROSTRUCTURES IN SINGLE LAYER MOS2 ON AU(111)*

3.1 Introduction

Two-dimensional (2D) transition metal dichalcogenides (TMDCs) have attracted tremendous attention over the past decade due to the exciting mechanical, electronic and frictional properties [1–8]. Different from graphenes atomically thin structure, 2D-TMDCs (general formula MX_2) consist of a transition metal M layer (*e.g.* W, Mo, Nb), sandwiched between two layers of chalcogen X atoms (*e.g.* S, Se, Te) [72]. Like graphene and other layered materials, 2D-TMDCs can also be easily cleaved from their bulk crystals due to the weak van der Waals interactions between layers [7, 43, 44, 73–76]. The electronic properties of bulk TMDCs can be metallic (*e.g.* NbS_2), semi-metallic (*e.g.* WTe_2), semiconducting(*e.g.* MoS_2), or insulating (*e.g.* HfS_2) [7]. Additionally, some TMDCs such as $NbSe_2$ and TaS_2 exhibit superconductivity, and undergo a Mott transition at low temperatures [77–79]. Synthesizing single- and few-layer MX_2 preserves their bulk properties, while additionally leading to exciting properties due to the quantum confinement and surface effect. Therefore, 2D-TMDCs have become emerging materials with promising potentials for solid lubricants [80, 81], hydrogen evolution reactions [82–89], ion batteries [90–93], catalysts [39, 40, 94], supercapacitors [95–97], superconductors [78, 98–100], piezoelectric materials [101–103], electronics [9, 104–106], and optoelectronic devices [9, 107–110].

Molybdenum disulfide (MoS_2), a well-known TMDC, can form two common polymorphs, *i.e.*, 2H-MoS_2 and 1T-MoS_2, based on the Mo coordination and the stacking orders. In particular, 2H-MoS_2 has a trigonal prismatic structure with a P63/mmc symmetry while 1T-MoS_2 has an octahedral structure with a P3 symmetry. These two polymorphs show considerable differences in their electronic structure due to the variation in the crystal symmetry. 2H-MoS_2 exhibits a semiconducting feature with a band gap between the d_{z^2} and the d_{xy}, $d_{x^2-y^2}$ sub-bands, while 1T-

*Reprinted with permission from Wu, F.; Liu, Z.; Hawthorne, N.; Chandross, M.; Moore, Q.; Argibay, N.; Curry, J. F.; Batteas, J. D. Formation of Coherent 1H-1T Heterostructures in Single-Layer MoS_2 on Au (111). *ACS nano* **2020**, *14* (12), 16939-16950. Copyright 2020 by American Chemical Society.

MoS_2 shows a metallic behavior with Fermi level lying inside the $d_{xy,yx,xz}$ single band [111]. The naturally abundant 2H-MoS_2 is widely known for its application in solid lubricants [80, 81], hydrodesulphurization catalysis [94], hydrogen evolution reactions [82, 84–89], photovoltaics [112], and lithium ion batteries [91–93, 113]. When the thickness of 2H-MoS_2 is reduced from bulk to a single layer, the nature of the electronic band structures changes from an indirect bandgap (1.2 eV) [114] to a direct bandgap (1.9 eV) [115]. Furthermore, due to symmetry breaking and spin-orbital coupling, a large splitting emerges at the K valleys in monolayer 2H-MoS_2. (we note that monolayer 2H-MoS_2 is also called 1H-MoS_2, and will be referred to as such for the remainder of this paper). These promising behaviors open up new possibilities of utilizing single-layer 1H-MoS_2 in optoelectronics, spintronics and valleytronics [9–13]. The 1T-MoS_2 phase (distorted version: 1T') is thermodynamically metastable, and tends to restack to a more stable 1H-MoS_2 phase by gentle annealing or aging [26]. Recently, the 1T phase has drawn great attentions for its topological properties, since the quantum spin Hall effect, dipolar ferroelectricity and Wely semi-metallicity have all been observed both experimentally and theoretically in MoS_2, $MoTe_2$ and WTe_2 [14–17].

Heterostructures of semiconductors and metals are the fundamental components of modern electronics [116]. 2D materials like graphene and 2D-TMDCs offer unprecedented opportunities in fabricating heterostructures for light emitting devices, high mobility transistors and photovoltaics. Historically, 2D heterostructures have been achieved through horizontal packing of various layered materials by chemical or mechanical techniques [117–120]. The atomically thin MoS_2 sheets, however, offer unique opportunities for heterostructure devices since they are chemically homogenous and electronically distinct (*e.g.* semiconducting 1H phase and metallic 1T phase, side by side with matched lattices). Possible applications include atomically thin Schottky diodes, field effect transistors and other optoelectronic devices [121]. To date, coherent heterostructures of single-layer MoS_2 have be formed by alkali metal interactions [122], metal substitutional doping [123], negative charging [124], strain [125], or irradiation by plasma [126], electron beams and lasers [127]. Given the complexity of these approaches, a facile way to fabricate high-quality monolayer MoS_2

heterostructures is therefore desirable for both fundamental research and applications development. Single-layer MoS_2 heterostructures were first synthesized by alkali metal interaction [7, 122]. Besides the difficulty in handling alkali metals, the tendency for aggregation and the contamination from the solvents make it a challenging approach. Chemical vapor deposition (CVD) yields large-area monolayer MoS_2 [27, 128, 129], but it is still difficult to grow single layers continuously at macroscale levels, not to mention the extensive time and cost. Recently, electrochemical exfoliation of large-scale MoS_2 has been reported. However, the intrinsic drawback in the process usually results in the partial oxidization of the resulting monolayers [95]. Compared to these methods, mechanical exfoliation yields the highest quality monolayers. Nonetheless, by using this technique, particularly the scotch-tape approach on SiO_2 substrates, the lateral size of the exfoliated MoS_2 is usually on the order of micrometers, one order of magnitude smaller than the graphene counterpart [9, 108, 130]. Furthermore, the mechanically exfoliated MoS_2 flakes are typically pristine 1H phase, which hinders their potential applications in heterostructure electronic devices.

Herein we exploit a modified mechanical exfoliation technique to prepare monolayer MoS_2 heterostructures (1H and 1T). The extent of exfoliation is found to be significantly enhanced when transferring to Au(111) substrates since Au is well-known for its strong affinity to sulfur [131, 132]. Our approach is derived from the well-known scotch-tape method, and is found to leave no tape residue as has been found in other exfoliation methods. Moreover, by transferring the MoS_2 onto Au, single layer MoS_2 can be deposited with feature sizes of up to millimeters in lateral dimension. Raman, XPS, and STM/STS collectively elucidate the resulting heterostructures in single-layer MoS_2 on Au. Additionally, we show that bubbles of trapped ambient adsorbates under the MoS_2 can be formed and manipulated by AFM.

3.2 Results and Discussion

3.2.1 Mechanical Exfoliation Technique for Monolayer MoS_2

During mechanical exfoliation, it is possible to achieve single-layer MoS_2 because the adhesion of the basal plane to the substrate is stronger than the adhesion to its bulk crystal [132, 133].

Previous work depositing MoS_2 on SiO_2 substrates usually resulted in single layer flakes with lateral sizes in the micron range [104, 134, 135], which are much smaller as compared to the graphene counterpart (tens of microns) [136]. Exfoliation yields can be significantly enhanced by improving the adhesion to the substrates. Here, as reported by Velicky *et al.*, by using Au substrates, adhesion is further increased, affording large area fabrication [19], without introducing tape residues typically seen in numerous related scotch-tape methods [19, 43, 44].

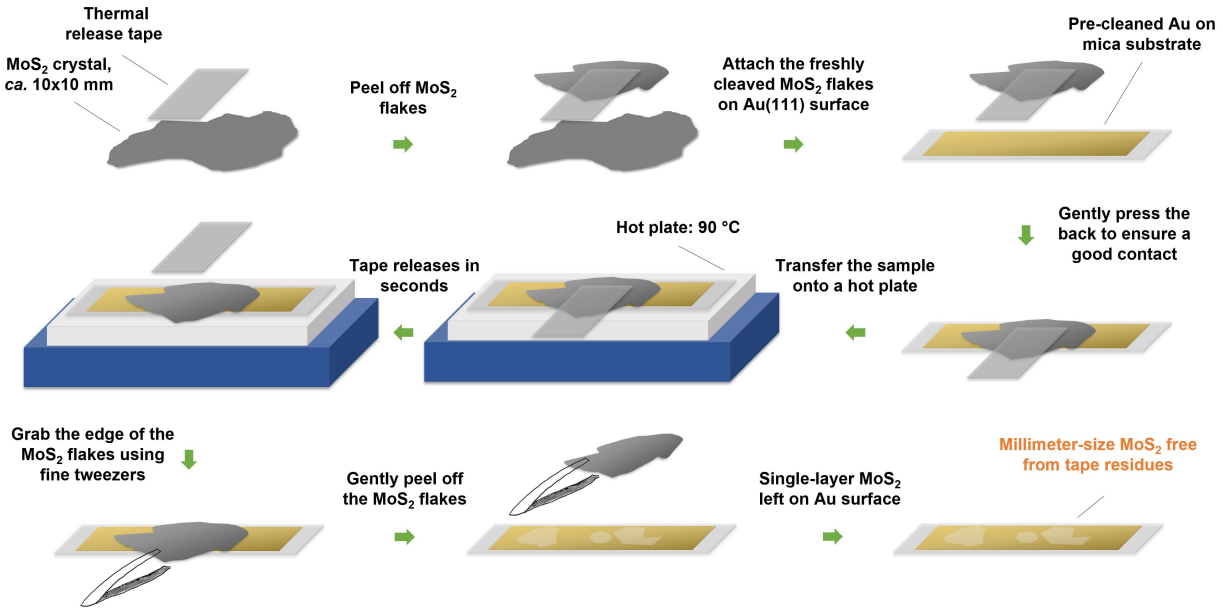

Figure 3.1: Schematic illustration of the facile mechanical exfoliation technique enabling monolayer MoS_2 free from tape residues, up to millimeter scale.

Figure 3.1 demonstrates our modified procedure for creating millimeter-size monolayer MoS_2. Prior to exfoliation, the Au(111) substrates were treated with UV/ozone for 15 minutes [137], followed by rinsing in sequence with ultrapure water (18.2 MΩ·cm) and ethanol. Next, Au substrates were dried with streaming nitrogen. Then, thick MoS_2 flakes were cleaved off from a bulk MoS_2 single crystal using a thermal release tape and immediately attached onto the Au surfaces. This step was critical which required direct contact between the freshly prepared MoS_2 flakes and Au substrates. The crystal flakes should be large enough to cover the whole Au and thick enough

that the tape did not touch the Au. In addition, this process needed to be done within one minute in order to minimize exposure to air contaminants. Moreover, exfoliating MoS_2 flakes too many times would divide the flakes into small fragments and degrade the film quality. Therefore, our MoS_2 flakes were cleaved only once or twice before attaching to the Au substrates. Following that, a downward pressure was employed to the back of the tape to ensure a good contact between the MoS_2 and the Au substrates. The sample was then transferred onto a hot plate at 90 °C where the thermal tape was released within a few seconds. Instead of immediately removing it from the hot plate, the sample was annealed for an additional 60 s. Finally, different from other mechanical exfoliation techniques, fine tweezers were implemented to grab the edge of the MoS_2 and gently peel off the crystal, leaving the bottom single-layer MoS_2 attached to the Au surfaces. The entire deposition was conducted in a laminar flow hood to mitigate environmental contaminants (*e.g.* dust). The sample was then transferred and stored in a UHV chamber ($\sim 10^{-10}$ mbar) for future characterization.

3.2.2 Optical, AFM, Raman, and XPS Characterization of Monolayer MoS_2 on Au(111)

Figure 3.2a illustrates a macroscopic optical photograph of MoS_2 freshly exfoliated onto Au(111). Single-layer MoS_2 can be recognized as the areas with a faint color contrast. The optical image reveals that single-layer MoS_2 has a decent crystal uniformity with millimeter size. Similar result can also be found in Figure 3.3. Cracks and breaks are barely observed inside the films. To further confirm the single-layer nature of the MoS_2, AFM experiments have been performed. The AFM topography image in Figure 3.2b shows a representative area containing both monolayer MoS_2 and Au which unambiguously indicates a clean surface in both MoS_2 and Au regions. Note that on the MoS_2 films (left side of the image), bright protrusions are visible over the whole area. These are MoS_2 bubbles containing trapped ambient adsorbates formed during the film transfer (also commonly seen in graphene transfers), which has been recently suggested to be predominately trapped water [138]. The corresponding friction image (Figure 3.2c) demonstrates the uniformity of the MoS_2 films as well as the chemical character of these bubbles, *e.g.*, in the circled locations, where the same friction is observed for both bubbled and flat MoS_2 regions, indicating that the

protrusions in the topography are part of the contiguous MoS_2 layer and not from tape residues or other environmental contaminants (STS measurements, described later, also verify the chemical/electronic character of these bubbles). Moreover, the universal defects (vacancy islands and dark pits) on the Au region are not seen in either AFM topography or friction images after being fully covered by MoS_2. The black line profile from Figure 3.2d measures the step height of the MoS_2 in Figure 3.2b and the blue line profile determines the physical height of a representative bubble in Figure 3.2b. The measured MoS_2 thickness ranges from 0.6 nm to 0.8 nm, confirming the single-layer character of the exfoliated MoS_2 flakes. The height of the bubbles ranges from 0.5 nm to 10 nm, and the width of the bubbles ranges from 10 nm to 100 nm based on the AFM measurements (tip radius of curvature $\sim$15 nm). Detailed statistics are provided in Figure 3.5. Raman spectra (Figure 3.2e) have also been employed to probe the layer thickness and the chemical character of the as-exfoliated MoS_2.

Among the four Raman modes of the bulk 2H-MoS_2 crystal, only two Raman peaks near 400 cm^{-1} ($E^1{}_{2g}$ and A_{1g}) have been observed. The other two modes (E_{1g} and $E^2{}_{2g}$) cannot be detected because of the selection rules for E_{1g} [139] and the limited rejection of Rayleigh scattering radiation for $E^2{}_{2g}$ [140]. The reference bulk 2H-MoS_2 exhibits $E^1{}_{2g}$ (in-plane) vibrational mode at 384.0 cm^{-1} and A_{1g} (out of plane) vibrational mode at 409.0 cm^{-1}. The frequency difference $\Delta\omega$ $\sim$ 25 cm^{-1}, agrees well with the values reported in literature for bulk MoS_2 crystals [141–143]. The bottom MoS_2 Raman spectrum in Figure 3.2e exhibits $E^1{}_{2g}$ vibrational mode at $\sim$379.9 cm^{-1} and A_{1g} vibrational mode at $\sim$398.4 cm^{-1}. The frequency difference $\Delta\omega \sim 18.5$ cm^{-1} indicates the single-layer exfoliation of MoS_2, and shows consistency with previous reports [141–143]. Generally, on insulating substrates, *e.g.* SiO_2, the $E^1{}_{2g}$ peak softens (red-shift), while the A_{1g} vibrational mode stiffens (blue-shift) with increasing layer thickness [141, 143]. The blue-shift of the A_{1g} peak has been explained by a classical model for coupled harmonic oscillators [115], in which the additional van der Waals forces increase the effective restoring forces on the atoms. The anomalous red-shift of the $E^1{}_{2g}$ peak has been attributed to the stacking-induced structural changes as previous low-energy electron diffraction (LEED) showed that the distance between the Mo and S

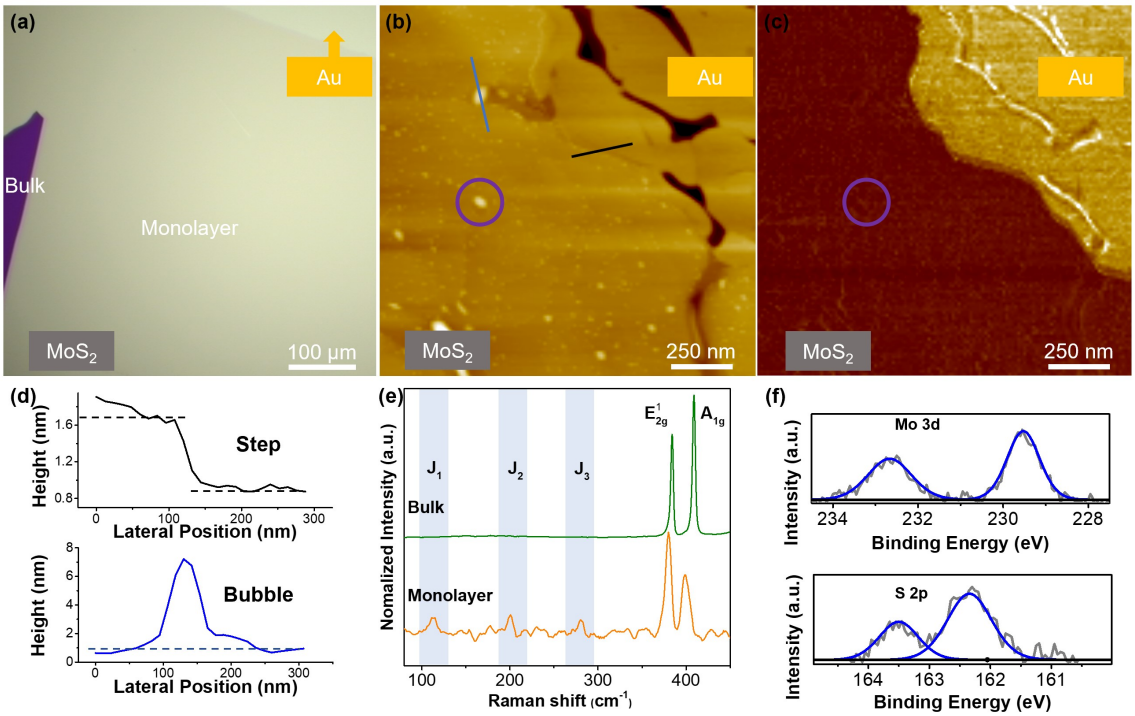

Figure 3.2: Characterization of the MoS_2 monolayers on Au(111). (a) Optical photograph of single-layer MoS_2 on Au(111) of millimeter size. (b) AFM topography image (load: 1 nN) showing monolayer MoS_2 and substrate Au. Both areas are free from tape residues. The bright protrusions, *e.g.*, in the circled location, are bubbles formed during the transfer. (c) Corresponding AFM friction image showing monolayer MoS_2 and Au regions. (d) Height profiles taken across the edge and the bubble along the directions marked by the black and blue lines in (b), respectively. (e) Raman spectra of the monolayer MoS_2 and the reference bulk crystal. In the shaded areas, weak J_1, J_2 and J_3 peaks are observed for the monolayer MoS_2, indicating the existence of a small portion of 1T phase inside the monolayers. (f) Mo 3d and S 2p core level XPS spectra of MoS_2 monolayers.

planes inside the topmost layer diminishes by 5% as compared to the bulk [144]. However, in our Raman spectra (Figure 3.2e), a blue-shift has been observed for the E^1_{2g} peak ($\sim$379.9 cm^{-1} for single layer shifted to $\sim$384.0 cm^{-1} for bulk crystal), indicating a strong interaction between the MoS_2 and the Au which may be caused by efficient charge transfer from substrate Au [19, 124]. In addition, the line width shrinks when the layer thickness increases from single to bulk. This reflects the presence of various effects on the vibrational modes of the monolayers compared to the bulk where the uniform inter-layer interaction dominates the bulk Raman peaks. Besides the charge transfer and the thickness effects on the Raman shift, our E^1_{2g} peak for single-layer MoS_2 ($\sim$379.9

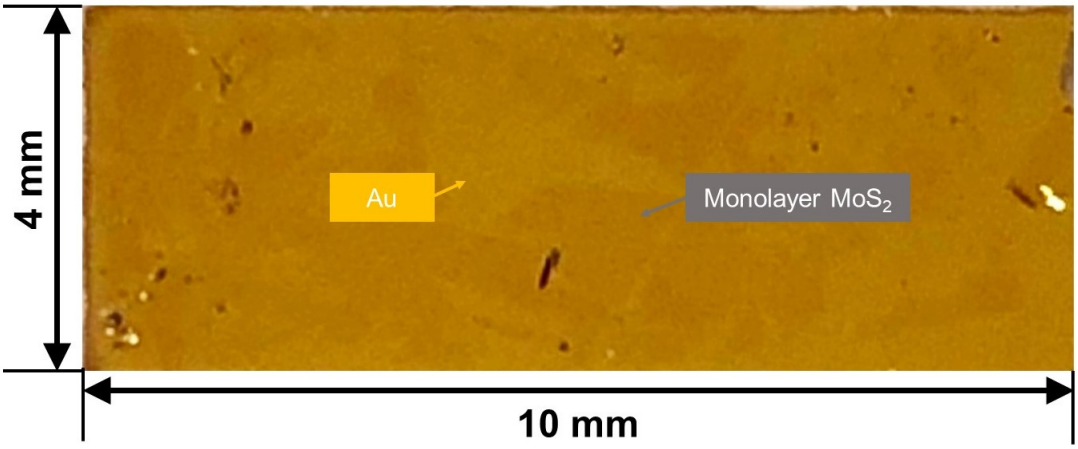

Figure 3.3: Optical photograph of single-layer MoS_2 on Au(111) of millimeter size.

cm^{-1}) has appeared red-shifted as compared to the E^1_{2g} peak of MoS_2 monolayer on SiO_2 (∼384 cm^{-1}) [143, 145]. This shift is consistent with a tensile strain being introduced into the MoS_2 from the Au substrates, since tensile strain usually leads to a red-shift while compressive strain leads to a blue-shift in the MoS_2 Raman spectra [145, 146]. Because of the strong adhesion between the Au substrates and the MoS_2, the monolayer could be mechanically coupled to the Au surface with friction, and the strain could possibly be engineered into the MoS_2 films due to the thermal expansion coefficient mismatch during the mechanical exfoliation process (recall that the samples have been heated up to 90 °C to release the thermal tape) [147]. Usually, peak splitting is expected for E^1_{2g} mode since the double degeneracies of E^1_{2g} are orthogonally polarized. However, this has not been observed, possibly due to the broadening effect as well as the resolution limitation [145]. Besides the E^1_{2g} peak and the A_{1g} peak typically observed in both monolayer and bulk, three additional peaks, J_1 (113.6 cm^{-1}), J_2 (200.7 cm^{-1}) and J_3 (280.3 cm^{-1}) have been detected in the monolayer MoS_2, suggesting the existence of the 1T phase embedded in the monolayer 1H phase MoS_2. XPS was used to further understand the electronic properties of the single layer MoS_2/Au(111) system (Figure 3.2f). The signals at 229.4 eV and 232.6 eV can be identified as Mo($3d_{5/2}$) and Mo($3d_{3/2}$) from single-layer 1H-MoS_2. Similarly, the signals at 162.3 eV and 163.5 eV can be assigned as S($2p_{3/2}$) and S($2p_{1/2}$) from single-layer 1H-MoS_2. However, because of the relative low single-to-

noise ratio for single layer MoS_2, the deconvolution of those peaks is difficult, and we could not confirm the existence of the 1T phase by XPS.

3.2.3 Atomistic Structures and Electronic Properties of Monolayer MoS_2 on Au(111)

To investigate the atomistic structures and electronic properties of single-layer MoS_2 on the Au(111) surface, detailed STM and STS experiments have been employed. In Figure 3.4a, the single-layer MoS_2 can be easily distinguished from the Au substrate. The black and blue line profiles from Figure 3.4b measure the height of a MoS_2 flake and the height of a bubble from Figure 4(a). The determined apparent height of the MoS_2 flake relative to the Au substrate is *ca.* 0.24 nm, which agrees with previous reports for single-layer MoS_2 on Au substrates by STM [41, 148–151]. Note that the apparent height measured in STM is a convolution of both electronic and geometric effects, and differs from the physical height measured with AFM. Additionally, the apparent height of the representative bubble is *ca.* 2 nm and the lateral size is *ca.* 50 nm. A detailed size distribution is provided in Figure 3.5. A zoomed-in atomic resolution STM image (Figure 3.4c) of certain area illustrates the hexagonal moiré structure formed by MoS_2 on Au(111) plane, again confirming that MoS_2 is single-layer. The line profile in Figure 3.4d shows the plane and also confirms that MoS_2 is single layer. The line profile in Figure 3.4d shows the periodicity to be *ca.* 3.15 nm and the height corrugation *ca.* 0.55 Å.

To reveal the electronic structures of MoS_2 on Au(111), STS has been implemented to probe the electronic variation along the moiré pattern as well as the bubbles. The feedback system was turned off for the voltage sweep and the corresponding tunneling current was recorded. During atomic-resolution STM imaging, the I-V spectra were simultaneously collected at specific points. Then, derivatives (dI/dV) of the averaged I-V curves were numerically calculated. Figure 3.4e shows the dI/dV curves for three different spots on single-layer MoS_2/Au(111). The dI/dV curve is a first approximation of the local density of states (LDOS) as a function of energy close to the Fermi level, and illustrates the electronic structures of the MoS_2/Au(111) system. A, B and C spectra in Figure 3.4e follow a similar trend in different bias regions, showing a typical semiconducting character which varies from the metallic Au substrates (see Figure 3.6, for full STM/STS

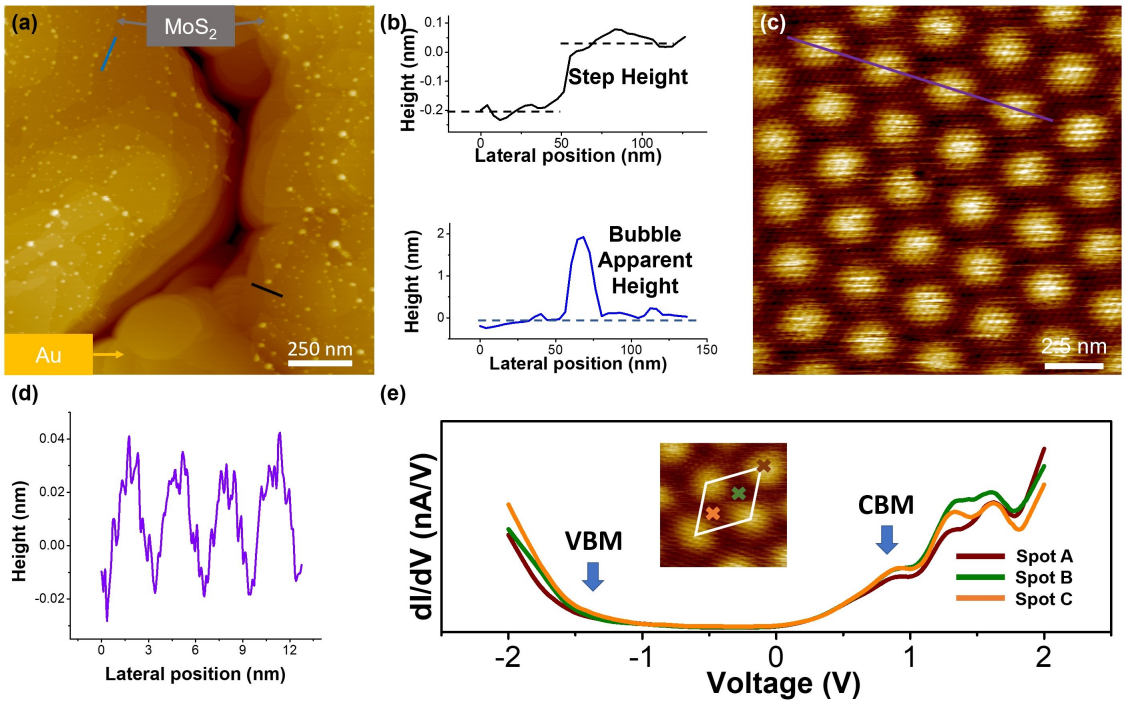

Figure 3.4: STM/STS characterization of the MoS_2 monolayers on Au(111) surfaces. (a) Large-scale STM image (V_{bias} = +500 mV, I_t = 0.5 nA) of single-layer MoS_2 flakes on Au(111). (b) Line profiles taken across an edge and a bubble along the directions marked by the black and the blue lines in (a). (c) High resolution STM image (V_{bias} = +100 mV, I_t = 0.5 nA) of single-layer MoS_2 on Au(111) showing the moiré periodicity. (d) Line profile showing the periodicity and the corrugation of the moiré patterns in (c). (e) STS spectra of the single-layer MoS_2/Au(111) on three different spots, shown in the inset STM image. The set point used to stabilize the tunneling gap is +500 mV and 0.5 nA. The plots are numerically calculated derivatives (dI/dV) of 100 averaged I-V curves for each location. VBM is the valance band maximum, and CBM is the conduction band minimum.

characterization of Au surfaces). However, there is still a small difference between dark regions B, C and the bright spot A, where B and C show a higher dI/dV value close to the CBM and thus, a higher LDOS. These three spots can be assigned to three distinct superstructures: (A) S on top of Au atoms; (B) Mo and S in or near fcc hollow sites; and (C) S in Au fcc hollow sites and Mo on top of Au atoms [28]. The differences in dI/dV indicate that the hybridized LDOS of the MoS_2/Au(111) system is influenced by the stacking configurations. In the B and C regions, a stronger out-of-plane orbital coupling is observed compared to the A region [28]. The width of the band gap for single-layer MoS_2 on Au is not easy to assign, because of the broadening effect at

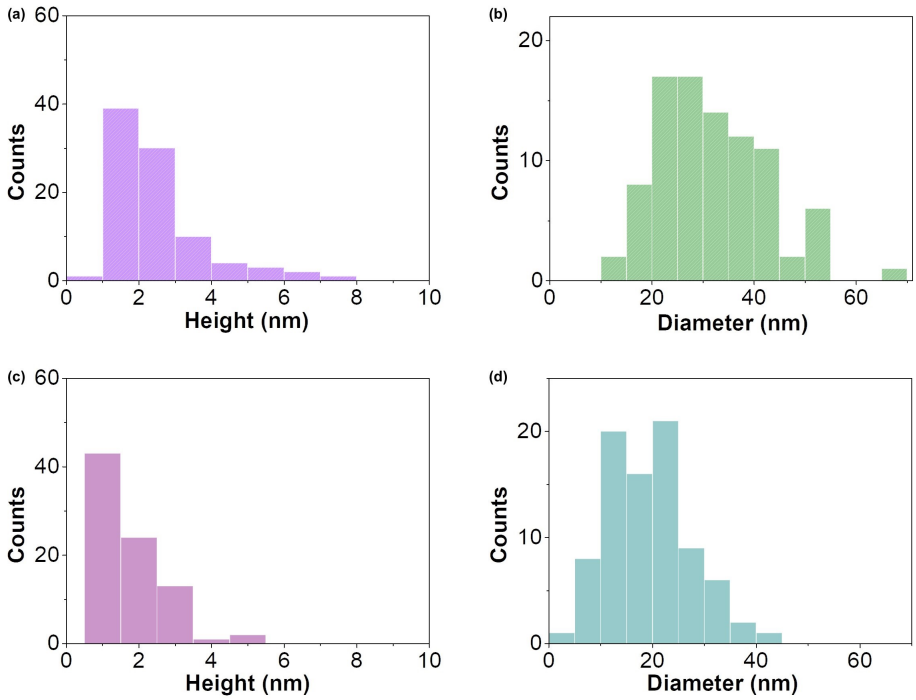

Figure 3.5: Size distribution of monolayer MoS_2 bubbles measured by AFM and STM. (a) Height distribution measured by AFM. (b) Lateral size statistics measured by AFM. (c) Height distribution measured by STM. (d) Lateral size statistics measured by STM. The results from AFM and STM show consistency for the size measurements of monolayer MoS_2 bubbles. The diameters determined by AFM are slightly larger compared to values by STM due to the tip effect.

room temperature, the non-zero tunneling current which exists at all bias voltages, and the strong hybridization between the Au and the MoS_2 [39, 152]. However, sharp rises can still be used to determine the band edges. In the negative tunneling current region, the VBM can be assigned *ca.* -1.3 V and in the positive tunneling current region, the CBM can be assigned *ca.* +0.7 V. The -1.3 V onset agrees with the maximum of the valance band at the K point and the +0.7 V onset fits well with the minimum of the conduction band at the K point in the Brillouin zone. Thus, the width of the band gap can be approximated as around 2.0 eV, close to the calculated value for freestanding single-layer MoS_2 [7, 17, 153]. We have also observed that the dI/dV of the bubbles follows the same trend compared to the single-layer flat area (Figure 3.7). This data serves as complementary proof, suggesting that the protrusions in both the STM and AFM topographic images arise from protrusions in the MoS_2 instead of from any local tape residues or environmental contaminants.

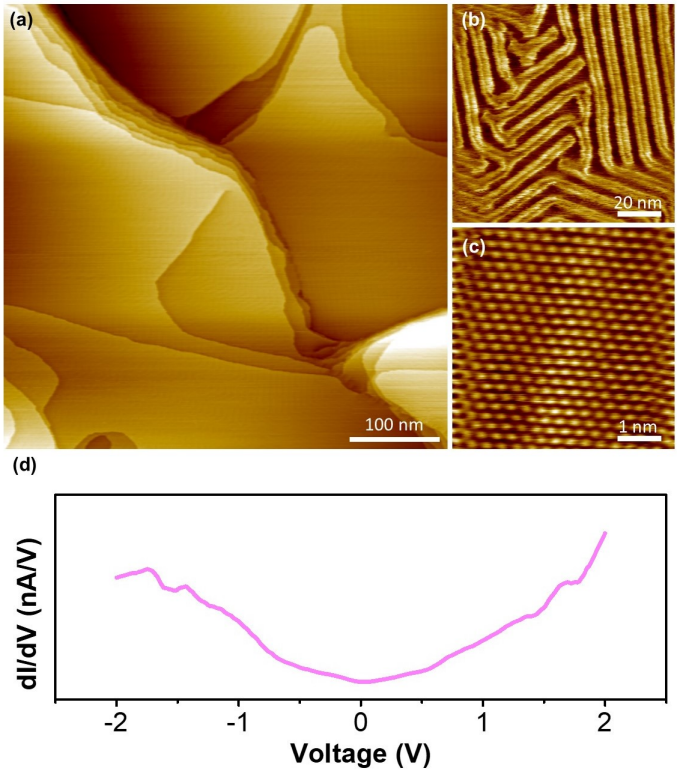

Figure 3.6: STM/STS characterization of Au(111) substrates. (a) Large-scale STM image (V_{bias} = +100 mV, I_t = 0.5 nA) showing the cleanliness of Au substrates. (b) Small-scale STM image (V_{bias} = -1 V, I_t = 1 nA) of Au(111) herringbone reconstruction. (c) Atomic-resolution STM image of Au(111) surfaces (V_{bias} = +100 mV, I_t = 0.5 nA). (d)STS spectrum of Au(111). The set point used to stabilize the tunneling gap is +500 mV and 0.5 nA. The plots are numerically calculated derivatives (dI/dV) of the averaged I-V curves.

In addition to the regular 1H moiré with periodicity *ca.* 3.15 nm, a different moiré with a dissimilar periodicity has also been observed. Figure 3.8a illustrates a 100 nm $\times$100 nm STM image showing both moiré patterns with two distinct periodicities. A clear domain boundary can be identified between the two moiré regions and the new moiré exhibits a smaller periodicity. Similar contrast along the boundary suggests that there is no significant height variation across the domain boundary (single terrace). The rotational angle between the two moiré patterns is measured *ac.* 21°. Figure 3.8b demonstrates a high-resolution STM image for both domains. Interestingly, the interfaces here appear to be crystallographically coherent on Au(111) substrates. In addition, while one might expect a sharp transition interface due to polar discontinuities, that has not been

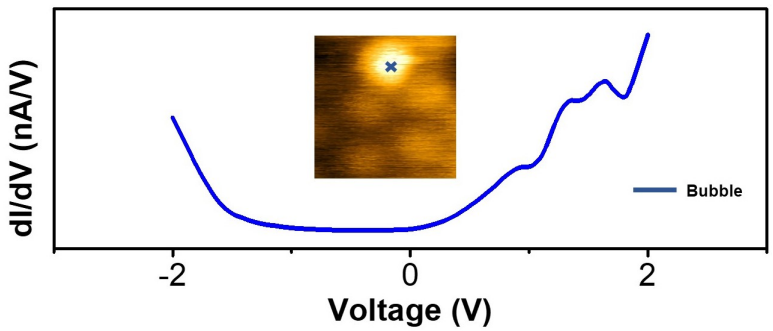

Figure 3.7: STS spectrum on the single-layer MoS_2 bubble, taken on the cross of the inserted STM image. The set point used to stabilize the tunneling gap is +500 mV and 0.5 nA. The plot is numerically calculated derivatives (dI/dV) of 100 averaged I-V curves.

observed, since the charge carriers from the Au(111) substrate can significantly screen these, which we have confirmed computationally (see Figure 3.9). To evaluate the partial charge distribution at the interfaces, we calculated the local charges using the self-consistent charge equilibration methods [154]. (based on local atomic neighborhood). The system consists of neighboring flakes of 1H and 1T MoS_2 on a metallic substrate with an Au(111) lattice, or the isolated system in vacuum. The system was energy minimized according to the force field used for the molecular dynamics simulations [155] followed by a final charge equilibration. The graphics show atoms in the MoS_2 flakes only with colors based on the calculated partial charges for the 1H and 1T MoS_2 system (on the left) on Au(111) and (on the right) in vacuum. Here, while a discontinuity appears in vacuum, this is clearly seen to be significantly screened on Au(111). A line profile for the "new" moiré has been measured in Figure 3.8d. The moiré periodicity is *ca.* 2.31 nm and the height corrugation is *ca.* 0.4 Å, which are smaller compared to the 1H moiré, accordingly. A careful atomic distance measurement has been employed in the STM current image (Figure 3.8c) since the current image provides a higher contrast. Line profiles (blue and red line profiles in Figure 3.8d) along the identical atomic row have been taken for 20 unit cells on both regions. The red line always exhibits a larger distance compared to the black line with the same lattice numbers. The lattice constants for these two regions have been measured as *ca.* 3.152 Å for the regular moiré and *ca.* 3.252 Å for the "new" moiré. The lattice constant for the regular moiré

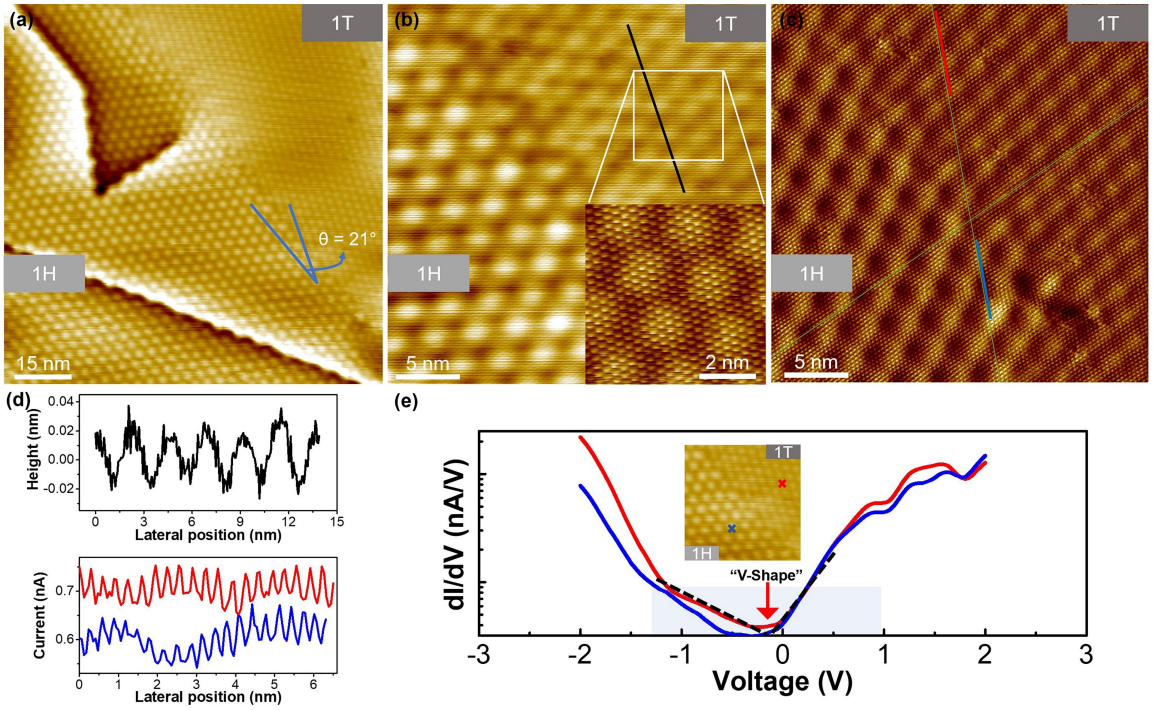

Figure 3.8: STM/STS characterization of the coherent heterostructures of MoS_2 monolayers. (a) Large-scale STM image (V_{bias} = +500 mV, I_t = 0.5 nA) of single-layer MoS_2 with two different moiré patterns. (b) High resolution STM topography image (V_{bias} = +100 mV, I_t = 0.5 nA) of single-layer MoS_2 showing the atomistic structures and the moiré periodicities. The insert shows a magnification topography image of the selected area (V_{bias} = +100 mV, I_t = 0.5 nA). (c) Corresponding high resolution STM current image (V_{bias} = +100 mV, I_t = 0.5 nA) of single-layer MoS_2 on Au(111). (d) Line profile (black) showing the periodicity and the corrugation of the 1T-MoS_2 moiré pattern in (b) and line profiles (blue and red) presenting the atomic distances for two different phases in (c). (e) STS spectra taken on two different spots as indicated in the inserted STM image. The set point used to stabilize the tunneling gap is +500 mV and 0.5 nA. The plots are numerically calculated derivatives (dI/dV) of 100 averaged I-V curves for each location. To enhance the analysis precision, logarithmically scaled spectra are employed.

region shows consistency with the lattice constant of the 1H phase, while the lattice constant for the "new" moiré region, matches the value of the 1T phase [156, 157]. We choose not to include the fast Fourier transform (FFT) of these two regions, as the real space measurement is more accurate as the moiré periodicity and lattice constant measurements of both phases in real space are averages of multiple unit cells, while the analysis by FFT is only a measurement of a few points in the reciprocal space. Such a result reveals the co-existence of the two polymorphs with matched lattices inside the monolayer MoS_2. Note that to the best of our knowledge, this is the

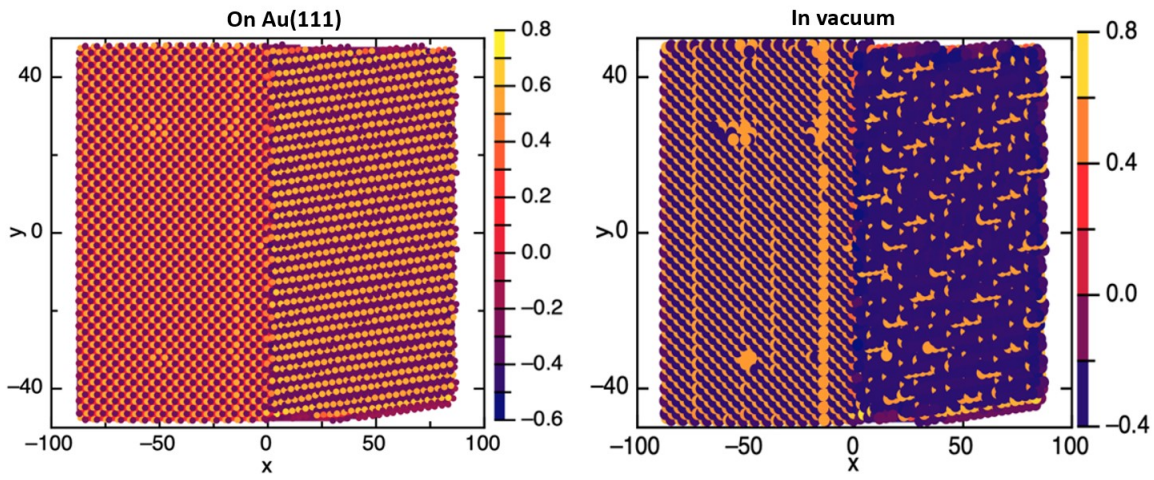

Figure 3.9: Partial charge distributions in the 1H and 1T phases of MoS_2, on Au (left) and in vacuum (right).

first coherent heterostructure of single-layer MoS_2 reported that has been prepared by mechanical exfoliation. While it is possible that a low-angle grain boundary in MoS_2 sheet could result in different moiré structures, we didnt observe any change in the lattice orientation, along two typical horizontally and vertically straight lines across both 1H and 1T regions in Figure 3.8c, proving this is not due to a slight change in lattice orientation. Conductance spectra (dI/dV) have also been taken on these different regions to examine the electronic structures of both phases. Figure 3.8e elucidates the STS spectra taken on two different spots, as indicated in the inserted STM image. The blue curve represents dI/dV on the 1H-MoS_2 area and the red curve corresponds to dI/dV on the 1T-MoS_2 area. In contrast to the semiconducting 1H-MoS_2 spectrum, a gapless V-shaped curve has been observed for the 1T-MoS_2. These results further confirm the co-existence of the semiconducting 1H phase and the metallic 1T phase within the mechanically exfoliated MoS_2 monolayers on Au substrates, consistent with the STM and the optical characterization described above. The formation and transition of the 1T-MoS_2 phase can be explained by charge transfer and the built-in strain from the Au substrate [124, 158]. Generally, the phase transition from the 1H phase to the 1T phase involves the change in position of an S atom from one pyramidal site in the lattice to the other. Charge transfer from the Au not only lowers the transition barrier, but also

stabilizes the 1T phase [19]. Particularly, most of the charge transferred from the Au substrates accumulates on the S atoms. These extra electrons weaken the Mo-S bonds and destabilize the 1H structure. At the same time, another small amount of charge is transferred into the nonbonding d-orbitals of Mo, which induces the nonbonding d-orbitals to spilt into two d-orbitals: $d_{yz,xz,xy}$ and d_{z^2,x^2-y^2}. The $d_{yz,xz,xy}$ is partially filled and the d_{z^2,x^2-y^2} is empty, which increases the metallic feature of MoS_2, and further stabilizes the 1T phase. In concert with the charge transfer effects, due to the heating process during sample preparation, the thermal coefficient of expansion mismatch introduces extra tensile strain into the MoS_2 monolayer. The strong coupling between the MoS_2 and the Au substrate, enables the accumulation of strain and promotes the phase transition of the MoS_2 on certain areas inside the monolayer [147, 159, 160]. The ability to control this in a precise way would enable new device designs in single layer MoS_2, and we will soon be exploring the effects of strain on this formation process.

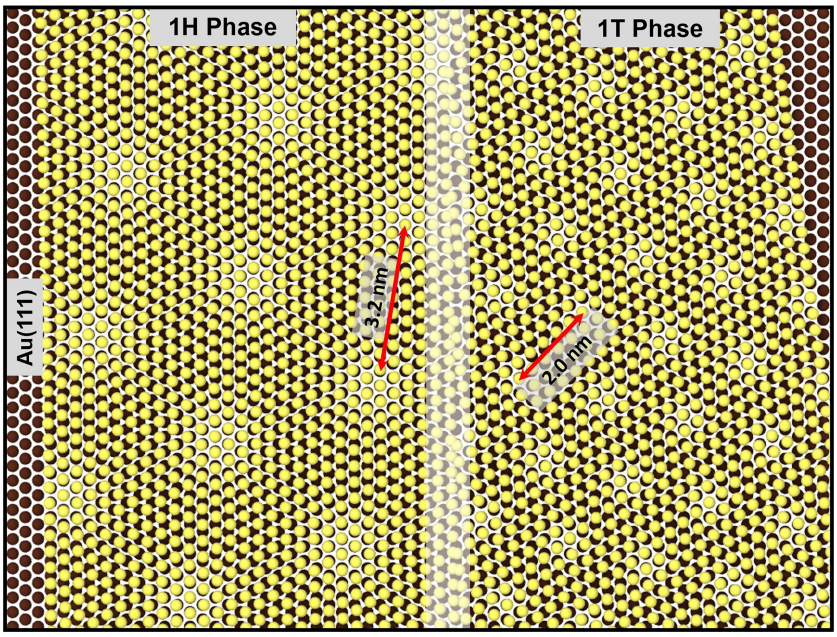

Figure 3.10: Simulated moiré patterns for MoS_2 on Au(111), with Au atoms shown in red and sulfur atoms from the lower layer of the MoS_2 shown in yellow. The left side of the MoS_2 flake is the 1H form, while the right side is the 1T form.

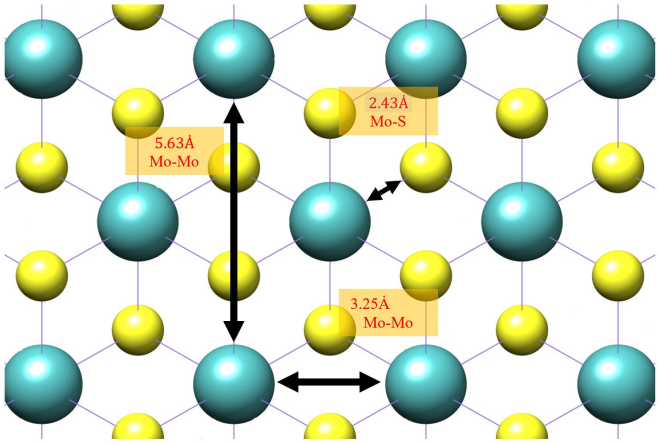

Figure 3.11: Top view of 1T MoS_2 showing the octahedral coordination and atomic distances. (aqua sphere: molybdenum atom, yellow sphere: sulfur atom).

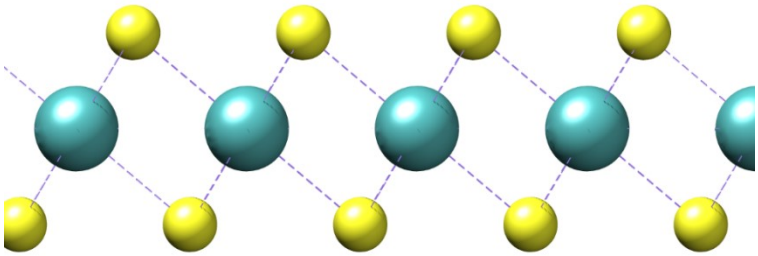

Figure 3.12: Side view of 1T MoS_2. (aqua sphere: molybdenum atom, yellow sphere: sulfur atom).

Figure 3.10 illustrates a model of the coherent heterostructures containing both 1H and 1T phases. The left side of the figure is the 1H form of MoS_2 on Au(111), while the right side of the figure is the 1T phase. The entire MoS_2 flake is rotated by 1° from the perfectly commensurate state to slightly adjust the periodicities of both moiré structures. The domain boundary (shown as the grey area) is not relevant, as the two areas were constructed separately. From Figure 3.10

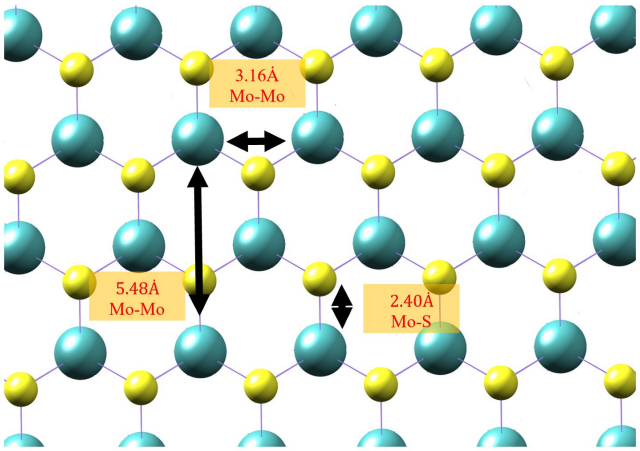

Figure 3.13: Top view of 1H MoS_2 showing the trigonal prismatic coordination and atomic distances. (aqua sphere: molybdenum atom, yellow sphere: sulfur atom).

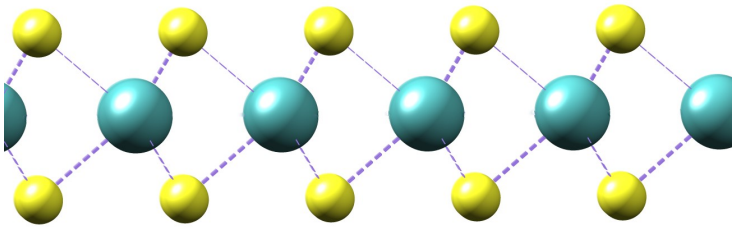

Figure 3.14: Side view of 1H MoS_2 (aqua sphere: molybdenum atom, yellow sphere: sulfur atom).

we can clearly see the stacking of the MoS_2 sheet on the Au(111) surface generates a modulated superlattice which reflects the similar structure and periodicity observed in the STM above. In addition, the rotational angle between the two moiré patterns is measured *ca.* 22.7°, closely matching our experimental STM data in Figure 3.8a. Details of the model can be found in the Figure 3.11 to Figure 3.14.

3.2.4 Bubble Engineering in Monolayer MoS_2 on Au(111)

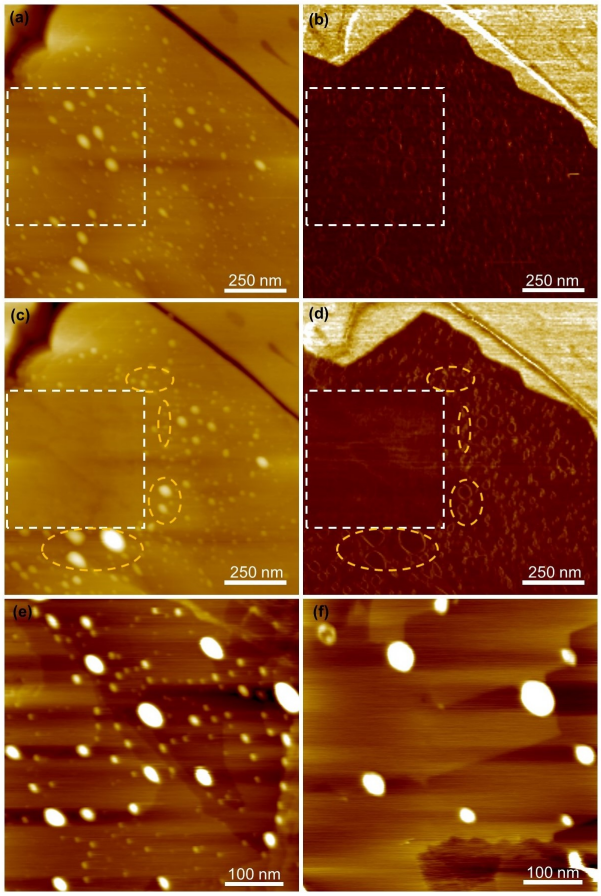

Figure 3.15: AFM characterization of single-layer MoS_2 bubbles on Au(111) surfaces. (a) AFM topography image (load: 1nN) showing monolayer MoS_2 on Au(111) before scanning with a large load (50 nN). (b) Corresponding AFM friction image (load: 1nN) showing monolayer MoS_2 on Au(111) before scanning with a large load (50 nN). (c) AFM topography image (same location: load: 1nN) containing the area scanned with a large load (50 nN). (d) Corresponding AFM friction image (same location: load: 1 nN) containing the area scanned with a large load (50 nN). The inserted squares are the areas scanned with a large load (50 nN). (e) AFM topography image (load: 1 nN) showing monolayer MoS_2 on Au(111) before annealing. (f) AFM topography image (load: 1 nN) showing monolayer MoS_2 on Au(111) after annealing in vacuum at 500 °C for 30 minutes.

In addition to the coherent heterostructures observed in the mechanically exfoliated MoS_2 monolayers, ripples and bubbles are always formed due to the soft nature of MoS_2 membranes. The AFM images in Figure 3.15 demonstrate that the MoS_2 monolayers are not flat on the Au

substrates. Bubbles are formed throughout the entire surface during exfoliation and film transfer. While the exact content of the bubbles is still unclear, recent work in the literature suggests that they contain predominately water, as their areal density and size have been shown to be highly dependent on temperature and humidity [161]. The trapped water inside the bubbles is mobile and can be engineered by the AFM tip using large loads. Figure 3.15a and Figure 3.15b illustrate the AFM topography and friction images before mechanically manipulating the bubbles. After scanning with a 50 nN load in the square area, AFM images have been taken again (Figure 3.15c and Figure 3.15d). All bubbles inside this area have been "nano-ironed" out and the bubbles around the scanning area increased in size and density (marked with orange circles). The bubbles can also be manipulated by thermal annealing. Comparing Figure 3.15e and Figure 3.15f, small bubbles disappear after annealing at 500 °C in vacuum for about 30 minutes. In addition, large bubbles increase in size, indicating the coalescence of smaller bubbles into the large ones.

3.3 Conclusions

Here we have demonstrated a facile mechanical exfoliation technique to prepare MoS_2 monolayers. This technique does not exhibit any of the tape residues reported in other exfoliation methods, and allows for single-layer MoS_2 of millimeters in lateral dimension for be formed on Au substrates. STM measurement show two distinct moiré patterns appearing in the MoS_2 on Au(111) that arise from the 1H and 1 T phases with single coherent layers. The existence of the 1T phase has been confirmed by Raman, XPS, STM as well as STS. Although coherent heterostructures have been observed in chemically exfoliated single-layer MoS_2 by scanning transmission electron microscopy [162], we believe this is the first time that coherent single-layer MoS_2 heterostructures formed by exfoliation on a supported surface have been seen. The formation of these junction is likely due to a combination of charge transfer from the Au substrate and built-in tensile strain facilitating the spatial transition of the 1H to the 1T phase. This work provides important guidance to produce macroscale coherent heterostructures of MoS_2 monolayers, which represent unique candidates for future electronic devices and applications, and their designed fabrication through spatial control of strain will be the subject of future work from our lab. As in other cases of deposited 2D

materials on surfaces, we also observed the trapping of ambient adsorbates (most likely water) beneath the MoS_2 forming bubbles due to their displacement during deposition. AFM studies showed that these bubble structures could be manipulated by imaging under increasing applied load.

3.4 Methods

Mechanical Exfoliation Method Our method for the deposition of MoS_2 on Au is detailed in the main body of the text, and is illustrated in Figure 3.1. MoS_2 samples were purchased from SPI Supplies. Au(111) substrates were bought from Phasis, which were 200 nm thick films on mica after flame annealing treatment. The thermal release tape was acquired from Graphene Supermarket.

Optical Microscopy and Raman Microspectroscopy Optical images were taken using a Witec 300 RA confocal microscope with a Nikon objective (10×, 0.25 N.A.). All Raman measurements were taken using a Witec 300 RA with a Nikon objective (100×, 0.9 N.A.), an 1800 g/mm grating, and a 532 nm excitation source. Reported data were averages of 100 spectra with an integration time of 1 s. The laser power was kept below 1 mW for all measurements.

X-ray Photoelectron Spectroscopy XPS data was acquired with a Scientia Omicron ESCA+ X-ray photoelectron spectrometer equipped with a hemispherical electron energy analyzer and 128-channel micro-channel plate. The radiation source was Mg Kα (1253.6 eV) with a source power of 300 W (15 kV, 20 mA). The energy resolution is *ca.* 0.8 eV with a spot size of *ca.* 54 μm. Chamber pressure was maintained in the $\sim 10^{-10}$ mbar range. Survey scans were carried out at a passing energy of 100 eV with 1.0 eV steps and a dwell time of 0.1 s. Multiplexed high-resolution scans of Mo 3d and S 2p were taken at a passing energy of 20 eV with 0.05 eV steps and a dwell time of 0.1 s. The survey and high-resolution spectra were averaged with 3 and 50 scans, respectively. All peak positions were calibrated with respect to the Au $4f_{7/2}$ peak at 84.0 eV.

Atomic Force Microscopy Contact-mode AFM images were collected using an Agilent 5500 and analyzed with Scanning Probe Image Processor (SPIP) software (version 6.0.2, Image Metrology, Lyngby, Denmark). Scans were performed at 1 nN with a 10 nm silicon probe (spring constant

$\sim$0.2 N/m and resonant frequency $\sim$20 kHz) under dry nitrogen conditions (0.1% relative humidity).

Scanning Tunneling Microscopy and Scanning Tunneling Spectroscopy STM images were collected with a variable-temperature scanning tunneling microscope (VT-STM) (Scientia Omicron GmbH, Germany) system (with a base pressure $< 1 \times 10^{-10}$ mbar) using mechanically cut Pt/Ir (80/20) tips. Constant-current mode images were obtained in a tip biasing and sample grounding configuration, and analyzed with SPIP. Detailed bias voltages and tunneling currents were described in each STM image. One hundred I-V curves were collected and averaged for each spectrum, by sweeping the voltage bias from -2 V to 2 V. The set point used to stabilize the tunneling gap was +0.5 V and 500 pA. To avoid various tip effects, I-V spectra were discarded if the subsequent imaging showed tip changes after the spectra were collected. All the images and the I-V spectra were collected at room temperature.

Modeling of the Moiré Pattern Atomic coordinates for the unit cell of the 1T phase of MoS_2 were acquired from the crystallographic information file from Springer Materials. The structural relaxation was carried out with Density Functional Theory (DFT) calculations with the Quantum ESPRESSO package. The General Gradient Approximation was used to describe the exchange correlation functional with a Perdew-BurkeErnzerhof parametrization corrected by the semiempirical Grimme scheme (PBE-D). Quantum Espresso was used to perform structural relaxation to confirm that the structure was stable. The unit cell of 1T-MoS_2 was replicated to form a 4×4 hexagonal supercell to mimic the basal plane of MoS2. A 3×3 k-point Monkhorst-Pack grid was used with a kinetic energy cut-off of 40 Rydberg and Methfessel-Paxton smearing (0.01 Rydberg) to ease the optimization procedure. structure relaxation in Quantum Espresso resulted in insignificant deviation from the initial structure. The supercell was replicated to obtain larger sheets (48×48) of 1T phase MoS_2 that were overlayed on a gold substrate to create the Moiré patterns. No further relaxation was performed on the MoS_2/Au structure, and only the bottom (top) layer of sulfur (gold) atoms are shown to improve clarity.

4. ACCELERATED AGING OF MOS2 ON AU(111)

4.1 Introduction

MoS_2 has received considerable attention over the past decade due to its promising mechanical and electronic properties [1–3, 5–7]. Differing from graphenes atomically thin structure, MoS_2 consists of a transition metal Mo layer, sandwiched between two layers of sulfur atoms. Similar to graphene and other layered two-dimensional (2D) materials, MoS_2 can be easily cleaved from its bulk crystal due to the weak van der Waals forces between layers [43,44]. The resulting low friction advocates its use as a solid lubricant in space tribological applications [80, 81, 163]. However, the inevitable exposure to environments, such as water (H_2O), molecular oxygen (O_2), ozone (O_3), and atomic oxygen (AO) has been shown to modify the properties of MoS_2, and significantly affect its tribological performance [48, 164–167].

The accelerated aging of MoS_2 on SiO_2 has been extensively investigated under various conditions. Anisotropic etching was reported for MoS_2 when exposed to O_2 at 300-340 °C [49, 50]. However, when annealed in an O_2/Ar environment at 350 °C, a complete chemical transformation of MoS_2 to MoO_3 was observed by Dooyong Lee *et al.* [51]. A systematic study by Curry and Jung revealed that the MoS_2 oxidation depended significantly on the microstructure [48] and crystallinity [168]. In addition to these aging studies at elevated temperature in oxygen rich environments, the evolution of MoS_2 was also investigated *via* oxygen plasma treatment. Although the photoluminescent measurements of MoS_2 led to controversial interpretations of the degradation mechanisms, XPS experiments consistently showed the appearance of Mo^{6+} peaks, implying the prevalence of MoS_2 to MoO_3 conversion after oxygen plasma reactions [52,53,169]. Additionally, by tuning the oxygen plasma energy and exposure time, the oxygen species were able to physically adsorb on MoS_2, preferentially oxidize the out-facing sulfur layer (forming S-O bonds) or the topmost layer of MoS_2 flakes (forming MoO_3) [55, 170]. Another commonly used method to examine the oxidation of MoS_2 was UV/ozone treatment. Similar results were also reported with

this approach, with the formation of both S-O and O-Mo bonds in MoS_2 [56, 171–173].

Solid lubricant coatings made from MoS_2 necessarily include interfaces attached to metal substrates, which could strongly modify its chemical and tribological properties [174, 175]. Although the accelerated aging of MoS_2 has been extensively investigated on SiO_2 in a wide range of conditions, studies on metal substrates are still lacking. Here, we explore MoS_2/Au(111) as a model system to study the aging of MoS_2 on metal surfaces *via* UV/ozone exposure. The reactive environment, consisting of gas species including O_2, O_3, and AO created under this condition was similar to those in the extraterrestrial environments, especially in the low earth orbit (LEO) [164, 176]. We found that, the chemical interaction of MoS_2 with these oxidizing environments depended strongly on the number of layers of MoS_2. Optical microscopy, AFM, XPS, and Raman spectroscopy collectively elucidated the evolution of MoS_2 on Au(111) under UV/ozone condition. Our work provides new insights of the accelerated aging of two-dimensional materials and the impact of substrate electronic interactions, which offers a critical guidance for rational design of the next-generation tribological systems.

4.2 Experimental Method

Mechanical Exfoliation Method The MoS_2 on Au(111) samples were fabricated by a mechanical exfoliation method which has been described in Chapter 3. This was a redesigned procedure that eliminated tape residues typically seen in most scotch-tape methods. MoS_2 samples were purchased from SPI Supplies (West Chester, PA, USA). Au(111) substrates were acquired from Phasis (Geneva Switzerland), which were 200 nm thick films on mica after flame annealing. The thermal release tapes were acquired from Graphene Supermarket (Ronkonkoma, NY, USA).

UV-Ozone Treatment To investigate the accelerated aging of MoS_2, MoS_2/Au(111) samples were exposed to UV/Ozone (Novascan PSD-UV, UV wavelength at 185 nm and 254 nm, average intensity 28-32 mW/cm^2 at 253.7 nm) from 0 to 60 min at a fixed lamp-sample distance *ca.* 1 cm.

Optical Microscopy and Raman Microspectroscopy Optical images were acquired using a Witec 300 RA confocal microscope with a Nikon objective (100×, 0.9 N.A.).All Raman mea-

surements were acquired using a Witec 300 RA with a Nikon objective (20×, 0.9 N.A.), an 1800 g/mm grating, and a 532 nm excitation source. Reported data were averages of 6 spectra with an integration time of 10 s each. The laser power was kept at about 4.6 mW for all measurements. All Raman spectra were processed with WITec Suite 4.0 software (Project FOUR).

X-ray Photoelectron Spectroscopy X-ray photoelectron spectra were collected with a Scientia Omicron ESCA+ X-ray photoelectron spectrometer equipped with a hemispherical electron energy analyzer and 128-channel micro-channel plate. The X-ray source was Mg Kα (1253.6 eV) with a source power of 150 W (15 kV, 10 mA). The energy resolution was *ca.* 0.8 eV with a spot size of *ca.* 54 μm in diameter. The pressure in the characterization chamber was maintained in the 10^{-10} mbar range. Survey scans were performed at a passing energy of 100 eV with 1.0 eV steps and a dwell time of 0.1 s. Multiplexed high-resolution scans of Mo 3d and S 2p were taken at a passing energy of 20 eV with 0.05 eV steps and a dwell time of 0.1 s. The survey and high-resolution spectra were averaged with 3 and 10 scans, respectively. All the peak positions were calibrated with respect to the Au $4f_{7/2}$ peak at 84.0 eV. Casa (version 2.3.22) software was employed for the XPS data analysis.

Atomic Force Microscopy Contact mode AFM (Agilent 5500) measurements were carried out with silicon tips (Mikromasch CSC37) in a dry nitrogen environment (relative humidity < 0.1% and at room temperature). The normal spring constants were *ca.* 0.2 N/m and the tip radii were *ca.* 10-20 nm. Scanning Probe Image Processor (SPIP, version 6.0.2, Image Metrology, Lyngby, Denmark) software was used for AFM data analysis.

4.3 Results and Discussion

4.3.1 Optical Characterization of the Accelerated Aging of MoS_2 on Au(111)

Similar to graphene on fixed thicknesses of silica [177], optical images of MoS_2 on Au(111) can be obtained that, due to refractive index differences, allow for the number of layers to be visually distinguished. Figure 4.1 presents the optical characterization of the structural evolution of MoS_2 on Au(111) due to UV/ozone exposure as a function of time. MoS_2 flakes are labeled

as SLM for single layer MoS_2, BLM for bilayer MoS_2, TLM for trilayer MoS_2, and Bulk for bulk MoS_2. Figure 4.1a shows the reference, as-exfoliated MoS_2 nanosheets before exposing to UV/ozone (the layer thickness was confirmed by AFM, see Figure 4.2). SLM can be identified as the areas with a faint color contrast. As the exposure time increased from 0 min to 30 min (Figure 4.1a to Figure 4.1f), the SLM films progressively faded. Intragranular/lamellar cracks and breaks gradually appeared and grew inside the films, while BLM and TLM remained relatively intact, indicating SLM might be more susceptible to UV/ozone induced oxidative degradation as compared to BLM or TLM.

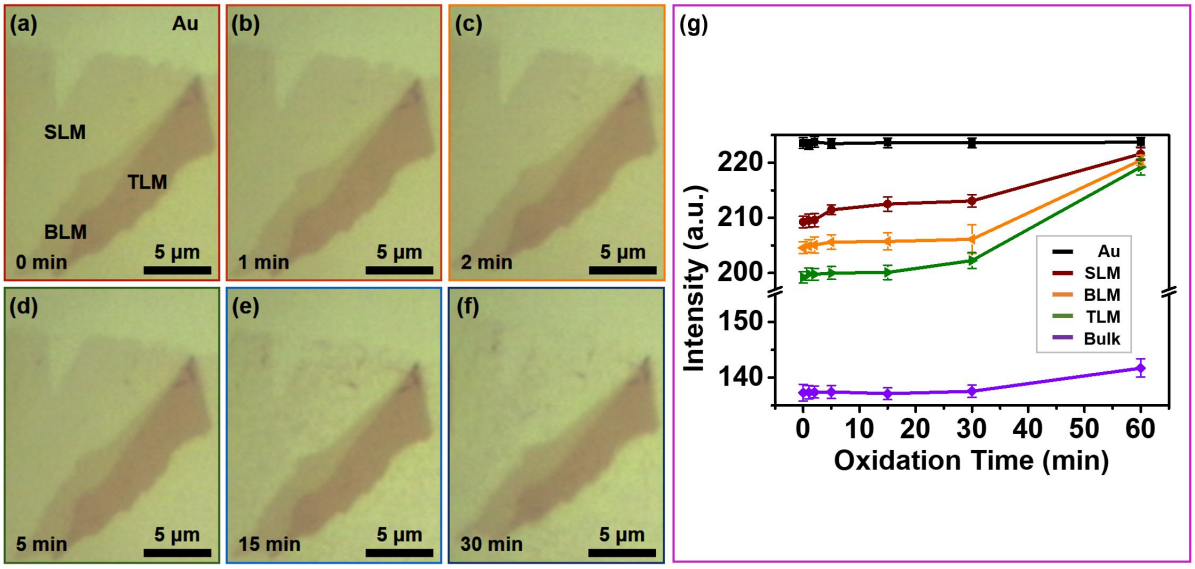

Figure 4.1: Optical characterization of MoS_2/Au(111) before and after UV/ozone treatment. (a) Initial as-exfoliated MoS_2 nanosheets on Au(111) and (b)-(f) MoS_2/Au(111) exposed to UV/ozone for 1, 2, 5, 15, 30 min, respectively. (g) Grey intensity analysis of MoS_2 as a function of oxidation time. The grey scale intensities were taken from fixed areas of 1.85×1.85 μm^2 in each image.

To quantitatively analyze the optical evolution of MoS_2 nanosheets, the grey intensity of Au, SLM, BLM, TLM, and Bulk were measured as a function of oxidation time (Figure 4.1g). The grey-scale intensities were taken from fixed areas of 1.85×1.85 μm^2 in each image. Bare Au had the highest intensity (used as a reference), followed by SLM, BLM, TLM, and bulk MoS_2 (the

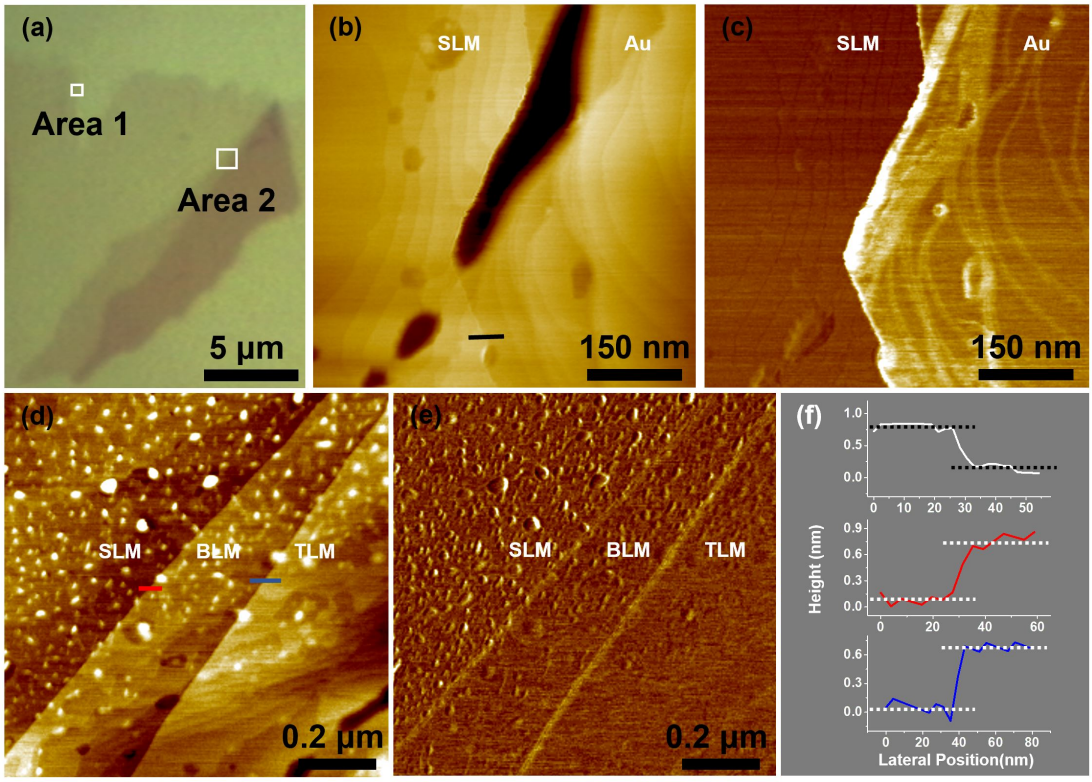

Figure 4.2: Layer thickness measurement of as-exfoliated MoS_2 nanosheets by AFM. (a) Optical photograph of MoS_2 nanosheets on Au(111). (b) AFM topography image showing SLM and Au substrate in Area 1. (c) Corresponding AFM friction image in (b). (d) AFM topography image showing SLM, BLM, and TLM in Area 2. (e) Corresponding AFM friction image in (d). (f) Height profiles taken across the edges along the directions marked by black, red, and blue lines in (b) and (d), confirming the layer thickness of SLM, BLM, and TLM.

bulk was much lower than the others). As the time increased from 0 min to 60 min, the intensity remained the same for Au, and increased by a small amount for bulk MoS_2, while the intensities for SLM, BLM, and TLM all increased substantially and reached their plateau values at 60 min, which were close but marginally smaller than the bare Au. The optical image of the same area at 60 min (see Figure 4.3) shows that most of the MoS_2 nanosheets were optically seemed to be "etched away". Nevertheless, whether the MoS_2 nanosheets were physically etched away by UV/ozone as well, was not determined, since this could simply be a refractive index effect.

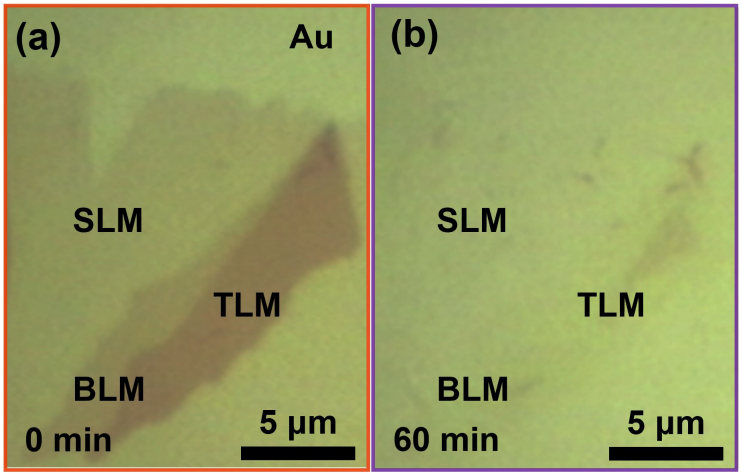

Figure 4.3: Optical images of as-exfoliated MoS_2 nanosheets (a) and MoS_2 nanosheets after 60 min of UV/ozone exposure in the same location.

4.3.2 Structural and Chemical Transformation of MoS_2 under Short Exposure Times

To further evaluate the structural and chemical evolution of MoS_2 on Au(111), AFM was employed to explore the corresponding structural change before and after 1 min of UV/ozone exposure. Figure 4.4a illustrates the topography image of both SLM and MLM on Au(111) before UV/ozone exposure (see Figure 4.5 for layer thickness determination). The elevated "bubbles", which appear to be formed by trapped ambient adsorbates during the film deposition, have been recently suggested to be predominately trapped water [161]. The height of the bubbles ranges from 0.5 nm to 10 nm, and the width of the bubbles ranges from 10 nm to 100 nm based on AFM measurements (tip radius of curvature from 10 to 20 nm). Figure 4.4b shows the corresponding friction image of both SLM and MLM on Au(111). Overall, similar friction contrast was observed for SLM and MLM, while the Au substrate showed a much higher friction. However, from the friction cursor profile (inserted green curve along the white scan line), the friction on SLM appears slightly higher than on MLM, consistent with the reported pattern of increasing friction with decreasing thickness for atomically thin sheets (graphene, MoS_2, $NbSe_2$, and h-BN) [3]. Moreover, MoS_2 bubbles possess isolated regions of slightly higher friction and this is attributed to the puckering effect, where adhesion to the sliding AFM probe induces out-of-bubble deformation, leading

to increased contact area and friction. After 1 min of UV/ozone exposure, there was no significant transformation observed in the topography image (Figure 4.4c), but notable difference observed in the friction image (Figure 4.4d). Specifically, the friction on SLM (Au-supported regions) increased considerably, while the friction on MLM only changed by a small amount relative to Au (also shown in the inserted green friction-cursor trace). Interestingly, in contrast to the friction increase for Au-supported SLM, the friction of the suspended SLM (bubbles) remained relatively intact, suggesting the local substrate interactions might play an important role.

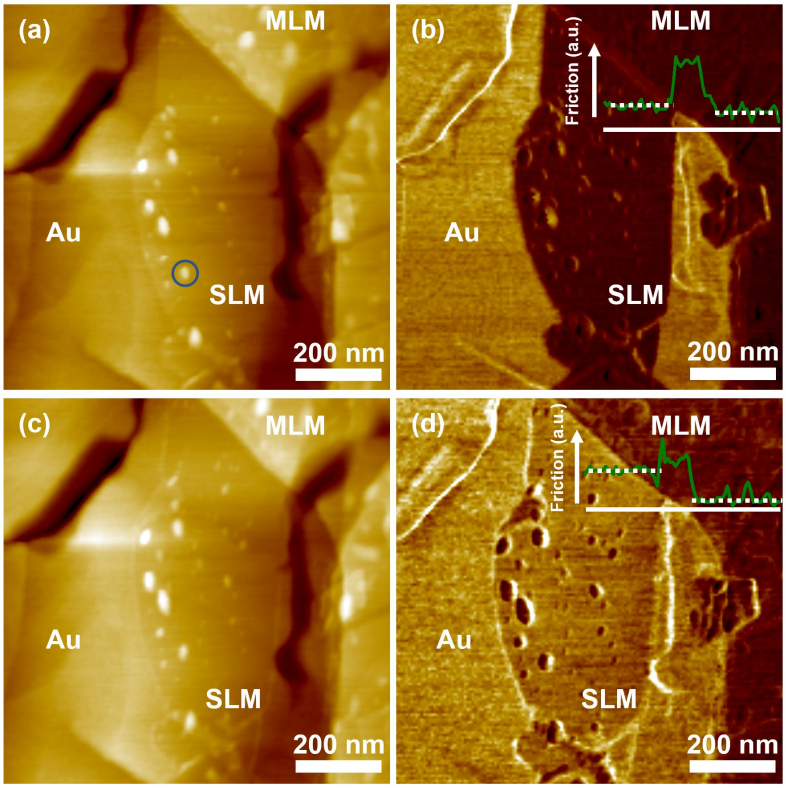

Figure 4.4: AFM characterization of MoS_2 nanosheets on Au(111) before and after 1 min of UV/ozone exposure. (a) AFM topography image showing SLM and multi-layer MoS_2 (labeled as MLM) before UV/ozone exposure. Both areas are free from tape residues. The bright protrusions, *e.g.*, in the blue circled location, are bubbles formed during the transfer. (b) Corresponding AFM friction image in the same area before UV/ozone exposure. (c) AFM topography image in the same area after 1 min exposure. (d) Corresponding AFM friction image in the same area after 1 min exposure. The green lines in Figure 2(b) and 2(d) are profiles of friction force along the white scan lines.

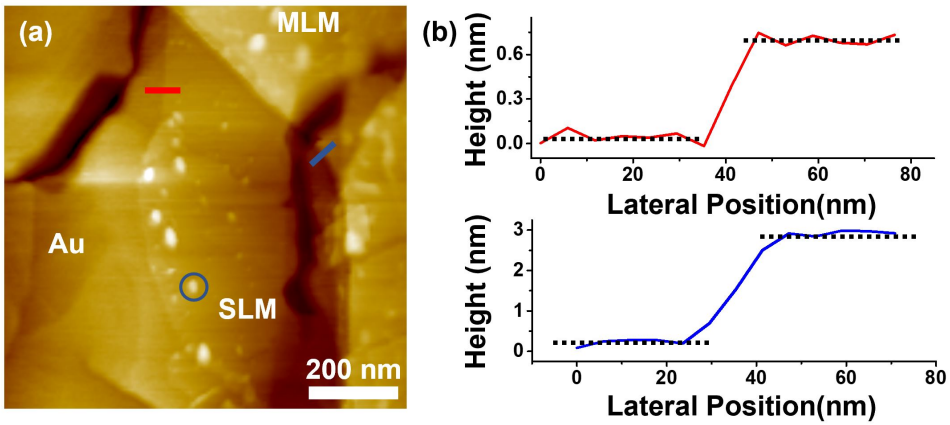

Figure 4.5: Layer thickness measurement of MoS_2 nanosheets by AFM. (a) AFM topography image showing SLM, MLM, and Au substrate. (b) Height profiles taken across the edges along the directions marked by red and blue lines in (a), confirming the layer thickness of SLM and MLM.

We can understand the substantial increase in friction with Au-supported SLM when considering the underlying mechanisms influencing the associated change in both surface chemistry and tip-sample interactions. First, considering the surface chemistry, it has been reported that both UV/ozone and O_2-plasma (at low power *e.g.* 15 mW/m^2 and short exposure time on the order of, *e.g.* 1 min) have been shown to alter the MoS_2 surface through the formation of weak S-O bonds without disrupting the Mo-S bonds [170, 172]. Additionally, DFT studies pointed out that the formation of S-O bonds is energetically favorable and can occur without Mo-S bond breaking [56, 178]. Gold has also been well-recognized and widely-utilized as a catalytic promotor to enhance the reactivity of MoS_2 [179–181]. Therefore, we propose (and later confirm through XPS) that, due to the enhanced reactivity for Au-supported SLM as compared to the elevated SLM (bubbles) or MLM (where the top layer of MoS_2 is decoupled from the substrate Au), a much larger density of top-layer S-O bonds are formed on Au-supported SLM regions. Such a change in the surface chemistry would greatly increase the hydrophilicity on the Au-supported SLM regions and thus, increase the adhesion and friction response with the AFM probes (silicon tips in our case with thin oxidized layers on tip surface) as compared to the elevated SLM or MLM regions.

Figure 4.6 illustrates the XPS results elucidating the chemical transformation of MoS_2 nanosheets

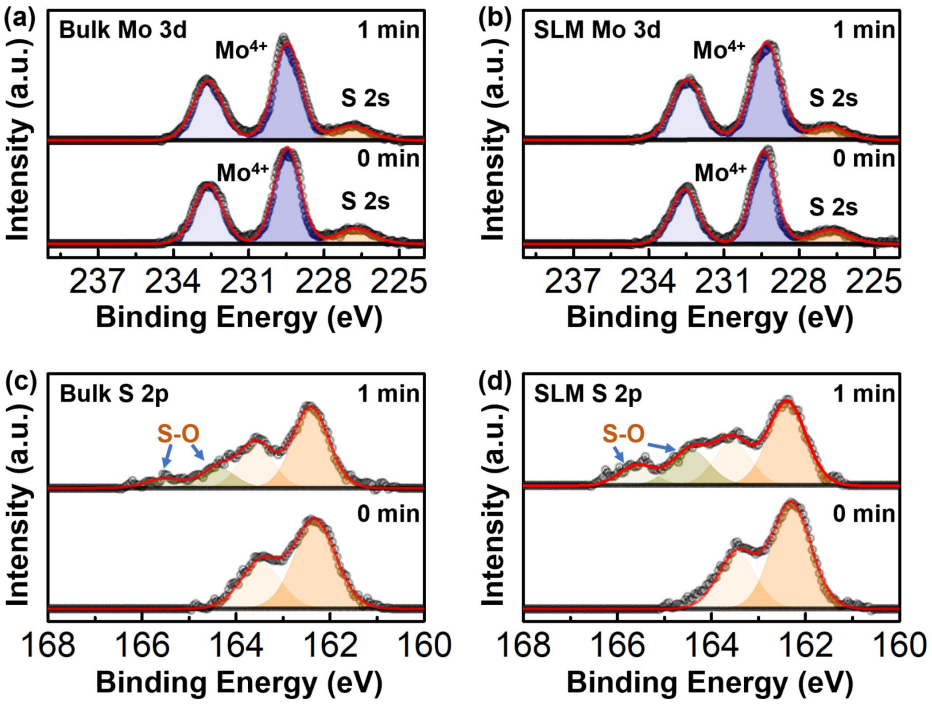

Figure 4.6: XPS characterization of MoS_2 on Au(111) before and after 1 min of UV/ozone exposure. (a) Bulk Mo 3d core level XPS spectra before and after 1 min of UV/ozone exposure. (b) SLM Mo 3d core level XPS spectra before and after 1 min of UV/ozone exposure. (c) Bulk S 2p core level XPS spectra before and after 1 min of UV/ozone exposure. (d) SLM S 2p core level XPS spectra before and after 1 min of UV/ozone exposure.

before and after 1 min of UV/ozone exposure. Because of the size of the X-ray beam (*ca.* 54 μm), we have only measured the XPS signals on SLM and bulk MoS_2 (located using an optical lens in the XPS). Regardless of the MoS_2 thickness (either bulk MoS_2 or SLM), 1 min UV/ozone exposure resulted in a negligible difference in the Mo (Mo $3d_{5/2}$ and Mo $3d_{3/2}$) states. The signals at 229.5 eV, 232.6 eV, and 226.8 eV can be identified as Mo($3d_{5/2}$), Mo($3d_{3/2}$), and S(2s), respectively. Similarly, the signals at 162.4 eV and 163.6 eV can be assigned as S($2p_{3/2}$) and S($2p_{1/2}$) from MoS_2 nanosheets. Although no Mo-O peaks were detected, an additional S 2p doublet was detected at 164.4 eV and 165.6 eV, corresponding to the chemical adsorption of oxygen atoms and the following formation of S-O bonds. To quantify the S/Mo intensity ratios, the sensitivity-corrected intensities were analyzed with the relative sensitivity factors (RSF) of 0.570 and 2.867 for S 2p and Mo 3d, respectively [182]:

$$\frac{\mathrm{S}}{\mathrm{Mo}} = \frac{\mathrm{I}_{\mathrm{S}\ 2p}}{\mathrm{RSF}_{\mathrm{S}\ 2p}} \Big/ \frac{\mathrm{I}_{\mathrm{Mo}\ 3d}}{\mathrm{RSF}_{\mathrm{Mo}\ 3d}} \tag{4.1}$$

Before UV/ozone exposure, the calculated S/Mo intensity ratios for SLM and bulk MoS_2 were 1.95 and 1.94, which are close to the stoichiometric value of MoS_2. After 1 min of UV/ozone exposure, however, the calculated S/Mo intensity ratios for SLM and bulk MoS_2 decreased to 1.70 and 1.87, respectively. Such a result suggests a partial sulfur removal by oxygen occurs at this stage for both SLM and bulk MoS_2, where SLM experienced a higher sulfur loss percentage as compared to bulk MoS_2. Combined with the observation that the S-O bond signals on SLM showed higher intensities comparing to the bulk, we can further conclude that, indeed, an enhanced reactivity for SLM as compared to bulk MoS_2.

4.3.3 Structural and Chemical Transformation of MoS_2 under Extended Exposure Times

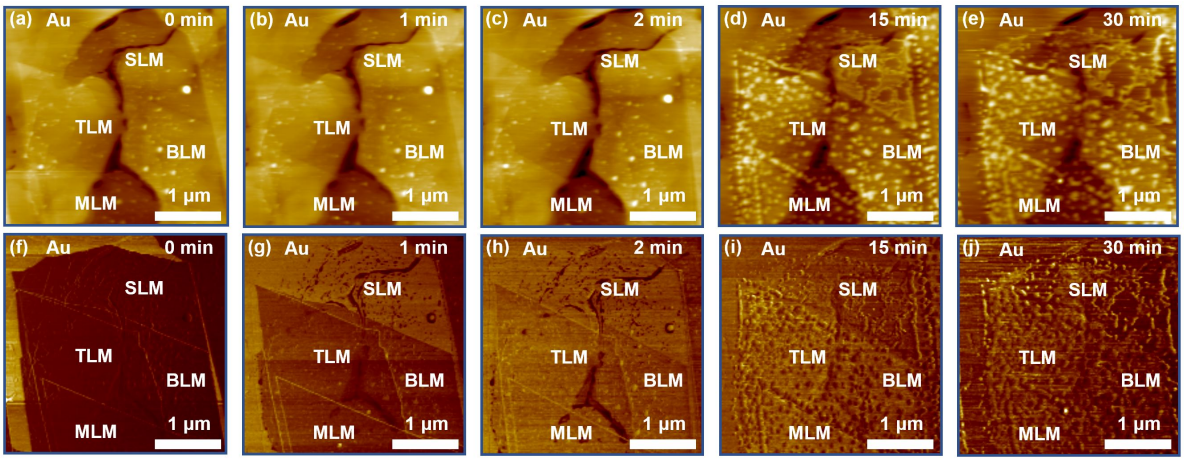

Figure 4.7: AFM characterization of MoS_2/Au(111) before and after UV/ozone treatment. (a) AFM topography image of as-exfoliated MoS_2 nanosheets and (b)-(e) AFM topography images of MoS_2 exposed to UV/ozone for 1, 2, 15, and 30 min, respectively. (f) Corresponding AFM friction image of as-exfoliated MoS_2 nanosheets in (a) and (g)-(j) corresponding AFM friction images of MoS_2 exposed to UV/ozone for 1, 2, 15, and 30 min in (b)-(e).

To systematically explore the oxidative changes in the MoS_2 nanosheets on Au(111), AFM (Figure 4.7) was implemented to monitor both the topographic and frictional changes after ex-

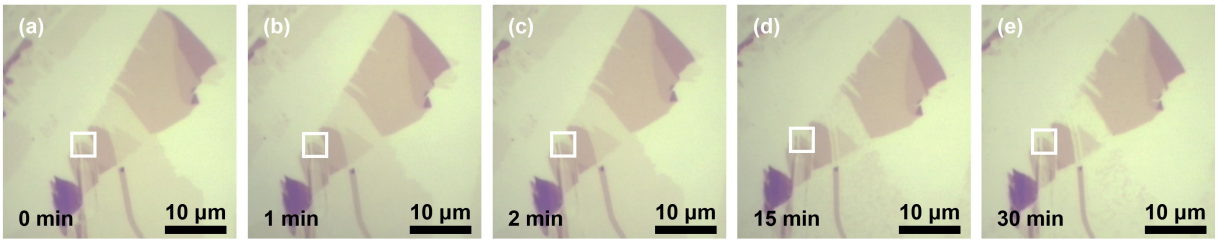

Figure 4.8: Optical photographs of MoS_2/Au(111) before and after UV/ozone treatment. (a) Optical image of as-exfoliated MoS_2 nanosheets and (b)-(e) Optical images of MoS_2 exposed to UV/ozone for 1, 2, 15, and 30 min, respectively. AFM characterization in Figure 4.4 was implemented in the square areas.

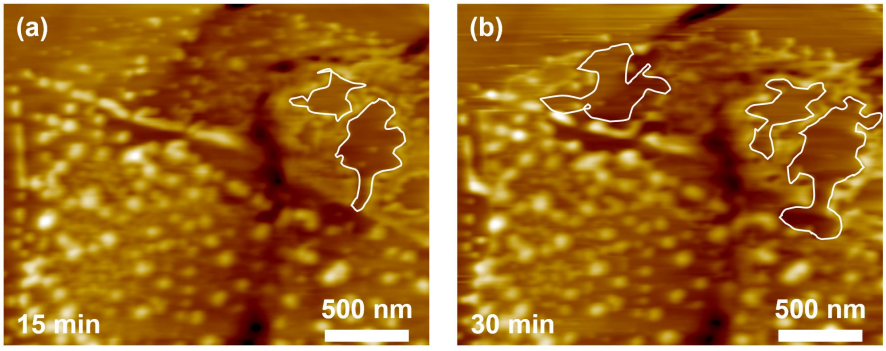

Figure 4.9: Zoomed-in AFM topography images of MoS_2 nanosheets in Figure 4.4 (d) and 4.4(e) after 15 and 30 min of UV/ozone exposure, showing the etched pits inside SLM regions increase their sizes and densities.

posure to UV/ozone for 0, 1, 2, 15, and 30 min in the same location (see corresponding optical images in Figure 4.8). After 1 min of UV/ozone exposure, similar results were observed that the friction response on SLM increased considerably more than BLM, TLM, and MLM. After 2 min of UV/ozone exposure, the friction increased on BLM, TLM, and MLM regions. No significant contrast difference was seen in these regions as compared to SLM, showing that the formation of S-O bonds is complete on various layer thickness (SLM, BLM, TLM, and MLM) at this stage. Despite the complicated friction transformation for difference MoS_2 layer thickness as a function of exposure time, no variation was detected in the topography images at these short exposure times (0, 1, and 2 min). In contrast, a considerable structural transformation on MoS_2 nanosheets was

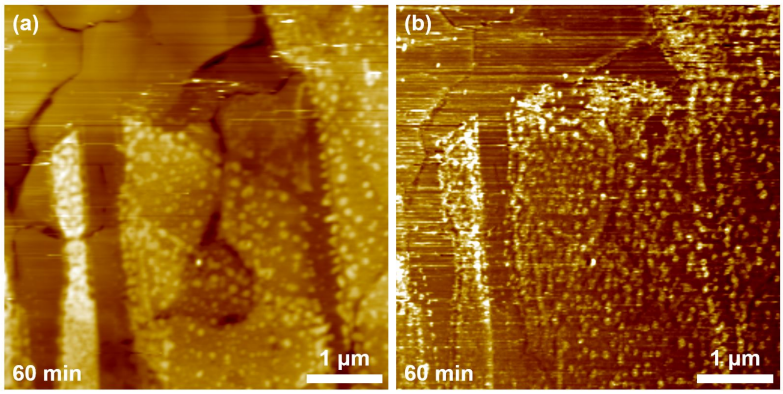

Figure 4.10: AFM characterization of MoS_2/Au(111) after 60 min of UV/ozone treatment. (a) AFM topography images of MoS_2 exposed to UV/ozone for 60 min. (b) Corresponding AFM friction image of MoS_2 exposed to UV/ozone for 60 min.

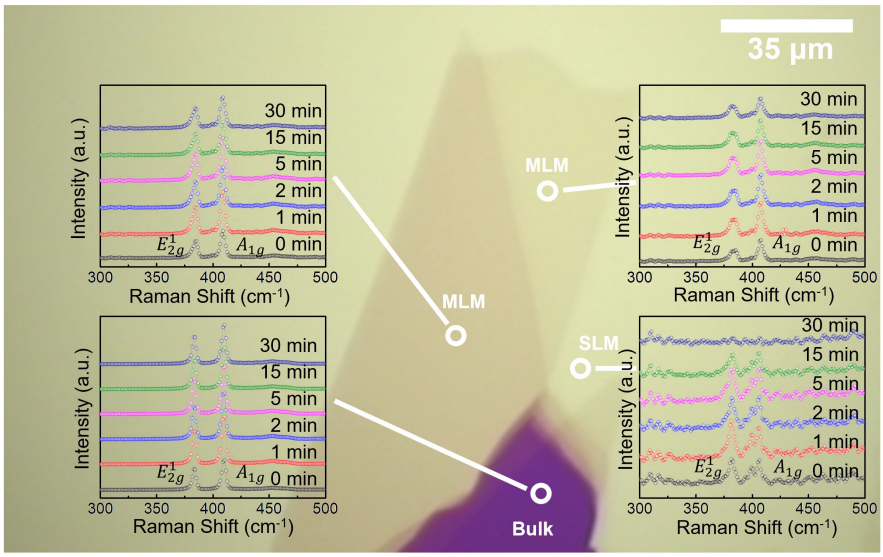

Figure 4.11: Raman spectra of SLM, MLM, and bulk MoS_2 before and after 1, 2, 5, 15, 30 min of UV/ozone exposure.

observed after 15 min of UV/ozone exposure. First, island-like structures were seen on all regions (SLM, BLM, TLM, and MLM), particularly on the edge sites, reflecting a nonuniform formation of MoO_3 on MoS_2 (as later confirmed by XPS). Second, in addition to the growth of MoO_3, SLM was further etched away, especially in the areas where fewer bubbles were observed. After 30 min of UV/ozone exposure, negligible changes occurred on BLM, TLM, and MLM. However, the etched

pits inside SLM regions increased their sizes and densities (close-up images in Figure 4.9) as compared to 15 min of UV/ozone exposure. Further extension of exposure time to 60 min (Figure 4.10) produced no significant morphological and frictional variations, reflecting that the oxidation of the MoS_2 nanosheets is complete at around 30 min. To further understand the structural degradation of MoS_2 nanosheets by UV/ozone exposure, Raman microspectroscopy measurements (Figure 4.11) were carried out before and after 1, 2, 5, 15, 30 min of UV/ozone exposure. The intensities of the E^1_{2g} and A_{1g} modes showed negligible attenuation for MLM and bulk MoS_2, while these two Raman modes completely disappeared after 30 min of UV/ozone exposure for SLM, indicating the loss of crystal symmetry and ordering in the SLM lattice.

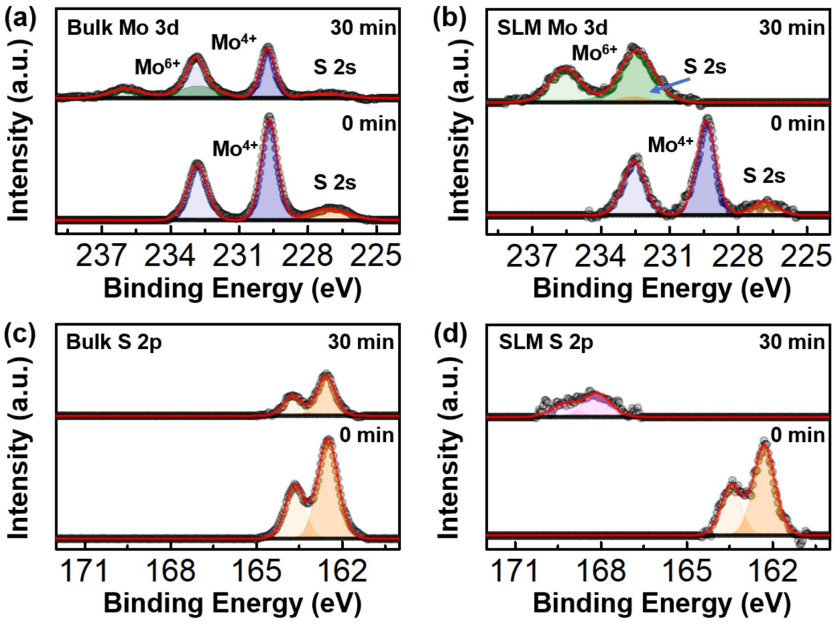

Figure 4.12: XPS characterization of MoS_2 on Au(111) before and after 30 min of UV/ozone exposure. (a) Bulk Mo 3d core level XPS spectra before and after 30 min of UV/ozone exposure. (b) SLM Mo 3d core level XPS spectra before and after 30 min of UV/ozone exposure. (c) Bulk S 2p core level XPS spectra before and after 30 min of UV/ozone exposure. (d) SLM S 2p core level XPS spectra before and after 30 min of UV/ozone exposure.

To fully understand the chemical transformation of MoS_2 nanosheets after extensive time of exposure, especially the resulting products on SLM, XPS was employed to fully characterize these

MoS_2 nanosheets. Figure 4.12 illustrates the XPS characterization of the chemical transformation of MoS_2 nanosheets before and after 30 min of UV/ozone exposure. As for bulk MoS_2, the signals at 229.5 eV and 232.6 eV can be assigned as Mo^{4+} $3d_{5/2}$ and Mo^{4+} $3d_{3/2}$ peaks. After 30 min of UV/ozone exposure, an additional Mo 3d doublet at binding energies of 232.7 eV and 235.9 eV is detected, which can be assigned to MoO_3 [183, 184]. A similar Mo 3d doublet (Mo^{6+}) was observed for SLM after 30 min of UV/ozone exposure. However, the Mo^{4+} signals disappeared at this point, suggesting all SLM was converted to a higher oxidation state. In addition, we observed peak broadening of Mo^{6+} signals as compared to Mo^{4+} peaks which was likely due to the creation of inhomogeneous surface potentials caused by uneven growth of MoO_3, consistent with the island-like structures seen in our AFM results (see above Figure 4.7) [185]. As for sulfur in bulk MoS_2, the signals at 162.4 eV and 163.6 eV can be assigned as $S(2p_{3/2})$ and $S(2p_{1/2})$ peaks, respectively. There was no significant shift in the peak position observed before and after 30 min of UV/ozone exposure, and the additional doublet at higher binding energies (that would result from S-O bonds, as shown in Figure 4.6) no longer exists. Combined with additional evidence that the sulfur peaks at 0 min became attenuated at 30 min, this confirms the conversion to MoO_3 at the top layers of MoS_2. The most interesting phenomenon is the unusual peak shift in the SLM S 2p spectrum after 30 min of UV/ozone exposure. Unlike bulk MoS_2, after 30 min of UV/ozone exposure, the S 2p doublet peaks, $S(2p_{3/2})$ and $S(2p_{1/2})$ in SLM shift up to 168.1 eV and 169.3 eV, respectively, indicating the formation of sulfate on the surface. The general chemical reaction associated with the MoS_2 oxidation can be described by the following reaction (note we only use O_2 as the oxidation source due to complexity of the gas components during the UV/ozone exposure, including O_2, O_3, and AO) [52, 186, 187]:

$$2MoS_2 + 7O_2 \rightarrow 2MoO_3 + 4SO_2 \tag{4.2}$$

Ross and Sussman [188] reported that the oxidation of MoS_2 in the presence of H_2O vapor would undergo the following reaction at elevated temperature (85 to 100 °C):

$$2MoS_2 + 9O_2 + 4H_2O \rightarrow 2MoO_3 + 4H_2SO_4 \quad (4.3)$$

Together with the results observed in our AFM, we propose that MLM (including BLM, TLM, and bulk MoS_2) undergo the general reaction pathway (Equation 4.2), in which MoS_2 only reacts with oxygen to form MoO_3 at the top layers of the films, consistent with the results reported in the literature [56, 171–173]. However, for SLM, the intimate contact with Au substrate catalyzes the oxidation process *via* charge transfer [124] and lowers the energy barriers for Equation 4.3. Therefore, SLM reacts with both oxygen and water at room temperature, producing MoO_3 and H_2SO_4, which could further react with each other to etch away the films and leave molybdenum sulfate formed as the final product. This would also be consistent with why MoS_2, fails as a functional friction modifier in humid environments [174].

4.4 Conclusions

In summary, we have systematically investigated the oxidation of MoS_2 on Au(111) surfaces under UV/ozone exposure. The reactive environment, which includes O_2, O_3, and AO gases, mimics the LEO environment, where MoS_2 is frequently employed s a friction reducing agent. Our work reveals that the extent and mechanism of oxidation depends strongly on the number of layers in the MoS_2 sample. After 1 min of UV/ozone exposure, SLM showed a higher reactivity as compared to MLM with the formation of S-O bonds on top of the MoS_2 nanosheets. After 15 min or longer time of UV/ozone exposure, although only the top-layer of MoS_2 was oxidized and converted to MoO_3 in MLM, SLM was partially etched away, leaving molybdenum sulfate formed as the final product. Our work reveals new insights of the support effect on the oxidation of two-dimensional materials, which provides a platform for more informed design of solid lubricant systems.

5. MECHANICAL AND ELECTRONIC PROPERTIES OF DIACETYLENE AND POLY-DIACETYLENE SELF-ASSEMBLED MONOLAYERS ON AU(111)*

5.1 Introduction

Self-assembled monolayers (SAMs) have attracted tremendous attention over the past few decades due to their potential applications in molecular electronics [189, 190]. There are numerous advantages to incorporating organic monolayers into electronic devices, such as their inherent nanometer size, increased functionality, and ability to be employed in bottom-up fabrication approaches. However, such miniaturization of electronic devices presents significant challenges. This is mainly due to the lack of fundamental understanding of the structure-function relationships, which relate to the synthesis, design, and assembling of molecules in the form of monolayers with stable and desirable properties. As an ideal model system that has been well characterized in fundamental research, alkanethiolates attached on Au surfaces have found widespread use as a background support to stabilize other guest molecules or molecule assemblies of interest. For example, one of the major results from our previous work has shown that by implementing alkanethiolates (dodecanethiolate in our case) to support porphyrin thiolate assemblies on Au(111), the charge transport mechanisms in porphyrin thiolate assemblies can be tuned by the nearest-neighbor interactions from a tunneling mechanism to a charge hopping mechanism [191]. The transition of the transport mechanisms was attributed to ensemble size effects since the charge-hopping characteristics were only observed in large (*ca.* 10 nm) porphyrin islands as compared to single porphyrin molecules. A problem we observed with using alkanethiolates as the surrounding matrix however, is that the local organization and the size of the assemblies cannot be well controlled from long periods of time, as the thiolates partially desorb from the Au surfaces with increased immersion time in solution [191–193].

Polyacetylene materials, especially two-dimensional polyacetylene thin films, have extensive

*Reprinted with permission from Wu, F.; Bhupathiraju, N.D.K.; Brown, A.; Liu, Z.; Drain, C.M.; Batteas, J.D. Mechanical and Electronic Properties of Diacetylene and Polydiacetylene Self-Assembled Monolayers on Au (111). *J. Phys. Chem. C* **2020**, *124*(7), 4081-4089. Copyright 2020 by American Chemical Society.

applications in photonics, molecular electronics, batteries, and solar cells [194–196]. One way to fabricate polyacetylene materials is to add functional groups that can covalently bond to the underlying substrates. Thiol-terminated poly-diacetylenes, with their highly conjugated polymer structures, provide abundant possibilities to fabricate robust monolayers when attached to Au surfaces [60, 197–206]. Similar to diacetylene solids or Langmuir-Blodgett films, the polymerization of DATs on Au(111) surfaces can be initiated by UV-irradiation [197]. The highly conjugated polymer structures, combined with covalent bonds to the Au substrates, result in a more rigid feature compared to typical alkanethiolate monolayers. Additionally, the poly-DATs exhibit excellent stability to repeated electrochemical cycling at extreme conditions, high temperature annealing up to 200 °C, and long-time exposure to hot base solutions [60].

The superior stability of the poly-DATs as compared to the unpolymerized DATs or alkanethiolates, inspired us to implement a comprehensive study of these molecules and investigate their structure-function relationships in terms of mechanical stability and electronic properties. Here, we explore the diacetylene thiol $HS(CH_2)_3C{\equiv}C{-}C{\equiv}C(CH_2)_4CH_3$ (C3-DAT) on Au(111) surfaces before and after polymerization. The molecules were synthesized to have the same chain length as dodecanethiols for direct comparison. Fourier-transform infrared spectroscopy (FTIR), Raman spectroscopy, X-ray photoelectron spectroscopy (XPS), atomic force microscopy (AFM), scanning tunneling microscopy (STM), and scanning tunneling spectroscopy (STS) collectively, elucidate the mechanical and electronic properties of C3-DATs and C3-poly-DATs on Au(111).

5.2 Experimental Methods

Synthesis of DATs

C3-DAT ($HS(CH_2)_3C{\equiv}C{-}C{\equiv}C(CH_2)_4CH_3$) was synthesized by a four-step procedure which had been described in a previously published method [207]. This was a redesigned synthesis that allowed 80% overall yields and gram-scale production.

Self-Assembled Monolayer (SAM) Preparation

C3-DAT SAM Preparation Self-assembled C3-DAT monolayers were adsorbed onto 200 nm thick, flamed annealed Au(111) on mica surfaces (Phasis, Geneva Switzerland). Before monolayer adsorption, the Au(111) substrates were treated with UV/ozone for 10 minutes, rinsed with ultrapure water (18.2 MΩ·cm), rinsed with ethanol (Koptec, 200 proof) and dried with streaming N_2. Next, Au samples were exposed to UV/ozone (Novascan PSD-UV, UV wavelength at 185 nm and 254 nm) for another 5 minutes and cleaned again with the same procedure described above. The Au samples were then immersed in 1mM C3-DATs in ethanol solution for 48 hours. The exposure to natural light was minimized during the sample preparation. Following the monolayer formation, the samples were removed from the solution, rinsed with ethanol and dried with streaming N_2. The samples were then transferred and stored in a UHV chamber ($\sim 10^{-10}$ mbar) for future characterization.

Mixed SAM Preparation Prior to mixed monolayer adsorption, the Au(111) surfaces were cleaned with the same procedure described above. The substrates were then immersed in 1 mM dodecanethiol (Aldrich, 98%, used as received) in ethanol solution for one day. Following the formation of the dodecanethiolate SAMs, the substrates were rinsed with ethanol, dried with N_2, and immersed in 0.1 mM C3-DAT in ethanol for one day. After that, the substrates were removed from the C3-DAT solution, rinsed with ethanol and dried with streaming N_2.

UV-Induced Polymerization For the UV-induced polymerization, the samples were placed inside a well-sealed container and irritated with a UV lamp (same UV source as above) under a N_2 purge for five minutes. It was important to note that the samples remained complete without photooxidation occurring under this irradiation condition (as determined by the following STM results).

Fourier Transform Infrared (FTIR) Spectroscopy

FTIR spectra were collected with a Thermo Nicolet 6700 equipped with an attenuated total reflection accessory (VariG-ATR, Ge crystal, incidence angle 65°C) and a liquid-nitrogen cooled

MCT (HgCdTe) detector. Spectra were collected with 512 scans at a resolution of 4 cm^{-1} for both C3-DATs and C3-poly-DATs films. Omnic (version 8.2) software was employed for the FTIR data analysis.

Raman Microspectroscopy

Raman microspectroscopy was employed to identify the UV induced polymerization. A WiTec Alpha 300R (Germany) equipped with a Nikon objective (50×, 0.9 N.A.) was used to characterize C3-DAT and C3-poly-DAT films. Reported spectra were each an average of 3 scans with an integration time of 5 seconds using 1800 g/mm grating and 532 nm excitation source. The laser power was kept at 12.5 mW for all measurements. All the Raman spectra were processed with WITec Suite 4.0 software (Project FOUR).

X-ray Photoelectron Spectroscopy (XPS)

XPS measurements were obtained with a Scientia Omicron ESCA+ X-ray photoelectron spectrometer equipped with a Mg Kα radiation source (1253.6 eV, source power 300 W, 15 kV, 20 mA). The energy resolution is *ca.* 0.8 eV with a spot size of *ca.* 54 μm. The base pressure of the analysis chamber was maintained in the $\sim 10^{-10}$ mbar range. Survey scans were acquired at a passing energy of 100 eV with 1.0 eV steps and a dwell time of 0.1 s. Multiplexed high-resolution scans of C(1s) and S(2p) were carried out at a passing energy of 20 eV with 0.05 eV steps and a dwell time of 0.1 s. The survey and high-resolution spectra were averaged with 3 and 50 scans, respectively. All the peak positions were calibrated with respect to the Au ($4f_{7/2}$) peak at 84.0 eV. Casa (version 2.3.22) software was employed for the XPS data analysis.

Atomic Force Microscopy (AFM)

Contact mode AFM (Agilent 5500) measurements were carried out with silicon tips (Mikromasch CSC37) in a dry nitrogen environment (relative humidity $<0.1\%$ and at room temperature). The normal spring constants were *ca.* 0.2 N/m which were determined by the Sader method [208]. The tip radii were *ca.* 10-20 nm which were calibrated by the blind tip reconstruction utilizing the standard procedure with Scanning Probe Image Processor (SPIP, version 6.0.2, Image Metrology,

Lyngby, Denmark). The lateral force calibration factors were determined by the corrected direct force balance method for the friction force measurements [209]. FD curves (1000 data point) were acquired with a maximum applied load of 10 nN, during time 1s, and an approach and retract rate of 2 μm/s. Force-volume mapping with a 16 $\times$ 16 point grid was used to obtain FD curves on 250 nm^2 surfaces. The force-volume mapping was taken before and after the friction measurements to confirm no tip changes occurred during scanning. Friction *vs* load curves were carried out using a pre-coded script to increase and decrease the applied load during the friction force measurements. On a 250 nm^2 area with a 256 point/line resolution, the nominal load was ramped from -10 to 20 nN, with the tip being temporarily brought out of contact with the sample in between the loading and unloading cycles. Each loading and unloading cycle were measured and averaged three times for each of the measured C3-DAT and C3-poly-DAT areas.

Scanning Tunneling Microscopy (STM) and Scanning Tunneling Spectroscopy (STS)

STM images were collected with a variable-temperature scanning tunneling microscope (VT-STM) (Scientia Omicron GmbH, Germany) system. The base pressure was maintained in $\sim 10^{-10}$ mbar range. Mechanically cut Pt/Ir (80/20) tips were used for constant-current imaging in a tip biasing and sample grounding configuration. Detailed bias voltages and tunneling currents were indicated in each STM figure. One hundred I-V curves were collected and averaged for each STS measurement, by sweeping the voltage bias from -2 V to 2 V. The setpoint used to stabilize the tunneling gap was +1.4 V and 20 pA. To avoid various tip effects, I-V spectra were discarded if the following imaging showed tip changes after the spectra were collected. All the images and the I-V spectra were taken at room temperature and analyzed with SPIP.

5.3 Results and Discussion

5.3.1 Spectral Characterization of C3-DATs and C3-Poly-DATs on Au(111)

Figure 5.1 shows the spectral characterization of C3-DATs and C3-poly-DATs on Au(111) surfaces. Vibrational transitions at 2923 cm^{-1} and 2854 cm^{-1} (FTIR spectra in Figure 5.1a) arise from the asymmetric and symmetric stretching modes of CH_2, respectively. An additional mode around

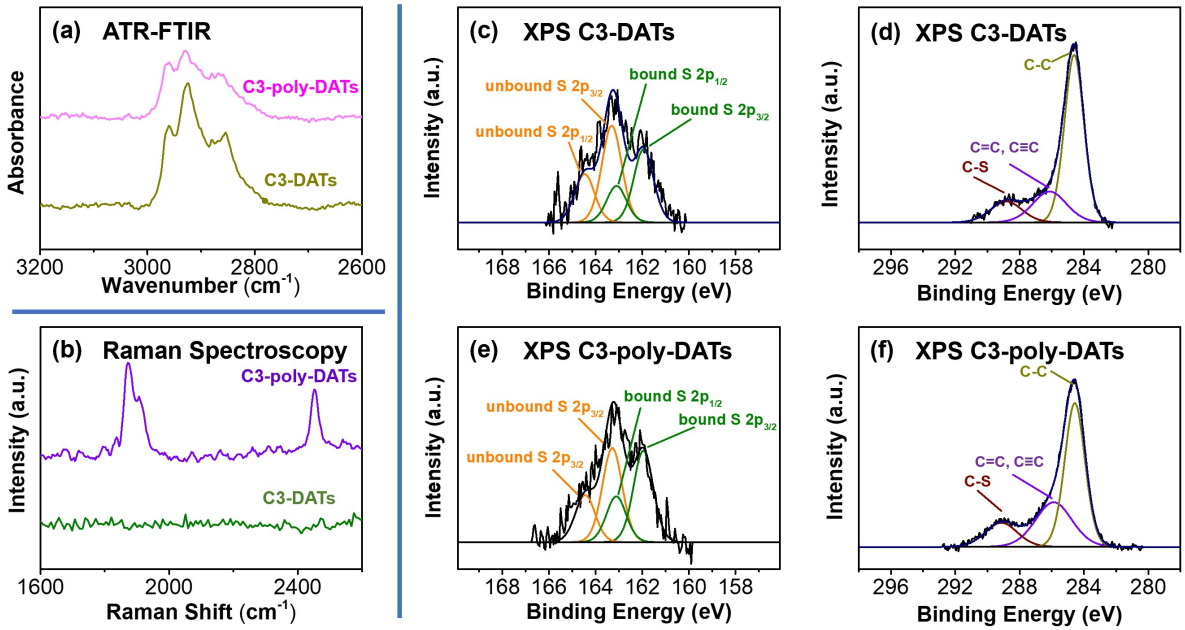

Figure 5.1: Spectral characterization of C3-DATs and C3-poly-DATs on Au(111) surfaces. (a) ATR-FTIR spectra of C3-DATs and C3-poly-DATs on Au(111) surfaces. (b) Raman spectra of C3-DATs and C3-poly-DATs on Au(111) surfaces. (c) S(2p) core level XPS spectra of C3-DATs on Au(111) surfaces. (d) C(1s) core level XPS spectra of C3-DATs on Au(111) surfaces. (e) S(2p) core level XPS spectra of C3-poly-DATs on Au(111) surfaces. (f) C(1s) core level XPS spectra of C3-poly-DATs on Au(111) surfaces.

2960 cm^{-1} can be assigned to the Fermi resonance of the methyl asymmetric stretch [210–212]. These vibrational modes confirm the existence of C3-DATs and C3-poly-DATs on Au surfaces. After polymerization, there is no shift in the position of these peaks, although there is a slight decrease in the peak intensity. This is due to the polymerization process which induces the decrease of the tilting angle inside the alkyl chains [200]. Raman spectra from Figure 5.1b further confirm the polymerization of C3-DATs on Au(111) surfaces. Before UV irritation, there were no peaks observed for C3-DATs. After UV irritation for 5 minutes, the spectrum shows vibrational modes around 1875 cm^{-1} and 2450 cm^{-1} which can be attributed to double and triple bonds after polymerization. As expected, these peaks are blue-shifted relatively to the peaks reported in the literature due to the odd-numbered nature of the spacer as well as the spacer length effects (relative short spacer group comparing to literature) [199]. Figure 5.1c to Figure 5.1f illustrate the XPS spectra

for S(2p) and C(1s) before and after polymerization. Overall, there are no significant differences in the XPS spectra for both C3-DATs and C3-poly-DATs. However, the deconvolution of the S(2p) demonstrates two different sets of S peaks. Here, we assign the signals at 163.1 eV and 161.9 eV as $S(2p_{1/2})$ and $S(2p_{3/2})$ for bound S to the Au substrates. The signals at 164.5 eV and 163.3 eV are identified as $S(2p_{1/2})$ and $S(2p_{3/2})$ for unbound S species. We postulate that when the C3-DATs are assembled on the Au surfaces, some are directly stabilized on the surfaces through the S-Au bonds, while others are assembled by intercalation without the formation of any bonds to the Au substrates (another explanation could possibly be the formation of diacetylene dimers containing S-S bonds during the self-assembling process). This is further confirmed by AFM and STM as discerned by the formation of cluster-like features taller than the background SAM matrix. In terms of the C peaks, the signals at 288.8 eV, 286.1 eV, and 284.8 eV for the C 1s spectra can be assigned to C−S, C≡C (or C=C), and C−C groups, respectively [213].

5.3.2 AFM Characterization of C3-DATs and C3-Poly-DATs on Au(111)

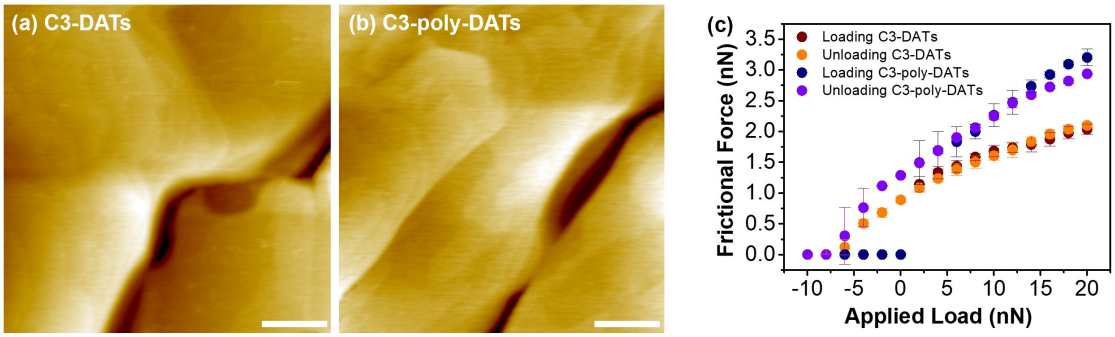

Figure 5.2: AFM characterization of C3-DATs and C3-poly-DATs on Au(111) surfaces. (a) Topography image of C3-DATs on Au(111) surfaces (applied load 1 nN) (scale bar = 200 nm). (b) Topography image of C3-poly-DATs on Au(111) surfaces (applied load 1 nN) (scale bar = 200 nm). (c) Friction force vs applied load curves for C3-DATs and C3-poly-DATs. The loading and unloading cycles for C3-DATs are represented by wine and orange dots, respectively. The loading and unloading measurements for C3-poly-DATs are represented by navy and violet dots respectively.

Figure 5.2 demonstrates the AFM characterization of C3-DATs and C3-poly-DATs on Au(111)

surface. Figure 5.2a and Figure 5.2b illustrate the topography images before and after polymerization at a relatively small load ($\sim$ 1 nN). Contrasting against the well-known structure of alkanethiolates on Au(111), we have seen molecular clusters scattered throughout the whole surfaces. After the polymerization, these clusters become less noticeable which indicates a structural evolution during the formation of the polymer backbones. Due to the resolution limitation of our AFM, a more accurate and detailed discussion of these clusters is given below based on STM measurements.

Friction force measurements have been performed with the same AFM tips for both C3-DATs and C3-poly-DATs to assess the impact of polymerization on the mechanical properties of the tip-SAM interface. Figure 5.2c demonstrates the representative load-dependent frictional behavior of C3-DATs and C3-poly-DATs on Au(111) surfaces. For the loading cycles, the applied load is increased from -10 nN to +20 nN and for the unloading cycles, the applied normal force is decreased from +20 nN to -10 nN, respectively. The AFM tips snap into contact at *ca.* +2 nN during the loading measurements and snap out of contact at *ca.*-8 nN during the unloading cycles for both C3-DAT and C3-poly-DAT samples. The tips were calibrated before and after the friction measurements to ensure that no changes to the tips occurred from the measurement. From Figure 5.2c, hysteresis is observed between the loading and unloading cycles for both C3-DATs and C3-poly-DATs. Additionally, these monolayers also exhibit higher frictional response as compared to dodecanethiolate SAMs reported in the literature [214]. The greater frictional response and the hysteresis behavior of C3-DATs and C3-poly-DATs together, indicate a lower crystallinity and a higher degree of disorder (as compared to dodecanethiolate SAMs), which is consistent with our FTIR spectra. Furthermore, C3-poly-DATs also shows higher friction as compared to C3-DATs at all applied positive loads. Such a trend shows consistency to previous work reported by Mowery *et al.* [215]. Generally self-assembled diacetylene monolayers show different structural order due to the presence of internal molecular scaffoldings that organize the monolayers laterally. Thus, the monolayer structures can be considered to consist of three different regions: the spacer regions between the surface and the diacetylene, the tail regions over the diacetylene, and the diacety-

lene regions themselves. Before polymerization, the crystallinity of the C3-DATs can be treated as the entire monolayers themselves with enhanced internal interaction due to the strong $\pi - \pi$ stacking. However, after polymerization, the crystallinity needs to be re-considered by different regions. This is verified by several studies showing that diacetylene monolayers of different tail and spacer groups have illustrated two spectroscopically discernible regions, corresponding to the spacer and the tail groups [204, 206]. Therefore, the mechanical properties of the C3-poly-DATs are highly dependent on the structures in the tail regions since the diacetylene and the spacer regions are locked by the UV-induced polymerization. With this in mind, we can understand the different frictional behavior between C3-DATs and C3-poly-DATs when considering the underlying mechanisms influencing the associated difference in both molecular spacing and chain-length dependent local ordering.

5.3.3 STM/STS Characterization of C3-DATs and C3-Poly-DATs on Au(111)

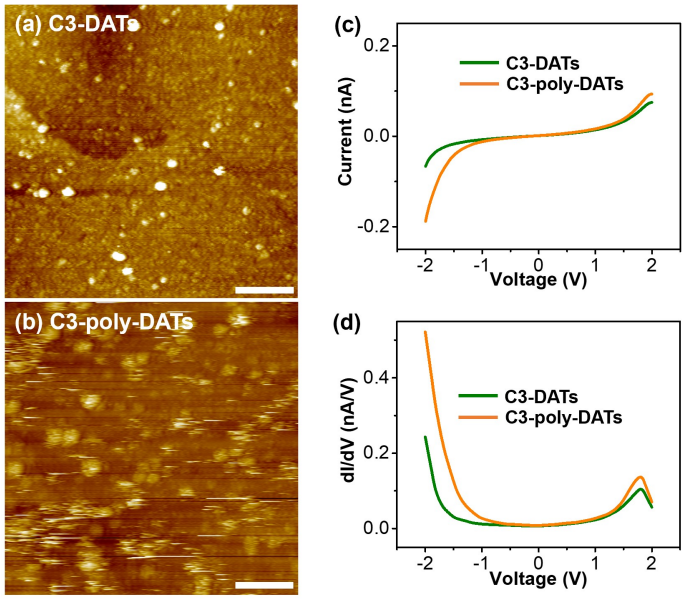

Figure 5.3: STM/STS characterization of C3-DATs and C3-poly-DATs on Au(111) surfaces. (a) STM image (V_{bias} = +1.4V, I_t = 20 pA) of C3-DATs on Au(111) (scale bar = 20 nm). (b) STM image (V_{bias} = +1.4V, I_t = 20 pA) of C3-poly-DATs on Au(111) (scale bar = 20 nm). (c) Averaged IV curves (100 curves for each) of C3-DATs and C3-poly-DATs on Au(111). (d) Numerically calculated derivatives (dI/dV spectra) of the I-V curves in Figure (c).

First, after polymerization, there is an intrinsic, although not significant, expansion within the SAMs, due to the formation of the covalent bonds. Therefore, the van der Waals forces stabilizing the tail regions diminish which results in a lower local ordering in the tail regions and a higher frictional response. Second, it is well-known that the frictional forces depend strongly on the number of carbon atoms in the molecular chains [214]. For example, when the number of carbon atoms in the molecular chains is larger than eleven, the friction forces are relatively similar for alkanethiolates. For the number of carbon atoms less than eleven, the frictional behavior is noticeably different. The higher frictional response for short-chain length is attributed to the increased disorder that occurs when decreasing the carbon number. Before polymerization, the C3-DATs (twelve carbon atoms in our case) are stabilized together by the van der Waals interactions. After polymerization, due to the interlock inside the diacetylene regions, the C3-poly-DAT films are expected to have a higher compressibility as the tail groups are now stabilized by a reduced number of carbon atoms (five carbon atoms). Therefore, a lower local ordering occurs which makes it possible to excite numerous surface defects and energy-dissipating channels, increasing the frictional response for C3-poly-DATs at the same applied load. Although the overall monolayer rigidity increases due to the polymerization, the rigidity of the tail regions decreases due to the two mechanisms discussed above.

To better understand the structural evolution of C3-DATs caused by the UV-induced polymerization, it is necessary to fully characterize both C3-DATs and C3-poly-DATs using STM which provides a higher resolution. Additionally, STS has also been implemented at the same time to extract the electronic information before and after polymerization transition. First, from Figure 5.3a and Figure 5.3b, similar molecular clusters are observed for both C3-DATs and C3-poly-DATs. This is consistent with the AFM topography images and the XPS spectra describe above, showing part of the SAMs intercalated into the background SAMs as molecular clusters without bonding to the Au surfaces. The height of the C3-DAT clusters ranges from 0.25 nm to 1.3 nm and the lateral size varies from 3 nm to 7 nm. The height of the C3-poly-DAT clusters ranges from 0.25 nm to 1.2 nm and the lateral sizes varies from 4 nm to 8 nm. The height of the molecular clusters

shows no significant change after polymerization, while the lateral dimension increases slightly. In addition, small crystal domains with averaged size around 5 nm appear in the background SAMs after polymerization (Figure 5.3b). This is contrary to earlier findings, in which the polymerization is known to result in unidirectional micro-sized domains in Langmuir-Blodgett films [216, 217]. The reason behind could possibly be the increased interactions between the thiolate groups and the substrates which limits the degree of freedom within the monolayers as well as the relative short spacer length. It is difficult to obtain molecular-resolution images for both C3-DATs and C3-poly-DATs, because of the relatively higher defect densities and smaller domain sizes. Another noteworthy phenomenon differs from typical alkanethiolates on gold is that the etch pits in C3-DATs are very small and scattered throughout the whole surfaces (Figure 5.3a). The depth measured is around 0.25 nm, similar to the etch pit depth in alkanethiolates on Au surfaces. The feature becomes less obvious in Figure 5.3b as the crystallinity decreases during polymerization. In the most widely accepted mechanism proposed by Poirier [218], the formation of the etch pits is explained by the surface relaxation and reconstruction process. During SAM formation, two Au atoms are released per primitive unit cell and then leave one vacancy behind in one primitive unit cell. The Au atoms diffuse and attach to the step edges while the vacancies nucleate and grow into large vacancy islands in the terraces which are called etch pits. Following such a consideration, the difference in the etch pit structures between C3-DATs/C3-poly-DATs and alkanethiolates can be attributed to the decreased mobility of the vacancies during the adsorption process. It has been reported that the metal-metal bonds can be weaken due to the chemical adsorption [219, 220]. The weakening magnitude is mainly determined by surface coverage and the adsorbate-metal bonding strength. Due to the highly conjugated structure inside the C3-DAT/C3-poly-DAT chains, the S-Au bonding energies are inferred to be weaker compared to the alkanethiolate SAMs, which leads to a higher diffusion barrier and a low mobility for the surface metal atoms. Similar results have also been reported for arenethiolate SAMs from previous literature [221]. Note that the STM images of C3-poly-DATs appear less defined than that in the C3-DAT SAMs, with additional streaks and spikes shown in the images. There are comments arguably saying this might be due to the

contaminants from the environment during the UV-induced polymerization process. However, our experiments on C3-poly-DATs embedded in dodecanethiolate matrix illustrate atomic resolution images after polymerization, clearly indicating the UV process in N_2 environment will not cause any contamination or oxidation issues to the SAMs on Au surfaces.

Figure 5.3c and Figure 5.3d demonstrate the representative I-V and dI/dV spectra on C3-DATs and C3-poly-DATs from a voltage range of -2 V to +2 V. Note the reason to choose such a bias range is because reliable I-V data has barely been achieved successfully larger than 2.5 V due to the junction breakdown in large electric fields. Unexpectedly, these spectra look very similar in both I-V and dI/dV. The main difference between C3-DATs and C3-poly-DATs is the higher current magnitude at greater bias for C3-poly-DATs (especially at negative bias region) compared to C3-DATs, which could arise from resonant tunneling due to the conjugated backbone structures. Small shoulder-like features at around 1.8 V can be attributed to Au-S bonds at the C3-DATs/C3-poly-DATs interfaces. The electronic structures for the molecular clusters are not discussed here due to the wild and random behaviors of the I-V measurements on these locations.

To understand the size-dependent electronic and transport properties of C3-DATs/C3-poly-DATs on Au(111) surfaces, mixed monolayers of C3-DATs/C3-poly-DATs and dodecanethiolates are prepared. Figure 5.4 and Figure 5.5 demonstrate the STM/STS characterization of C3-DATs and C3-poly-DATs within dodecanethiolate background matrix on Au(111) surfaces. The background molecules are dodecanethiolates and the bright protrusions are C3-DAT/C3-poly-DAT islands. The molecular structures are well-resolved for dodecanethiolates and the C3-DAT/C3-poly-DAT islands are more organized within the dodecanethiolate surrounding matrix. The apparent height measured for C3-DAT SAMs is approximately 0.1 nm higher compared to dodecanethiolates, while the apparent height difference between C3-poly-DATs and dodecanethiolates is around 0.2 nm (see Figure 5.6 and Figure 5.7). The transformation in apparent height could either originate from the height change after polymerization or be due to a greater conductance for C3-poly-DATs since the apparent height measurement in STM is a convolution of both geometric and electronic effects.

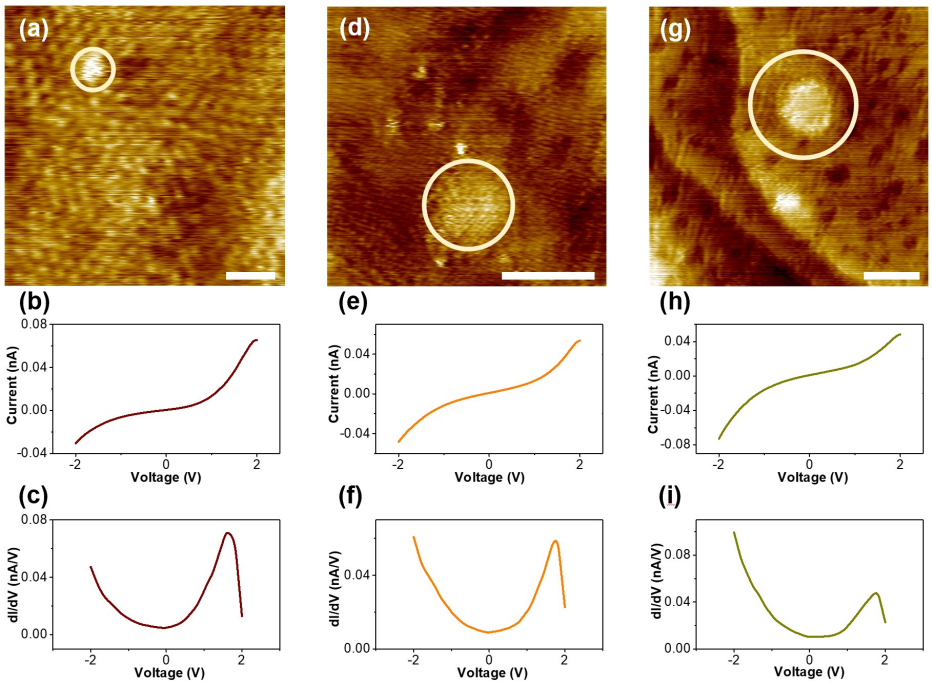

Figure 5.4: STM/STS characterization of C3-DATs within dodecanethiolate background matrix on Au(111). (a) STM image (V_{bias} = +1.4V, I_t= 20 pA) of a C3-DAT island (∼1 nm in size) surrounded by dodecanethiolates on Au(111) (scale bar = 2 nm). (b) and (c) Corresponding I-V (averaged by 100 times) and dI/dV (numerically calculated from I-V) curves of the C3-DAT island within dodecanethiolate matrix in (a). (d) STM image (V_{bias} = +1.4V, I_t = 20 pA) of a C3-DAT island (∼10 nm in size) surrounded by dodecanethiolates on Au(111) (scale bar = 10 nm). (e) and (f) Corresponding I-V (averaged by 100 times) and dI/dV (numerically calculated from I-V) curves of the C3-DAT island within dodecanethiolate matrix in (d). (g) STM image (V_{bias} = +1.4V, I_t = 20 pA) of a C3-DAT island (∼20 nm in size) surrounded by dodecanethiolates on Au(111) (scale bar = 20 nm). (h) and (i) Corresponding I-V (averaged by 100 times) and dI/dV (numerically calculated from I-V) curves of the C3-DAT island within dodecanethiolate matrix in (g).

All I-V curves on C3-DAT islands (Figure 5.4) show asymmetric features from a voltage range of -2 V to +2 V. The asymmetry within all I-V curves is due to the experimental factors such as material differences between tips (Pt/Ir) and substrates (Au), and the intrinsic asymmetry of the C3-DATs employed in our experiments. However, there are some interesting differences observed in electronic properties (I-V and dI/dV) of the C3-DAT SAMs (Figure 5.3c and Figure 5.3d) as compared to the C3-DAT islands (STS in Figure 5.4). For the ∼ 1 nm C3-DAT islands (Figure 5.4 a,b,c), the I-V curve shows a higher conductance at positive tip bias comparing to negative tip bias. As the size of the islands increase from ∼ 1 nm to ∼ 10 nm (Figure 5.4 d,e,f), then to ∼

20 nm (Figure 5.4 g,h,i), the higher conductance shifts from the positive region to the negative region. In fact, for island sizes $\sim$ 20 nm, the I-V spectra (also dI/dV) already looks very similar to the complete C3-DAT SAMs on Au(111) (Figure 5.3c and Figure 5.3d). It is expected that for small C3-DAT islands (single or a few C3-DAT molecules, total size $\sim$ 1-2 nm), the current should be much larger for positive tip voltage (electron transport through HOMO) than for negative tip voltage (electron transport through LUMO) since the highest occupied molecular orbital (HOMO) is a sulfur-based level that couples much stronger to the Au compared to the lowest unoccupied molecular orbital (LUMO). However, as the C3-DAT island increases in size (*e.g.* to $\sim$ 20 nm), due to the strong $\pi-\pi$ stacking in the diacetylene regions, the nearest-neighbor interactions appreciably alter the alignment of the frontier orbitals comparing to the Fermi level of the electrodes, which shifts the transport through LUMO more favorable at negative tip bias.

Figure 5.5 illustrates the STM/STS characterization of C3-poly-DATs within the dodecanethiolate background matrix. Again, molecular resolution is still achievable after polymerization, clearly indicating that UV exposure in N_2 environment does not lead to any degradation to the SAMs on Au(111) surfaces. The most interesting results emerge when measuring the I-V on these C3-poly-DAT islands. Figure 5.5b and Figure 5.5c demonstrate the I-V curve and the corresponding dI/dV curve of the poly-DAT island ($\sim$ 1-2 nm) in dodecanethiolate matrix. Based on the size and packing density of C3-DAT SAMs on Au(111) surfaces, such a small island of 1-2 nm could contain 2 to 5 polymerized C3-DAT molecules. Surprisingly, the electronic structure measured for the C3-poly-DAT island ($\sim$ 1-2 nm) shows appreciable difference as nearly no gap was observed in the dI/dV curve (Figure 5.5c), suggesting the higher conductance for C3-poly-DAT island ($\sim$ 1-2 nm) compared to C3-DAT island (of same size) and C3-poly-DAT SAMs. Although very insignificant, additional densities of states show up around -1.01 V and +0.34 V (Figure 5.5c) compared to C3-poly-DAT SAMs (Figure 5.3d), indicating the band structure change, as well as new transport mechanisms being activated after polymerization. Similar results have also been observed for C3-poly-DAT island around 20 nm in size (Figure 5.5h and Figure 5.5i), showing a higher conductance character and mid-gap states appearing around -1.29 V and +0.30 V with

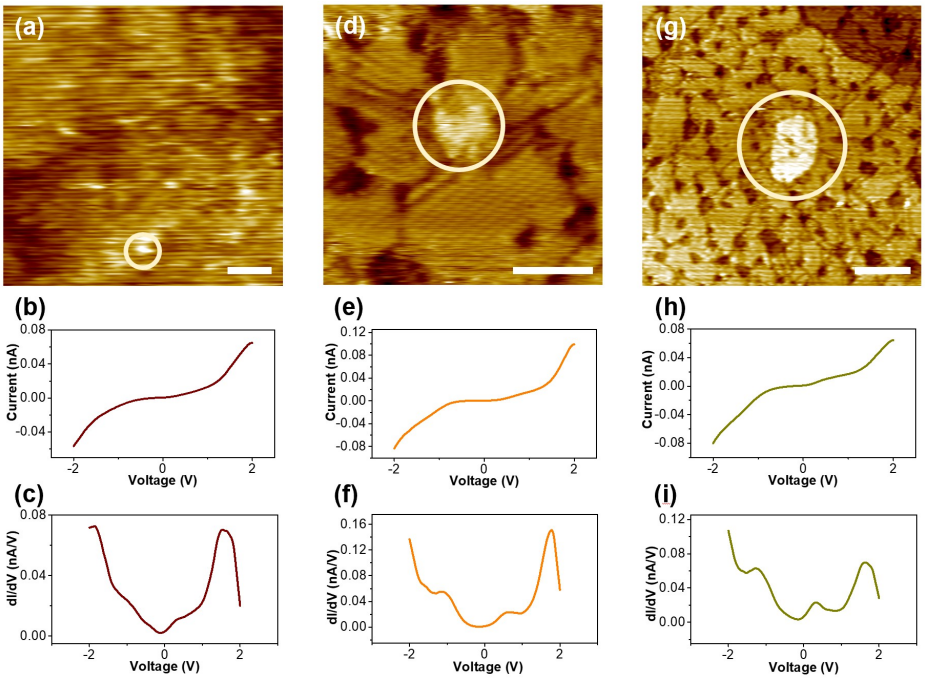

Figure 5.5: STM/STS characterization of C3-poly-DATs within dodecanethiolate background matrix on Au(111). (a) STM image (V_{bias} = +1.4V, I_t = 20 pA) of a C3-poly-DAT island ($\sim$1 nm in size) surrounded by dodecanethiolates on Au(111) (scale bar = 2 nm). (b) and (c) Corresponding I-V (averaged by 100 times) and dI/dV (numerically calculated from I-V) curves of the C3-poly-DAT island within dodecanethiolate matrix in (a). (d) STM image (V_{bias} = +1.4V, I_t = 20 pA) of a C3-poly-DAT island ($\sim$10 nm in size) surrounded by dodecanethiolates on Au(111) (scale bar = 10 nm). (e) and (f) Corresponding I-V (averaged by 100 times) and dI/dV (numerically calculated from I-V) curves of the C3-poly-DAT island within dodecanethiolate matrix in (d). (g) STM image (V_{bias} = +1.4V, I_t = 20 pA) of a C3-poly-DAT island ($\sim$20 nm in size) surrounded by dodecanethiolates on Au(111) (scale bar = 20 nm). (h) and (i) Corresponding I-V (averaged by 100 times) and dI/dV (numerically calculated from I-V) curves of the C3-poly-DAT island within dodecanethiolate matrix in (g).

increased intensities. If we now turn to C3-poly-DAT islands of $\sim$ 10 nm, the dI/dV measurement (Figure 5.5e and Figure 5.5f) exhibits analogous new states at around -1.13 V and 0.60 V. However, a blockade-like behavior is observed in which the current is considerably suppressed with the voltage range from -0.5 V to +0.2 V. We believe the unique I-V (or dI/dV) for the C3-poly-DAT island ($\sim$ 10 nm) results from the single electron tunneling effects, *i.e.* Coulomb blockade. For comparison, the I-V curve (dI/dV) has also been measured on dodecanethiolate SAMs as a reference (see Figure 5.8). The I-V curve is relatively linear with small slopes at low bias, consistent

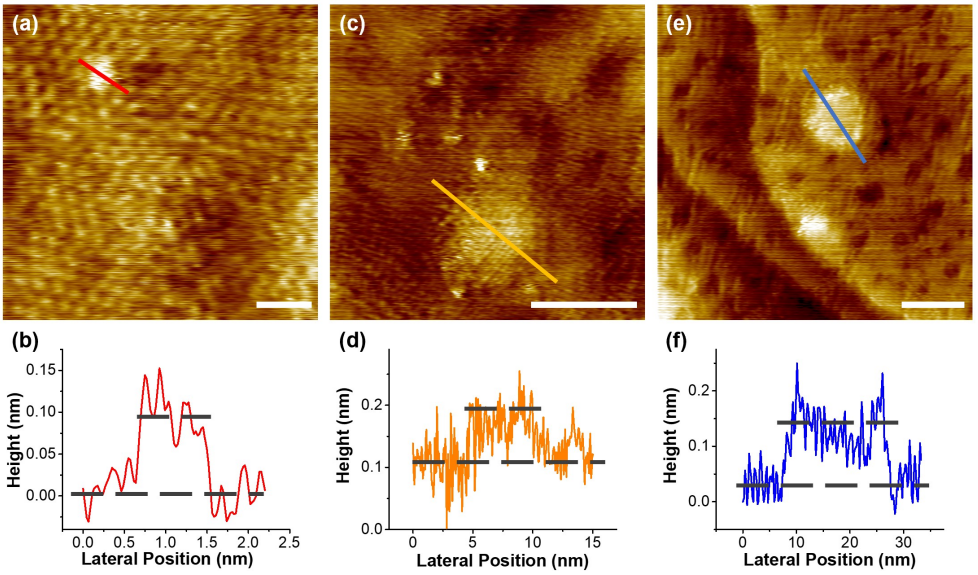

Figure 5.6: STM characterization of C3-DATs within dodecanethiolate background matrix on Au(111). (a) STM image (V_{bias} = +1.4V, I_t = 20 pA) of a C3-DAT island (∼1 nm in size) surrounded by dodecanethiolates on Au(111) (scale bar = 2 nm). (b) Height profile taken across the C3-DAT island (∼1 nm in size) along the direction marked by the red line in (a). (c) STM image (V_{bias} = +1.4V, I_t = 20 pA) of a C3-DAT island (∼10 nm in size) surrounded by dodecanethiolates on Au(111) (scale bar = 10 nm). (d) Height profile taken across the C3-DAT island (∼10 nm in size) along the direction marked by the orange line in (c). (e) STM image (V_{bias} = +1.4V, I_t = 20 pA) of a C3-DAT island (∼20 nm in size) surrounded by dodecanethiolates on Au(111) (scale bar = 20 nm). (f) Height profile taken across the C3-DAT island (∼20 nm in size) along the direction marked by the blue line in (e).

with no Coulomb blockade in dodecanethiolate SAMs. To achieve the Coulomb blockade, two conditions must be met for the observation of single electron tunneling effects at room temperature. First, the thermal energy of the system (K_{BT}) must be below the charging energy of the island ($E_c = e^2/2C$); Second, the tunneling resistance R_t, should be large than $h/2\pi e^2$, due to the Heisenbergs uncertainty principle. In order to analyze the Coulomb blockade effects, the semi-classical double barrier tunneling junction (DBTJ) model is implemented here [222, 223]. The schematic of the two tunneling junctions are shown in Figure 5.9. The first tunneling junction contains the alkane spacer groups sandwiched by the diacetylene regions and the Au substrates. The second tunneling junction consists of an insulating alkane barrier between the STM tip and the highly conductive diacetylene regions. Each junction has a capacitance and an effective resistance,

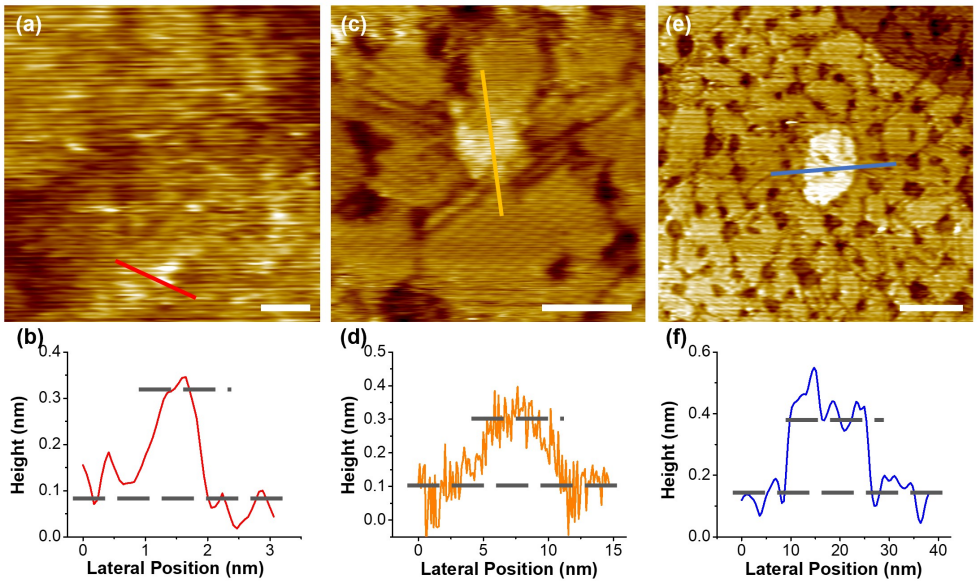

Figure 5.7: STM characterization of C3-poly-DATs within dodecanethiolate background matrix on Au(111). (a) STM image (V_{bias} = +1.4V, I_t = 20 pA) of a C3-poly-DAT island (∼1 nm in size) surrounded by dodecanethiolates on Au(111) (scale bar = 2 nm). (b) Height profile taken across the C3-poly-DAT island (∼1 nm in size) along the direction marked by the red line in (a). (c) STM image (V_{bias} = +1.4V, I_t = 20 pA) of a C3-poly-DAT island (∼10 nm in size) surrounded by dodecanethiolates on Au(111) (scale bar = 10 nm). (d) Height profile taken across the C3-poly-DAT island (∼10 nm in size) along the direction marked by the orange line in (c). (e) STM image (V_{bias} = +1.4V, I_t = 20 pA) of a C3-poly-DAT island (∼20 nm in size) surrounded by dodecanethiolates on Au(111) (scale bar = 20 nm). (f) Height profile taken across the C3-poly-DAT island (∼20 nm in size) along the direction marked by the blue line in (e).

which are represented by C_i and R_i, with i = 1 or 2. Generally, a fractional charge Q_0 exists on the diacetylene regions, which is arguably originated from the work function difference between the electrodes within the junctions, permitting the asymmetry of the I-V curves in our case. From Figure 5.5e and Figure 5.5f, the charging energy of the Coulomb blockade island (∼ 10 nm) is determined at around 0.30 eV and therefore, the corresponding total tunneling capacitance C_t can be calculated as $C_t = e^2/2E_c = 2.67 \times 10^{-19}$ F. Based on the calculated total capacitance, the effective diameter is determined as $d = C_t/2\pi\varepsilon\varepsilon_0 = 1.9$ nm for this two-dimensional Coulomb blockade island. In addition, based on the equation developed by Hanna *et al.* [222], R_2 can be extracted at around 37 GΩ, as well as $C_1 = 2.21 \times 10^{-19}$ F, $C_2 = 0.46 \times 10^{-19}$ F, and $Q_0 = 0.32$e. The insignificant appearance of the Coulomb blockade effects within the small C3-poly-DAT is-

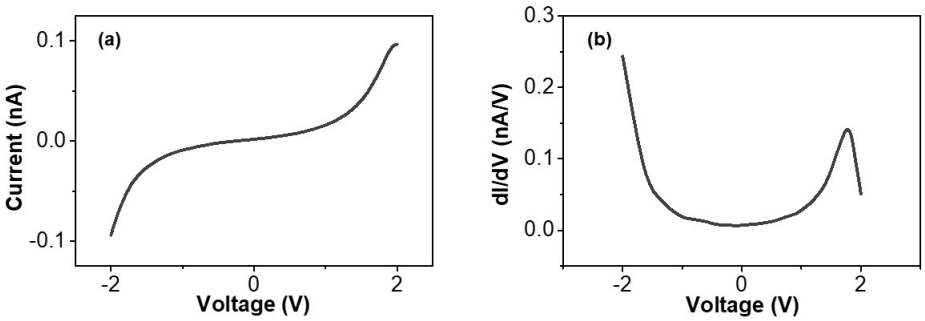

Figure 5.8: STS characterization of dodecanethiolate SAMs on Au(111) surfaces. (a) I-V (average of 100 scans) and (b) dI/dV (numerically calculated from I-V) curves of the dodecanethiolate SAMs. The setpoint used to stabilize the tunneling gap in I-V measurements is 1.4 V and 20 pA.

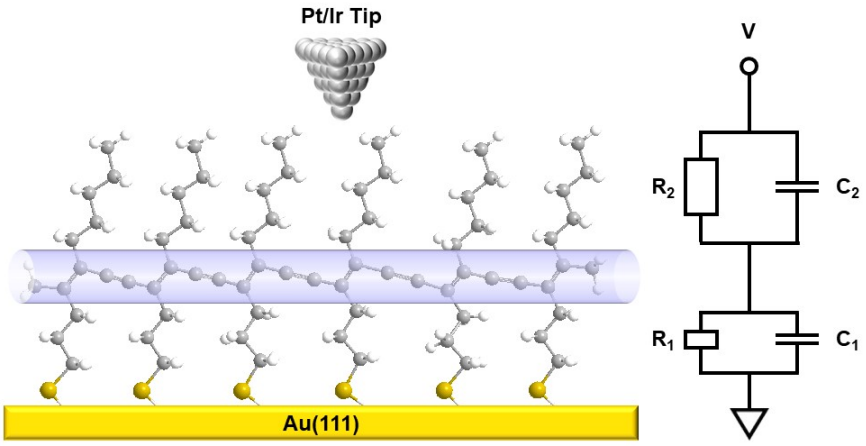

Figure 5.9: Schematic of the nanostructure at the tip-Au interface and the equivalent circuit representing the semiclassical double barrier tunneling junction (DBTJ) model.

land ($\sim$ 1-2 nm) is caused by the quantum confinement effects. For the large C3-poly-DAT island ($\sim$ 20 nm), although we can still observe the Coulomb blockade, due to the reduction of the capacitive charging energy as size increases, the thermal energy (K_{BT}) becomes more dominant during the transport, which leads to a decrease in the Coulomb gap, ultimately extinguishing the Coulomb blockade effects as in the C3-poly-DAT monolayer case.

5.4 Conclusions

In summary, we have explored the diacetylene thiol C3-DAT ($HS(CH_2)_3C{\equiv}C{-}C{\equiv}C(CH_2)_4CH_3$) on Au(111) surfaces before and after polymerization. The formation of C3-DATs and C3-poly-DATs on Au(111) surfaces is confirmed by FTIR, Raman spectroscopy, and XPS. After polymerization, the molecular films exhibit a higher frictional response in AFM due to the reduced local ordering. In addition, small molecular clusters and etch pits have been observed throughout the whole surfaces. STS spectra illustrate similar I-V (dI/dV) for both C3-DAT and C3-poly-DAT SAMs. However, significant size-dependent differences in electronic structures arise for C3-DAT and C3-poly-DAT islands when embedded into dodecanethiolate matrix. The Coulomb blockade effects are revealed and discussed in these C3-poly-DAT nanostructures.

6. SUMMARY AND CONCLUSIONS

This dissertation has explored the evolution of MoS_2 on metal surfaces. The phase transition, accelerated aging, and defect engineering by diacetylenethiolate-based chemisorption of MoS_2 have been discussed in details. The whole first chapter lays the keynote for this work, with a review on the evolution of MoS_2 on Au(111) surfaces. The literature briefly introduces the structure-function properties of 2D-TMDs, strategic fabrication of 2D-MoS_2, phase transition of MoS_2 on Au(111), evolution of MoS_2/Au(111) under accelerated aging conditions, and tuning the electronic properties of MoS_2 by defect engineering of chemisorption. To systematically investigate the structural and chemical transformation of MoS_2 on Au(111) surfaces, a fundamental understanding of the experimental surface science techniques that target specific phenomena is required. In second chapter, the theoretical consideration of the major instrumental techniques was discussed, including scanning tunneling microscopy, atomic force microscopy, Raman spectroscopy, and X-ray photoelectron spectroscopy. Moving forward to Chapter 3-5, three questions have been addressed to understand the evolution of MoS_2 on metal surfaces. I) How does the structure of MoS_2 evolve after deposited on gold substrates. II) How does MoS_2 on Au(111) evolve under accelerated aging conditions. III) What's the mechanical and electronic properties of diacetylene and polydiacetylene SAMs on Au(111) surfaces.

Chapter 3 reported the formation of the coherent single-layer 1H-1T MoS_2 heterostructures by mechanical exfoliation on Au(111), which were chemically homogenous with matched lattices, but showed electronically distinct semiconducting (1H phase) and metallic (1T phase) character. This could be attributed to a combination of lattice strain and charge transfer. The exfoliation approach employed was free from tape residues usually found in many exfoliation methods and yielded single-layer MoS_2 with millimeter size on the Au. Raman spectroscopy, XPS, AFM, STM and STS were employed to elucidate the structural and electronic properties of MoS_2 monolayers on Au substrates. Bubbles in the MoS_2 formed by the trapping of ambient adsorbates beneath the single layer during deposition, were observed and characterized.

The inevitable exposure to environments, has been shown to alter the properties of MoS_2, and significantly affect its tribological performance. In the meantime, solid lubricant coatings made from MoS_2 include interfaces attached to metal substrates, which could strongly modify its chemical and tribological properties. Therefore in Chapter 4, we explored MoS_2 on Au(111) as a model scheme to systematically understand the accelerated aging of MoS_2 on metal surfaces by UV/ozone treatment. The reactive environment, including molecular oxygen, ozone, and atomic oxygen, was very close to the extraterrestrial scenario, especially intended for space applications in LEO environment. We found that, the accelerated aging varies strongly with the layer thickness of MoS_2 sample. After a short time of UV/ozone exposure, single-layer MoS_2 exhibited enhanced reactivity as compared to multi-layer MoS_2. After an extensive time of UV/ozone exposure, while only the top-layer of MoS_2 was oxidized and converted to MoO_3 for multi-layer MoS_2, single-layer MoS_2 was partially etched away, leaving molybdenum sulfate as the final product. This work reveals new insights of the support effect on the accelerated aging of two-dimensional materials, which provides a critical guidance for future design of nanotribological systems.

Because of the intrinsic defects on MoS_2, these undercoordinated surface sites can be identified as potential synthetic starting points for surface modification. Particularly, when functionalized with thiol-terminated molecules, it is possible to tune the electronic properties of MoS_2 comparing to the inertness of complete MoS_2 sheets (either p-dope or n-dope depending on the electronegativity of head groups). In Chapter 5, before directly doping MoS_2, we examined thiol-terminated diacetylenes, especially the polymerized diacetylene thiols on Au(111) surfaces first. The highly conjugated structures, combined with covalent bonds to the MoS_2 substrates, will result in a more rigid feature compared to typical alkanethiols or other thiol-containing molecules. In particular, we explored the diacetylene thiol, $HS(CH_2)_3C{\equiv}C{-}C{\equiv}C(CH_2)_4CH_3$, assembled on Au(111) surfaces before and after polymerization. The monolayers were found to exhibit higher friction following polymerization due to structural changes in the films. Electronically, although I-V (dI/dV) measurements showed similar spectra for both C3-DAT and C3-poly-DAT monolayer films, size-dependent differences in the electronic properties were found to arise for C3-poly-DAT islands of

ca. 10 nm when embedded into a dodecanethiolate matrix, which could be attributed to Coulomb blockade.

REFERENCES

[1] K. Novoselov, D. Jiang, F. Schedin, T. Booth, V. Khotkevich, S. Morozov, and A. Geim, "Two-dimensional atomic crystals," *Proc. Natl. Acad. Sci. U.S.A.*, vol. 102, pp. 10451–10453, 2005.

[2] R. Ma and T. Sasaki, "Nanosheets of oxides and hydroxides: ultimate 2D charge-bearing functional crystallites," *Adv. Mater.*, vol. 22, pp. 5082–5104, 2010.

[3] C. Lee, Q. Li, W. Kalb, X.-Z. Liu, H. Berger, R. W. Carpick, and J. Hone, "Frictional characteristics of atomically thin sheets," *Science*, vol. 328, pp. 76–80, 2010.

[4] I. Song, C. Park, and H. C. Choi, "Synthesis and properties of molybdenum disulphide: from bulk to atomic layers," *RSC Adv.*, vol. 5, pp. 7495–7514, 2015.

[5] X. Huang, Z. Zeng, and H. Zhang, "Metal dichalcogenide nanosheets: preparation, properties and applications," *Chem. Soc. Rev.*, vol. 42, pp. 1934–1946, 2013.

[6] R. Lv, J. A. Robinson, R. E. Schaak, D. Sun, Y. Sun, T. E. Mallouk, and M. Terrones, "Transition metal dichalcogenides and beyond: synthesis, properties, and applications of single-and few-layer nanosheets," *Acc. Chem. Res.*, vol. 48, pp. 56–64, 2014.

[7] M. Chhowalla, H. S. Shin, G. Eda, L.-J. Li, K. P. Loh, and H. Zhang, "the chemistry of two-dimensional layered transition metal dichalcogenide nanosheets," *Nat. Chem.*, vol. 5, p. 263, 2013.

[8] Z. Li, X. Meng, and Z. Zhang, "Recent development on MoS_2-based photocatalysis: a review," *J. Photochem. Photobiol. C*, vol. 35, pp. 39–55, 2017.

[9] Q. H. Wang, K. Kalantar-Zadeh, A. Kis, J. N. Coleman, and M. S. Strano, "Electronics and optoelectronics of two-dimensional transition metal dichalcogenides," *Nat. Nanotechnol.*, vol. 7, p. 699, 2012.

[10] T. Cao, G. Wang, W. Han, H. Ye, C. Zhu, J. Shi, Q. Niu, P. Tan, E. Wang, and B. Liu, "Valley-selective circular dichroism of monolayer molybdenum disulphide," *Nat. Commun.*, vol. 3, p. 887, 2012.

[11] J. Feng, X. Qian, C.-W. Huang, and J. Li, "Strain-engineered artificial atom as a broad-spectrum solar energy funnel," *Nat. Photonics*, vol. 6, no. 12, p. 866, 2012.

[12] S. Kim, A. Konar, W.-S. Hwang, J. H. Lee, J. Lee, J. Yang, C. Jung, H. Kim, J.-B. Yoo, and J.-Y. Choi, "High-mobility and low-power thin-film transistors based on multilayer MoS_2 crystals," *Nat. Commun.*, vol. 3, p. 2018, 2012.

[13] D. Xiao, G.-B. Liu, W. Feng, X. Xu, and W. Yao, "Coupled spin and valley physics in monolayers of MoS_2 and other group-vi dichalcogenides," *Phys. Rev. Lett.*, vol. 108, p. 196802, 2012.

[14] X. Qian, J. Liu, L. Fu, and J. Li, "Quantum spin hall effect in two-dimensional transition metal dichalcogenides," *Science*, p. 1256815, 2014.

[15] D. H. Keum, S. Cho, J. H. Kim, D.-H. Choe, H.-J. Sung, M. Kan, H. Kang, J.-Y. Hwang, S. W. Kim, and H. Yang, "Bandgap opening in few-layered monoclinic $MoTe_2$," *Nat. Phys.*, vol. 11, p. 482, 2015.

[16] S. Tang, C. Zhang, D. Wong, Z. Pedramrazi, H.-Z. Tsai, C. Jia, B. Moritz, M. Claassen, H. Ryu, and S. Kahn, "Quantum spin hall state in monolayer 1T'-WTe_2," *Nat. Phys.*, vol. 13, p. 683, 2017.

[17] S. N. Shirodkar and U. V. Waghmare, "Emergence of ferroelectricity at a metal-semiconductor transition in a 1T monolayer of MoS_2," *Phys. Rev. Lett.*, vol. 112, p. 157601, 2014.

[18] B. K. Miremadi and S. R. Morrison, "High activity catalyst from exfoliated MoS_2," *J. Catal.*, vol. 103, no. 2, pp. 334–345, 1987.

[19] M. Velicky, G. E. Donnelly, W. R. Hendren, S. McFarland, D. Scullion, W. J. DeBenedetti, G. C. Correa, Y. Han, A. J. Wain, and M. A. Hines, "Mechanism of gold-assisted exfolia-

tion of centimeter-sized transition-metal dichalcogenide monolayers," *ACS Nano*, vol. 12, pp. 10463–10472, 2018.

[20] S. B. Desai, S. R. Madhvapathy, M. Amani, D. Kiriya, M. Hettick, M. Tosun, Y. Zhou, M. Dubey, J. W. Ager III, D. Chrzan, *et al.*, "Gold mediated exfoliation of ultralarge optoelectronically perfect monolayers," *Adv. Mater.*, vol. 28, no. 21, pp. 4053–4058, 2016.

[21] J. N. Coleman, M. Lotya, A. ONeill, S. D. Bergin, P. J. King, U. Khan, K. Young, A. Gaucher, S. De, R. J. Smith, *et al.*, "Two-dimensional nanosheets produced by liquid exfoliation of layered materials," *Science*, vol. 331, no. 6017, pp. 568–571, 2011.

[22] R. J. Smith, P. J. King, M. Lotya, C. Wirtz, U. Khan, S. De, A. O'Neill, G. S. Duesberg, J. C. Grunlan, G. Moriarty, *et al.*, "Large-scale exfoliation of inorganic layered compounds in aqueous surfactant solutions," *Adv. Mater.*, vol. 23, no. 34, pp. 3944–3948, 2011.

[23] K. Lee, H.-Y. Kim, M. Lotya, J. N. Coleman, G.-T. Kim, and G. S. Duesberg, "Electrical characteristics of molybdenum disulfide flakes produced by liquid exfoliation," *Adv. Mater.*, vol. 23, no. 36, pp. 4178–4182, 2011.

[24] B. Akesson and K. Paulsson, "Experimental exposure of male volunteers to N-methyl-2-pyrrolidone (NMP): acute effects and pharmacokinetics of NMP in plasma and urine," *Occup. Environ. Med.*, vol. 54, no. 4, pp. 236–240, 1997.

[25] J. Guo, R. Peng, H. Du, Y. Shen, Y. Li, J. Li, and G. Dong, "The application of nano-MoS_2 quantum dots as liquid lubricant additive for tribological behavior improvement," *Nanomaterials*, vol. 10, no. 2, p. 200, 2020.

[26] G. Eda, H. Yamaguchi, D. Voiry, T. Fujita, M. Chen, and M. Chhowalla, "Photoluminescence from chemically exfoliated MoS_2," *Nano Lett.*, vol. 11, pp. 5111–5116, 2011.

[27] Y. Lee, X. Zhang, W. Zhang, M. Chang, C. Lin, K. Chang, Y. Yu, J. T. Wang, C. Chang, and L. Li, "Synthesis of largearea MoS_2 atomic layers with chemical vapor deposition," *Adv. Mater.*, vol. 24, pp. 2320–2325, 2012.

[28] S. G. Sørensen, H. G. Fuchtbauer, A. K. Tuxen, A. S. Walton, and J. V. Lauritsen, "Structure and electronic properties of In Situ synthesized single-layer MoS_2 on a gold surface," *ACS Nano*, vol. 8, pp. 6788–6796, 2014.

[29] K.-K. Liu, W. Zhang, Y.-H. Lee, Y.-C. Lin, M.-T. Chang, C.-Y. Su, C.-S. Chang, H. Li, Y. Shi, H. Zhang, *et al.*, "Growth of large-area and highly crystalline MoS_2 thin layers on insulating substrates," *Nano Lett.*, vol. 12, no. 3, pp. 1538–1544, 2012.

[30] Y.-C. Lin, W. Zhang, J.-K. Huang, K.-K. Liu, Y.-H. Lee, C.-T. Liang, C.-W. Chu, and L.-J. Li, "Wafer-scale MoS_2 thin layers prepared by MoO_3 sulfurization," *Nanoscale*, vol. 4, no. 20, pp. 6637–6641, 2012.

[31] J. Xie, H. Zhang, S. Li, R. Wang, X. Sun, M. Zhou, J. Zhou, X. W. Lou, and Y. Xie, "Defect-rich MoS_2 ultrathin nanosheets with additional active edge sites for enhanced electrocatalytic hydrogen evolution," *Adv. Mater.*, vol. 25, no. 40, pp. 5807–5813, 2013.

[32] M. Wang, G. Li, H. Xu, Y. Qian, and J. Yang, "Enhanced lithium storage performances of hierarchical hollow MoS_2 nanoparticles assembled from nanosheets," *ACS Appl. Mater. Interfaces*, vol. 5, no. 3, pp. 1003–1008, 2013.

[33] H. Ramakrishna Matte, A. Gomathi, A. K. Manna, D. J. Late, R. Datta, S. K. Pati, and C. Rao, "MoS_2 and WS_2 analogues of graphene," *Angew. Chem. Int.*, vol. 49, no. 24, pp. 4059–4062, 2010.

[34] Y. Lu, X. Yao, J. Yin, G. Peng, P. Cui, and X. Xu, "MoS_2 nanoflowers consisting of nanosheets with a controllable interlayer distance as high-performance lithium ion battery anodes," *RSC Adv.*, vol. 5, no. 11, pp. 7938–7943, 2015.

[35] P.-p. Wang, H. Sun, Y. Ji, W. Li, and X. Wang, "Three-dimensional assembly of single-layered MoS_2," *Adv. Mater.*, vol. 26, no. 6, pp. 964–969, 2014.

[36] D. Kong, H. Wang, J. J. Cha, M. Pasta, K. J. Koski, J. Yao, and Y. Cui, "Synthesis of MoS_2 and $MoSe_2$ films with vertically aligned layers," *Nano Lett.*, vol. 13, no. 3, pp. 1341–1347, 2013.

[37] C. Liu, D. Kong, P.-C. Hsu, H. Yuan, H.-W. Lee, Y. Liu, H. Wang, S. Wang, K. Yan, D. Lin, *et al.*, "Rapid water disinfection using vertically aligned MoS_2 nanofilms and visible light," *Nat. Nanotechnol.*, vol. 11, no. 12, p. 1098, 2016.

[38] H. J. Song, S. You, X. H. Jia, and J. Yang, "MoS_2 nanosheets decorated with magnetic Fe_3O_4 nanoparticles and their ultrafast adsorption for wastewater treatment," *Ceram. Int.*, vol. 41, no. 10, pp. 13896–13902, 2015.

[39] M. Bollinger, J. Lauritsen, K. W. Jacobsen, J. K. Nørskov, S. Helveg, and F. Besenbacher, "One-dimensional metallic edge states in MoS_2," *Phys. Rev. Lett.*, vol. 87, p. 196803, 2001.

[40] S. Helveg, J. V. Lauritsen, E. Lægsgaard, I. Stensgaard, J. K. Nørskov, B. Clausen, H. Topsøe, and F. Besenbacher, "Atomic-scale structure of single-layer MoS_2 nanoclusters," *Phys. Rev. Lett.*, vol. 84, p. 951, 2000.

[41] J. Lauritsen, M. Nyberg, J. K. Nørskov, B. Clausen, H. Topsøe, E. Lægsgaard, and F. Besenbacher, "Hydrodesulfurization reaction pathways on MoS_2 nanoclusters revealed by scanning tunneling microscopy," *J. Catal.*, vol. 224, pp. 94–106, 2004.

[42] S. Yasuda, R. Takahashi, R. Osaka, R. Kumagai, Y. Miyata, S. Okada, Y. Hayamizu, and K. Murakoshi, "Out-of-plane strain induced in a moiré superstructure of monolayer MoS_2 and $MoSe_2$ on Au (111)," *Small*, vol. 13, no. 31, p. 1700748, 2017.

[43] G. Z. Magda, J. Pet, G. Dobrik, C. Hwang, L. P. Biró, and L. Tapasztó, "Exfoliation of large-area transition metal chalcogenide single layers," *Sci. Rep.*, vol. 5, p. 14714, 2015.

[44] P. Vancsó, G. Z. Magda, J. Pet, J.-Y. Noh, Y.-S. Kim, C. Hwang, L. P. Biró, and L. Tapasztó, "The intrinsic defect structure of exfoliated MoS_2 single layers revealed by scanning tunneling microscopy," *Sci. Rep.*, vol. 6, p. 29726, 2016.

[45] S. Barja, S. Refaely-Abramson, B. Schuler, D. Y. Qiu, A. Pulkin, S. Wickenburg, H. Ryu, M. M. Ugeda, C. Kastl, C. Chen, *et al.*, "Identifying substitutional oxygen as a prolific point defect in monolayer transition metal dichalcogenides," *Nat. Commun.*, vol. 10, no. 1, pp. 1–8, 2019.

[46] N. Krane, C. Lotze, J. M. Lager, G. Reecht, and K. J. Franke, "Electronic structure and luminescence of quasi-freestanding MoS_2 nanopatches on Au (111)," *Nano Lett.*, vol. 16, no. 8, pp. 5163–5168, 2016.

[47] J. Gao, B. Li, J. Tan, P. Chow, T.-M. Lu, and N. Koratkar, "Aging of transition metal dichalcogenide monolayers," *ACS Nano*, vol. 10, no. 2, pp. 2628–2635, 2016.

[48] J. F. Curry, M. A. Wilson, H. S. Luftman, N. C. Strandwitz, N. Argibay, M. Chandross, M. A. Sidebottom, and B. A. Krick, "Impact of microstructure on MoS_2 oxidation and friction," *ACS Appl. Mater. Interfaces*, vol. 9, no. 33, pp. 28019–28026, 2017.

[49] M. Yamamoto, T. L. Einstein, M. S. Fuhrer, and W. G. Cullen, "Anisotropic etching of atomically thin MoS_2," *J. Phys. Chem. C*, vol. 117, no. 48, pp. 25643–25649, 2013.

[50] J. Wu, H. Li, Z. Yin, H. Li, J. Liu, X. Cao, Q. Zhang, and H. Zhang, "Layer thinning and etching of mechanically exfoliated MoS_2 nanosheets by thermal annealing in air," *Small*, vol. 9, no. 19, pp. 3314–3319, 2013.

[51] D. Lee, J. H. Jang, W. Song, J. Moon, Y. Kim, J. Lee, B. Jeong, and S. Park, "In situ work-function measurement during chemical transformation of MoS_2 to MoO_3 by ambient-pressure X-ray photoelectron spectroscopy," *2D Mater.*, vol. 7, no. 2, p. 025014, 2020.

[52] N. Kang, H. P. Paudel, M. N. Leuenberger, L. Tetard, and S. I. Khondaker, "Photoluminescence quenching in single-layer MoS_2 *via* oxygen plasma treatment," *J. Phys. Chem. C*, vol. 118, no. 36, pp. 21258–21263, 2014.

[53] H. Nan, Z. Wang, W. Wang, Z. Liang, Y. Lu, Q. Chen, D. He, P. Tan, F. Miao, X. Wang, *et al.*, "Strong photoluminescence enhancement of MoS_2 through defect engineering and oxygen bonding," *ACS Nano*, vol. 8, no. 6, pp. 5738–5745, 2014.

[54] S. Kim, M. S. Choi, D. Qu, C. H. Ra, X. Liu, M. Kim, Y. J. Song, and W. J. Yoo, "Effects of plasma treatment on surface properties of ultrathin layered MoS_2," *2D Mater.*, vol. 3, no. 3, p. 035002, 2016.

[55] W. Yang, Q.-Q. Sun, Y. Geng, L. Chen, P. Zhou, S.-J. Ding, and D. W. Zhang, "The integration of sub-10 nm gate oxide on MoS_2 with ultra low leakage and enhanced mobility," *Sci. Rep.*, vol. 5, p. 11921, 2015.

[56] A. Azcatl, S. McDonnell, S. KC, X. Peng, H. Dong, X. Qin, R. Addou, G. I. Mordi, N. Lu, J. Kim, *et al.*, "MoS_2 functionalization for ultra-thin atomic layer deposited dielectrics," *Appl. Phys. Lett.*, vol. 104, no. 11, p. 111601, 2014.

[57] E. P. Nguyen, B. J. Carey, J. Z. Ou, J. van Embden, E. D. Gaspera, A. F. Chrimes, M. J. Spencer, S. Zhuiykov, K. Kalantar-zadeh, and T. Daeneke, "Electronic tuning of 2D MoS_2 through surface functionalization," *Adv. Mater.*, vol. 27, no. 40, pp. 6225–6229, 2015.

[58] D. M. Sim, M. Kim, S. Yim, M.-J. Choi, J. Choi, S. Yoo, and Y. S. Jung, "Controlled doping of vacancy-containing few-layer MoS_2 *via* highly stable thiol-based molecular chemisorption," *ACS Nano*, vol. 9, no. 12, pp. 12115–12123, 2015.

[59] M. Makarova, Y. Okawa, and M. Aono, "Selective adsorption of thiol molecules at sulfur vacancies on MoS_2 (0001), followed by vacancy repair *via* S-C dissociation," *J. Phys. Chem. C*, vol. 116, no. 42, pp. 22411–22416, 2012.

[60] T. Kim, K. C. Chan, and R. M. Crooks, "Polymeric self-assembled monolayers. 4. chemical, electrochemical, and thermal stability of w-functionalized, self-assembled diacetylenic and polydiacetylenic monolayers," *J. Am. Chem. Soc.*, vol. 119, no. 1, pp. 189–193, 1997.

[61] B. Voigtländer, *Scanning probe microscopy: Atomic force microscopy and scanning tunneling microscopy*. Springer, 2015.

[62] A. D. Gottlieb and L. Wesoloski, "Bardeens tunnelling theory as applied to scanning tunnelling microscopy: a technical guide to the traditional interpretation," *Nanotechnology*, vol. 17, no. 8, p. R57, 2006.

[63] C. J. Chen, *Introduction to scanning tunneling microscopy*, vol. 4. Oxford University Press on Demand, 1993.

[64] I. Agilent Technologies, "Agilent 5500 LS AFM/SPM user manual," 2008.

[65] D. A. Skoog, F. J. Holler, and S. R. Crouch, *Principles of instrumental analysis*. Cengage learning, 2017.

[66] C. Fadley, "Basic concepts of x-ray photoelectron spectroscopy," *Electron spectroscopy: theory, techniques and applications*, vol. 2, pp. 1–156, 1978.

[67] K. Siegbahn, *ESCA applied to free molecules*. North-Holland Pub. Co., 1969.

[68] S. Kowalczyk, L. Ley, R. Martin, F. McFeely, and D. Shirley, "Relaxation and final-state structure in XPS of atoms, molecules, and metals," *Faraday Discussions of the Chemical Society*, vol. 60, pp. 7–17, 1975.

[69] D. Shirley, "The effect of atomic and extra-atomic relaxation on atomic binding energies," *Chem. Phys. Lett.*, vol. 16, no. 2, pp. 220–225, 1972.

[70] D. Davis and D. Shirley, "A relaxation correction to core-level binding-energy shifts in small molecules," *Chem. Phys. Lett.*, vol. 15, no. 2, pp. 185–190, 1972.

[71] S. Kowalczyk, L. Ley, R. Pollak, F. McFeely, and D. Shirley, "New multiplet structure in photemission from MnF_2," *Phys. Rev. B*, vol. 7, no. 8, p. 4009, 1973.

[72] Y. Li, K.-A. N. Duerloo, K. Wauson, and E. J. Reed, "Structural semiconductor-to-semimetal phase transition in two-dimensional materials induced by electrostatic gating," *Nat. Commun.*, vol. 7, p. 10671, 2016.

[73] G. Pagona, C. Bittencourt, R. Arenal, and N. Tagmatarchis, "Exfoliated semiconducting pure 2H-MoS_2 and 2H-WS_2 assisted by chlorosulfonic acid," *Chem. Commun.*, vol. 51, pp. 12950–12953, 2015.

[74] N. Liu, P. Kim, J. H. Kim, J. H. Ye, S. Kim, and C. J. Lee, "Large-area atomically thin MoS_2 nanosheets prepared using electrochemical exfoliation," *ACS Nano*, vol. 8, pp. 6902–6910, 2014.

[75] A. Jawaid, D. Nepal, K. Park, M. Jespersen, A. Qualley, P. Mirau, L. F. Drummy, and R. A. Vaia, "Mechanism for liquid phase exfoliation of MoS_2," *Chem. Mater.*, vol. 28, pp. 337–348, 2015.

[76] Z. Lin, Y. Liu, U. Halim, M. Ding, Y. Liu, Y. Wang, C. Jia, P. Chen, X. Duan, and C. Wang, "Solution-processable 2D semiconductors for high-performance large-area electronics," *Nature*, vol. 562, p. 254, 2018.

[77] R. Gordon, D. Yang, E. Crozier, D. Jiang, and R. Frindt, "Structures of exfoliated single layers of WS_2, MoS_2, and $MoSe_2$ in aqueous suspension," *Phys. Rev. B: Condens. Matter*, vol. 65, p. 125407, 2002.

[78] B. Sipos, A. F. Kusmartseva, A. Akrap, H. Berger, L. Forró, and E. Tuti, "From Mott state to superconductivity in 1T-TaS_2," *Nat. Mater.*, vol. 7, p. 960, 2008.

[79] A. Kuc, N. Zibouche, and T. Heine, "Influence of quantum confinement on the electronic structure of the transition metal sulfide TS_2," *Phys. Rev. B: Condens. Matter*, vol. 83, p. 245213, 2011.

[80] R. Holinski and J. Gänsheimer, "A study of the lubricating mechanism of molybdenum disulfide," *Wear*, vol. 19, pp. 329–342, 1972.

[81] W. O. Winer, "Molybdenum disulfide as a lubricant: A review of the fundamental knowledge," *Wear*, vol. 10, pp. 422–452, 1967.

[82] H. Wang, Z. Lu, D. Kong, J. Sun, T. M. Hymel, and Y. Cui, "Electrochemical tuning of MoS_2 nanoparticles on three-dimensional substrate for efficient hydrogen evolution," *ACS Nano*, vol. 8, no. 5, pp. 4940–4947, 2014.

[83] J. Kibsgaard, Z. Chen, B. N. Reinecke, and T. F. Jaramillo, "Engineering the surface structure of MoS_2 to preferentially expose active edge sites for electrocatalysis," *Nat. Mater.*, vol. 11, p. 963, 2012.

[84] Y. Ouyang, C. Ling, Q. Chen, Z. Wang, L. Shi, and J. Wang, "Activating inert basal planes of MoS_2 for hydrogen evolution reaction through the formation of different intrinsic defects," *Chem. Mater.*, vol. 28, pp. 4390–4396, 2016.

[85] Z. Liu, Z. Gao, Y. Liu, M. Xia, R. Wang, and N. Li, "Heterogeneous nanostructure based on 1T-phase MoS_2 for enhanced electrocatalytic hydrogen evolution," *ACS Appl. Mater. Interfaces*, vol. 9, pp. 25291–25297, 2017.

[86] G. Li, D. Zhang, Q. Qiao, Y. Yu, D. Peterson, A. Zafar, R. Kumar, S. Curtarolo, F. Hunte, and S. Shannon, "All the catalytic active sites of MoS_2 for hydrogen evolution," *J. Am. Chem. Soc.*, vol. 138, pp. 16632–16638, 2016.

[87] D. Wang, X. Zhang, S. Bao, Z. Zhang, H. Fei, and Z. Wu, "Phase engineering of a multiphasic 1T/2H MoS_2 catalyst for highly efficient hydrogen evolution," *J. Mater. Chem. A*, vol. 5, pp. 2681–2688, 2017.

[88] H. Wang, Z. Lu, S. Xu, D. Kong, J. J. Cha, G. Zheng, P.-C. Hsu, K. Yan, D. Bradshaw, and F. B. Prinz, "Electrochemical tuning of vertically aligned MoS_2 nanofilms and its application in improving hydrogen evolution reaction," *Proc. Natl. Acad. Sci. U.S.A.*, vol. 110, pp. 19701–19706, 2013.

[89] M. A. Lukowski, A. S. Daniel, F. Meng, A. Forticaux, L. Li, and S. Jin, "Enhanced hydrogen evolution catalysis from chemically exfoliated metallic MoS_2 nanosheets," *J. Am. Chem. Soc.*, vol. 135, pp. 10274–10277, 2013.

[90] X. Geng, Y. Jiao, Y. Han, A. Mukhopadhyay, L. Yang, and H. Zhu, "Freestanding metallic 1T MoS_2 with dual ion diffusion paths as high rate anode for sodiumion batteries," *Adv. Funct. Mater.*, vol. 27, p. 1702998, 2017.

[91] X. Cao, Y. Shi, W. Shi, X. Rui, Q. Yan, J. Kong, and H. Zhang, "Preparation of MoS_2-coated three-dimensional graphene networks for high-performance anode material in lithium-ion batteries," *Small*, vol. 9, pp. 3433–3438, 2013.

[92] K. Chang and W. Chen, "L-cysteine-assisted synthesis of layered MoS_2/graphene composites with excellent electrochemical performances for lithium ion batteries," *ACS Nano*, vol. 5, pp. 4720–4728, 2011.

[93] J. Xiao, D. Choi, L. Cosimbescu, P. Koech, J. Liu, and J. P. Lemmon, "Exfoliated MoS_2 nanocomposite as an anode material for lithium ion batteries," *Chem. Mater.*, vol. 22, pp. 4522–4524, 2010.

[94] F. Cheng, J. Chen, and X. Gou, "MoS_2Ni nanocomposites as catalysts for hydrodesulfurization of thiophene and thiophene derivatives," *Adv. Mater.*, vol. 18, pp. 2561–2564, 2006.

[95] A. Ejigu, I. A. Kinloch, E. Prestat, and R. A. Dryfe, "A simple electrochemical route to metallic phase trilayer MoS_2: Evaluation as electrocatalysts and supercapacitors," *J. Mater. Chem. A*, vol. 5, pp. 11316–11330, 2017.

[96] C. Yang, Z. Chen, I. Shakir, Y. Xu, and H. Lu, "Rational synthesis of carbon shell coated polyaniline/MoS_2 monolayer composites for high-performance supercapacitors," *Nano Res.*, vol. 9, pp. 951–962, 2016.

[97] H. Tang, J. Wang, H. Yin, H. Zhao, D. Wang, and Z. Tang, "Growth of polypyrrole ultrathin films on MoS_2 monolayers as highperformance supercapacitor electrodes," *Adv. Mater.*, vol. 27, pp. 1117–1123, 2015.

[98] C. Guo, J. Pan, H. Li, T. Lin, P. Liu, C. Song, D. Wang, G. Mu, X. Lai, and H. Zhang, "Observation of superconductivity in 1T-MoS_2 nanosheets," *J. Mater. Chem. C*, vol. 5, pp. 10855–10860, 2017.

[99] J. Lu, O. Zheliuk, I. Leermakers, N. F. Yuan, U. Zeitler, K. T. Law, and J. Ye, "Evidence for two-dimensional ising superconductivity in gated MoS_2," *Science*, vol. 350, no. 6266, pp. 1353–1357, 2015.

[100] Y. Saito, Y. Nakamura, M. S. Bahramy, Y. Kohama, J. Ye, Y. Kasahara, Y. Nakagawa, M. Onga, M. Tokunaga, and T. Nojima, "Superconductivity protected by spin-valley locking in ion-gated MoS_2," *Nat. Phys.*, vol. 12, pp. 144–149, 2016.

[101] S. K. Kim, R. Bhatia, T.-H. Kim, D. Seol, J. H. Kim, H. Kim, W. Seung, Y. Kim, Y. H. Lee, and S.-W. Kim, "Directional dependent piezoelectric effect in CVD grown monolayer MoS_2 for flexible piezoelectric nanogenerators," *Nano Energy*, vol. 22, pp. 483–489, 2016.

[102] K. Maity, B. Mahanty, T. K. Sinha, S. Garain, A. Biswas, S. K. Ghosh, S. Manna, S. K. Ray, and D. Mandal, "Two-dimensional piezoelectric MoS_2-modulated nanogenerator and nanosensor made of poly (vinlydine fluoride) nanofiber webs for self-powered electronics and robotics," *Energy Technol.*, vol. 5, pp. 234–243, 2017.

[103] H. Zhu, Y. Wang, J. Xiao, M. Liu, S. Xiong, Z. J. Wong, Z. Ye, Y. Ye, X. Yin, and X. Zhang, "Observation of piezoelectricity in free-standing monolayer MoS_2," *Nat. Nanotechnol.*, vol. 10, p. 151, 2015.

[104] B. Radisavljevic, A. Radenovic, J. Brivio, i. V. Giacometti, and A. Kis, "Single-layer MoS_2 transistors," *Nat. Nanotechnol.*, vol. 6, p. 147, 2011.

[105] N. Krane, C. Lotze, G. Reecht, L. Zhang, A. L. Briseno, and K. J. Franke, "High-resolution vibronic spectra of molecules on molybdenum disulfide allow for rotamer identification," *ACS Nano*, vol. 12, no. 11, pp. 11698–11703, 2018.

[106] G. Reecht, N. Krane, C. Lotze, and K. J. Franke, "π-radical formation by pyrrolic h abstraction of phthalocyanine molecules on molybdenum disulfide," *ACS nano*, vol. 13, p. 70317035, 2019.

[107] S. Huang, X. Ling, L. Liang, J. Kong, H. Terrones, V. Meunier, and M. S. Dresselhaus, "Probing the interlayer coupling of twisted bilayer MoS_2 using photoluminescence spectroscopy," *Nano Lett.*, vol. 14, pp. 5500–5508, 2014.

[108] K. F. Mak, C. Lee, J. Hone, J. Shan, and T. F. Heinz, "Atomically thin MoS_2: a new direct-gap semiconductor," *Phys. Rev. Lett.*, vol. 105, p. 136805, 2010.

[109] O. Lopez-Sanchez, D. Lembke, M. Kayci, A. Radenovic, and A. Kis, "Ultrasensitive photodetectors based on monolayer MoS_2," *Nat. Nanotechnol.*, vol. 8, p. 497, 2013.

[110] S. Huang, L. Liang, X. Ling, A. A. Puretzky, D. B. Geohegan, B. G. Sumpter, J. Kong, V. Meunier, and M. S. Dresselhaus, "Low-frequency interlayer Raman modes to probe interface of twisted bilayer MoS_2," *Nano Lett.*, vol. 16, pp. 1435–1444, 2016.

[111] L. Mattheiss, "Band structures of transition-metal-dichalcogenide layer compounds," *Phys. Rev. B: Condens. Matter*, vol. 8, p. 3719, 1973.

[112] E. Fortin and W. Sears, "Photovoltaic effect and optical absorption in MoS_2," *J. Phys. Chem. Solids*, vol. 43, pp. 881–884, 1982.

[113] H. Hwang, H. Kim, and J. Cho, "MoS_2 nanoplates consisting of disordered graphene-like layers for high rate lithium battery anode materials," *Nano Lett.*, vol. 11, pp. 4826–4830, 2011.

[114] C. Roxlo, R. Chianelli, H. Deckman, A. Ruppert, and P. Wong, "Bulk and surface optical absorption in molybdenum disulfide," *J. Vac. Sci. Technol. A*, vol. 5, pp. 555–557, 1987.

[115] T. Li and G. Galli, "Electronic properties of MoS_2 nanoparticles," *J. Phys. Chem. C*, vol. 111, pp. 16192–16196, 2007.

[116] S. Sze, "Physics of semiconductor deviceswiley eastern," *New York*, 1981.

[117] Y. Wu, J. Xiang, C. Yang, W. Lu, and C. M. Lieber, "Single-crystal metallic nanowires and metal/semiconductor nanowire heterostructures," *Nature*, vol. 430, p. 61, 2004.

[118] L. Ci, L. Song, C. Jin, D. Jariwala, D. Wu, Y. Li, A. Srivastava, Z. Wang, K. Storr, and L. Balicas, "Atomic layers of hybridized boron nitride and graphene domains," *Nat. Mater.*, vol. 9, p. 430, 2010.

[119] K. S. Kim, Y. Zhao, H. Jang, S. Y. Lee, J. M. Kim, K. S. Kim, J.-H. Ahn, P. Kim, J.-Y. Choi, and B. H. Hong, "Large-scale pattern growth of graphene films for stretchable transparent electrodes," *Nature*, vol. 457, p. 706, 2009.

[120] Y. Shi, W. Zhou, A.-Y. Lu, W. Fang, Y.-H. Lee, A. L. Hsu, S. M. Kim, K. K. Kim, H. Y. Yang, and L.-J. Li, "Van der Waals epitaxy of MoS_2 layers using graphene as growth templates," *Nano Lett.*, vol. 12, pp. 2784–2791, 2012.

[121] J. C. Hill, A. T. Landers, and J. A. Switzer, "An electrodeposited inhomogeneous metal-insulatorsemiconductor junction for efficient photoelectrochemical water oxidation," *Nat. Mater.*, vol. 14, p. 1150, 2015.

[122] F. Xiong, H. Wang, X. Liu, J. Sun, M. Brongersma, E. Pop, and Y. Cui, "Li intercalation in MoS_2: In situ observation of its dynamics and tuning optical and electrical properties," *Nano. Lett.*, vol. 15, pp. 6777–6784, 2015.

[123] A. N. Enyashin, L. Yadgarov, L. Houben, I. Popov, M. Weidenbach, R. Tenne, M. Bar-Sadan, and G. Seifert, "New route for stabilization of 1T-WS_2 and MoS_2 phases," *J. Phys. Chem. C*, vol. 115, pp. 24586–24591, 2011.

[124] G. Gao, Y. Jiao, F. Ma, Y. Jiao, E. Waclawik, and A. Du, "Charge mediated semiconducting-to-metallic phase transition in molybdenum disulfide monolayer and hydrogen evolution reaction in new 1T phase," *J. Phys. Chem. C*, vol. 119, pp. 13124–13128, 2015.

[125] S. Song, D. H. Keum, S. Cho, D. Perello, Y. Kim, and Y. H. Lee, "Room temperature semiconductor-metal transition of $MoTe_2$ thin films engineered by strain," *Nano Lett.*, vol. 16, pp. 188–193, 2015.

[126] J. Zhu, Z. Wang, H. Yu, N. Li, J. Zhang, J. Meng, M. Liao, J. Zhao, X. Lu, and L. Du, "Argon plasma induced phase transition in monolayer MoS_2," *J. Am. Chem. Soc.*, vol. 139, pp. 10216–10219, 2017.

[127] S. Cho, S. Kim, J. H. Kim, J. Zhao, J. Seok, D. H. Keum, J. Baik, D.-H. Choe, K. J. Chang, and K. Suenaga, "Phase patterning for ohmic homojunction contact in $MoTe_2$," *Science*, vol. 349, no. 6248, pp. 625–628, 2015.

[128] X. Ling, Y.-H. Lee, Y. Lin, W. Fang, L. Yu, M. S. Dresselhaus, and J. Kong, "Role of the seeding promoter in MoS_2 growth by chemical vapor deposition," *Nano Lett.*, vol. 14, pp. 464–472, 2014.

[129] X. Wang, H. Feng, Y. Wu, and L. Jiao, "Controlled synthesis of highly crystalline MoS_2 flakes by chemical vapor deposition," *J. Am. Chem. Soc.*, vol. 135, pp. 5304–5307, 2013.

[130] H. Li, J. Wu, Z. Yin, and H. Zhang, "Preparation and applications of mechanically exfoliated single-layer and multilayer MoS_2 and WSe_2 nanosheets," *Acc. Chem. Res.*, vol. 47, pp. 1067–1075, 2014.

[131] C. Tsai, F. Abild-Pedersen, and J. K. Nørskov, "Tuning the MoS_2 edge-site activity for hydrogen evolution *via* support interactions," *Nano Lett.*, vol. 14, pp. 1381–1387, 2014.

[132] H. Häkkinen, "The gold sulfur interface at the nanoscale," *Nat. Chem.*, vol. 4, p. 443, 2012.

[133] S. B. Desai, S. R. Madhvapathy, M. Amani, D. Kiriya, M. Hettick, M. Tosun, Y. Zhou, M. Dubey, J. W. Ager III, and D. Chrzan, "Goldmediated exfoliation of ultralarge optoelectronicallyperfect monolayers," *Adv. Mater.*, vol. 28, pp. 4053–4058, 2016.

[134] M. Buscema, G. A. Steele, H. S. van der Zant, and A. Castellanos-Gomez, "The effect of the substrate on the Raman and photoluminescence emission of single-layer MoS_2," *Nano Res.*, vol. 7, pp. 561–571, 2014.

[135] X. S. Chu, A. Yousaf, D. O. Li, A. A. Tang, A. Debnath, D. Ma, A. A. Green, E. J. Santos, and Q. H. Wang, "Direct covalent chemical functionalization of unmodified two-dimensional molybdenum disulfide," *Chem. Mater.*, vol. 30, pp. 2112–2128, 2018.

[136] S. P. Koenig, N. G. Boddeti, M. L. Dunn, and J. S. Bunch, "Ultrastrong adhesion of graphene membranes," *Nat. Nanotechnol.*, vol. 6, p. 543, 2011.

[137] S. Rentenberger, A. Vollmer, E. Zojer, R. Schennach, and N. Koch, "UV/ozone treated au for air-stable, low hole injection barrier electrodes in organic electronics," *J. Appl. Phys.*, vol. 100, p. 053701, 2006.

[138] D. A. Sanchez, Z. Dai, P. Wang, A. Cantu-Chavez, C. J. Brennan, R. Huang, and N. Lu, "Mechanics of spontaneously formed nanoblisters trapped by transferred 2d crystals," *Proc. Natl. Acad. Sci. U. S. A.*, vol. 115, no. 31, pp. 7884–7889, 2018.

[139] J. Verble and T. Wieting, "Lattice mode degeneracy in MoS_2 and other layer compounds," *Phys. Rev. Lett.*, vol. 25, p. 362, 1970.

[140] J. Verble, T. Wietling, and P. Reed, "Rigid-layer lattice vibrations and Van der Waals bonding in hexagonal MoS_2," *Solid State Commun.*, vol. 11, pp. 941–944, 1972.

[141] Y. Zhao, X. Luo, H. Li, J. Zhang, P. T. Araujo, C. K. Gan, J. Wu, H. Zhang, S. Y. Quek, and M. S. Dresselhaus, "Interlayer breathing and shear modes in few-trilayer MoS_2 and WSe_2," *Nano Lett.*, vol. 13, pp. 1007–1015, 2013.

[142] H. Li, Q. Zhang, C. C. R. Yap, B. K. Tay, T. H. T. Edwin, A. Olivier, and D. Baillargeat, "From bulk to monolayer MoS_2: evolution of Raman scattering," *Adv. Funct. Mater.*, vol. 22, pp. 1385–1390, 2012.

[143] C. Lee, H. Yan, L. E. Brus, T. F. Heinz, J. Hone, and S. Ryu, "Anomalous lattice vibrations of single-and few-layer MoS_2," *ACS Nano*, vol. 4, pp. 2695–2700, 2010.

[144] B. Mrstik, R. Kaplan, T. Reinecke, M. Van Hove, and S. Tong, "Surface-structure determination of the layered compounds MoS_2 and $NbSe_2$ by low-energy electron diffraction," *Phys. Rev. B: Condens. Matter*, vol. 15, p. 897, 1977.

[145] C. Rice, R. Young, R. Zan, U. Bangert, D. Wolverson, T. Georgiou, R. Jalil, and K. Novoselov, "Raman-scattering measurements and first-principles calculations of strain-induced phonon shifts in monolayer MoS_2," *Phys. Rev. B*, vol. 87, p. 081307, 2013.

[146] C. Zhu, G. Wang, B. Liu, X. Marie, X. Qiao, X. Zhang, X. Wu, H. Fan, P. Tan, and T. Amand, "Strain tuning of optical emission energy and polarization in monolayer and bilayer MoS_2," *Phys. Rev. B*, vol. 88, p. 121301, 2013.

[147] G. H. Ahn, M. Amani, H. Rasool, D.-H. Lien, J. P. Mastandrea, J. W. Ager III, M. Dubey, D. C. Chrzan, A. M. Minor, and A. Javey, "Strain-engineered growth of two-dimensional materials," *Nat. Commun.*, vol. 8, p. 608, 2017.

[148] S. S. Grønborg, S. Ulstrup, M. Bianchi, M. Dendzik, C. E. Sanders, J. V. Lauritsen, P. Hofmann, and J. A. Miwa, "Synthesis of epitaxial single-layer MoS_2 on Au(111)," *Langmuir*, vol. 31, pp. 9700–9706, 2015.

[149] H. G. Füchtbauer, A. K. Tuxen, P. G. Moses, H. Topsøe, F. Besenbacher, and J. V. Lauritsen, "Morphology and atomic-scale structure of single-layer WS_2 nanoclusters," *Phys. Chem. Chem. Phys.*, vol. 15, pp. 15971–15980, 2013.

[150] J. Lu, D.-L. Bao, K. Qian, S. Zhang, H. Chen, X. Lin, S.-X. Du, and H.-J. Gao, "Identifying and visualizing the edge terminations of single-layer $MoSe_2$ island epitaxially grown on Au(111)," *ACS Nano*, vol. 11, pp. 1689–1695, 2017.

[151] S. B. Desai, G. Seol, J. S. Kang, H. Fang, C. Battaglia, R. Kapadia, J. W. Ager, J. Guo, and A. Javey, "Strain-induced indirect to direct bandgap transition in multilayer WSe_2," *Nano Lett.*, vol. 14, pp. 4592–4597, 2014.

[152] M. Bollinger, K. W. Jacobsen, and J. K. Nørskov, "Atomic and electronic structure of MoS_2 nanoparticles," *Phys. Rev. B: Condens. Matter*, vol. 67, p. 085410, 2003.

[153] A. Bruix, J. A. Miwa, N. Hauptmann, D. Wegner, S. Ulstrup, S. S. Grønborg, C. E. Sanders, M. Dendzik, A. G. abo, and M. Bianchi, "Single-layer MoS_2 on Au(111): Band gap renormalization and substrate interaction," *Phys. Rev. B: Condens. Matter*, vol. 93, p. 165422, 2016.

[154] A. Blumberg, U. Keshet, I. Zaltsman, and O. Hod, "Interlayer registry to determine the sliding potential of layered metal dichalcogenides: the case of 2H-MoS_2," *J. Phys. Chem. Lett.*, vol. 3, no. 15, pp. 1936–1940, 2012.

[155] A. K. Rappe and W. A. Goddard III, "Charge equilibration for molecular dynamics simulations," *J. Phys. Chem.*, vol. 95, no. 8, pp. 3358–3363, 1991.

[156]

[157] K. E. Dungey, M. D. Curtis, and J. E. Penner-Hahn, "Structural characterization and thermal stability of MoS_2 intercalation compounds," *Chem. Mater.*, vol. 10, pp. 2152–2161, 1998.

[158] Y. Cheng, A. Nie, Q. Zhang, L.-Y. Gan, R. Shahbazian-Yassar, and U. Schwingenschlogl, "Origin of the phase transition in lithiated molybdenum disulfide," *ACS Nano*, vol. 8, pp. 11447–11453, 2014.

[159] S. Kretschmer, H.-P. Komsa, P. Bøggild, and A. V. Krasheninnikov, "Structural transformations in two-dimensional transition-metal dichalcogenide MoS_2 under an electron beam: insights from first-principles calculations," *J. Phys. Chem. Lett.*, vol. 8, no. 13, pp. 3061–3067, 2017.

[160] K.-A. N. Duerloo, Y. Li, and E. J. Reed, "Structural phase transitions in two-dimensional Mo-and W-dichalcogenide monolayers," *Nat. Commun.*, vol. 5, no. 1, pp. 1–9, 2014.

[161] D. A. Sanchez, Z. Dai, P. Wang, A. Cantu-Chavez, C. J. Brennan, R. Huang, and N. Lu, "Mechanics of spontaneously formed nanoblisters trapped by transferred 2D crystals," *Proc. Natl. Acad. Sci. U.S.A.*, vol. 115, pp. 7884–7889, 2018.

[162] G. Eda, T. Fujita, H. Yamaguchi, D. Voiry, M. Chen, and M. Chhowalla, "Coherent atomic and electronic heterostructures of single-layer MoS_2," *ACS Nano*, vol. 6, pp. 7311–7317, 2012.

[163] P. Fleischauer and M. Hilton, "Applications of space tribology in the USA," *Tribol. Int.*, vol. 23, no. 2, pp. 135–139, 1990.

[164] J. Cross, J. Martin, L. Pope, and S. Koontz, "Atomic oxygen-MoS_2 chemical interactions," *Surf. Coat. Technol.*, vol. 42, no. 1, pp. 41–48, 1990.

[165] L. Cheng, X. Qin, A. T. Lucero, A. Azcatl, J. Huang, R. M. Wallace, K. Cho, and J. Kim, "Atomic layer deposition of a high-k dielectric on MoS_2 using trimethylaluminum and ozone," *ACS Appl. Mater. Interfaces*, vol. 6, no. 15, pp. 11834–11838, 2014.

[166] C. Pritchard and J. Midgley, "The effect of humidity on the friction and life of unbonded molybdenum disulphide films," *Wear*, vol. 13, no. 1, pp. 39–50, 1969.

[167] H. Khare and D. Burris, "Surface and subsurface contributions of oxidation and moisture to room temperature friction of molybdenum disulfide," *Tribol. Lett.*, vol. 53, no. 1, pp. 329–336, 2014.

[168] C. Jung, H. I. Yang, and W. Choi, "Effect of ultraviolet-ozone treatment on MoS_2 monolayers: Comparison of chemical-vapor-deposited polycrystalline thin films and mechanically exfoliated single crystal flakes," *Nanoscale Res. Lett.*, vol. 14, no. 1, pp. 1–8, 2019.

[169] J. Yang, S. Kim, W. Choi, S. H. Park, Y. Jung, M.-H. Cho, and H. Kim, "Improved growth behavior of atomic-layer-deposited high-k dielectrics on multilayer MoS_2 by oxygen plasma pretreatment," *ACS Appl. Mater. Interfaces*, vol. 5, no. 11, pp. 4739–4744, 2013.

[170] H. Zhu, X. Qin, L. Cheng, A. Azcatl, J. Kim, and R. M. Wallace, "Remote plasma oxidation and atomic layer etching of mos_2," *ACS Appl. Mater. Interfaces*, vol. 8, no. 29, pp. 19119–19126, 2016.

[171] H. I. Yang, S. Park, and W. Choi, "Modification of the optoelectronic properties of two-dimensional MoS_2 crystals by ultraviolet-ozone treatment," *Appl. Surf. Sci.*, vol. 443, pp. 91–96, 2018.

[172] S. Park, S. Y. Kim, Y. Choi, M. Kim, H. Shin, J. Kim, and W. Choi, "Interface properties of atomic-layer-deposited Al_2O_3 thin films on ultraviolet/ozone-treated multilayer MoS_2 crystals," *ACS Appl. Mater. Interfaces*, vol. 8, no. 18, pp. 11189–11193, 2016.

[173] Q. Van Le, T. P. Nguyen, H. W. Jang, and S. Y. Kim, "The use of UV/ozone-treated MoS_2 nanosheets for extended air stability in organic photovoltaic cells," *Phys. Chem. Chem. Phys.*, vol. 16, no. 26, pp. 13123–13128, 2014.

[174] J. Panitz, L. Pope, J. Lyons, and D. Staley, "The tribological properties of MoS_2 coatings in vacuum, low relative humidity, and high relative humidity environments," *J. Vac. Sci. Tech. A: Vacuum, Surfaces, and Films*, vol. 6, no. 3, pp. 1166–1170, 1988.

[175] C. Donnet, J. Martin, T. Le Mogne, and M. Belin, "Super-low friction of MoS_2 coatings in various environments," *Tribol. Int.*, vol. 29, no. 2, pp. 123–128, 1996.

[176] M. Tagawa, M. Muromoto, S. Hachiue, K. Yokota, N. Ohmae, K. Matsumoto, and M. Suzuki, "Hyperthermal atomic oxygen interaction with MoS_2 lubricants and relevance to space environmental effects in low earth orbit–effects on friction coefficient and wear-life," *Tribol. Lett.*, vol. 18, no. 4, pp. 437–443, 2005.

[177] P. Blake, E. Hill, A. Castro Neto, K. Novoselov, D. Jiang, R. Yang, T. Booth, and A. Geim, "Making graphene visible," *Appl. Phys. Lett.*, vol. 91, no. 6, p. 063124, 2007.

[178] L. M. Farigliano, P. A. Paredes-Olivera, and E. M. Patrito, "Initial steps of oxidative etching of MoS_2 Basal Plane Induced by O_2," *J. Phys. Chem. C*, 2020.

[179] Y. Shi, J. Wang, C. Wang, T.-T. Zhai, W.-J. Bao, J.-J. Xu, X.-H. Xia, and H.-Y. Chen, "Hot electron of Au nanorods activates the electrocatalysis of hydrogen evolution on MoS_2 nanosheets," *J. Am. Chem. Soc.*, vol. 137, no. 23, pp. 7365–7370, 2015.

[180] R. Bar-Ziv, P. Ranjan, A. Lavie, A. Jain, S. Garai, A. Bar Hen, R. Popovitz-Biro, R. Tenne, R. Arenal, A. Ramasubramaniam, *et al.*, "Au-MoS_2 hybrids as hydrogen evolution electrocatalysts," *ACS Appl. Energy Mater.*, vol. 2, no. 8, pp. 6043–6050, 2019.

[181] T. Wang, J. Zhuo, Y. Chen, K. Du, P. Papakonstantinou, Z. Zhu, Y. Shao, and M. Li, "Synergistic catalytic effect of MoS_2 nanoparticles supported on gold nanoparticle films for a highly efficient oxygen reduction reaction," *ChemCatChem*, vol. 6, no. 7, pp. 1877–1881, 2014.

[182] J. F. Moulder, "Handbook of X-ray photoelectron spectroscopy," *Physical electronics*, pp. 230–232, 1995.

[183] M. Anwar, C. Hogarth, and R. Bulpett, "Effect of substrate temperature and film thickness on the surface structure of some thin amorphous films of MoO_3 studied by X-ray photoelectron spectroscopy (ESCA)," *J. Mater. Sci.*, vol. 24, no. 9, pp. 3087–3090, 1989.

[184] F. Werfel and E. Minni, "Photoemission study of the electronic structure of Mo and Mo oxides," *J. of Phys. C: Solid State Phys.*, vol. 16, no. 31, p. 6091, 1983.

[185] R. Schlaf, O. Lang, C. Pettenkofer, and W. Jaegermann, "Band lineup of layered semiconductor heterointerfaces prepared by van der Waals epitaxy: Charge transfer correction term for the electron affinity rule," *J. of Appl. Phys.*, vol. 85, no. 5, pp. 2732–2753, 1999.

[186] M. R. Islam, N. Kang, U. Bhanu, H. P. Paudel, M. Erementchouk, L. Tetard, M. N. Leuenberger, and S. I. Khondaker, "Tuning the electrical property via defect engineering of single layer MoS_2 by oxygen plasma," *Nanoscale*, vol. 6, no. 17, pp. 10033–10039, 2014.

[187] B. C. Windom, W. Sawyer, and D. W. Hahn, "A Raman spectroscopic study of MoS_2 and MoO_3: applications to tribological systems," *Tribol. Lett.*, vol. 42, no. 3, pp. 301–310, 2011.

[188] S. Ross and A. Sussman, "Surface oxidation of molybdenum disulfide," *J. Phys. Chem.*, vol. 59, no. 9, pp. 889–892, 1955.

[189] J. M. Tour, "Molecular electronics. synthesis and testing of components," *Acc. Chem. Res.*, vol. 33, no. 11, pp. 791–804, 2000.

[190] C. Joachim, J. K. Gimzewski, and Aviram, "Electronics using hybrid-molecular and monomolecular devices," *Nature*, vol. 408, no. 6812, p. 541548, 2000.

[191] A. E. Schuckman, B. W. Ewers, L. H. Yu, J. P. Tome, L. M. Perez, C. M. Drain, J. G. Kushmerick, and J. D. Batteas, "Utilizing nearest-neighbor interactions to alter charge transport mechanisms in molecular assemblies of porphyrins on surfaces," *J. Phys. Chem. C*, vol. 119, no. 24, pp. 13569–13579, 2015.

[192] A. Ulman, "Formation and structure of self-assembled monolayers," *Chem. Rev.*, vol. 96, no. 4, pp. 1533–1554, 1996.

[193] A. Pawlicki, A. Vilan, M. Jurow, C. M. M. Drain, and J. D. Batteas, "The influence of nearest-neighbour interactions and assembly dynamics on the transport properties of porphyrin supramolecular assemblies on Au(111)," *Faraday Discuss.*, vol. 204, no. 2017, pp. 349–366, 2017.

[194] A. Ugur, F. Katmis, M. Li, L. Wu, Y. Zhu, K. K. Varanasi, and K. K. Gleason, "Low-dimensional conduction mechanisms in highly conductive and transparent conjugated polymers," *Adv. Mater.*, vol. 27, no. 31, pp. 4604–4610, 2015.

[195] L. Dou, Y. Liu, Z. Hong, G. Li, and Y. Yang, "Low-bandgap near-IR conjugated polymers/molecules for organic electronics," *Chem. Rev.*, vol. 115, no. 23, pp. 12633–12665, 2015.

[196] K. Saranya, M. Rameez, and A. Subramania, "Developments in conducting polymer based counter electrodes for dye-sensitized solar cells-an overview," *Eur. Polym. J.*, vol. 66, no. 2015, pp. 207–227, 2015.

[197] M. Cai, M. D. Mowery, H. Menzel, and C. E. Evans, "Fabrication of extended conjugation length polymers within diacetylene monolayers on Au surfaces: Influence of UV exposure time," *Langmuir*, vol. 15, no. 4, pp. 1215–1222, 1999.

[198] C. E. Evans, A. C. Smith, D. J. Burnett, A. L. Marsh, D. A. Fischer, and J. L. Gland, "Polymer conversion measurement of diacetylene-containing thin films and monolayers using soft X-ray fluorescence spectroscopy," *J. Phys. Chem. B*, vol. 106, no. 35, pp. 9036–9043, 2002.

[199] H. Menzel, S. Horstmann, M. Mowery, M. Cai, and C. Evans, "Diacetylene polymerization in self-assembled monolayers: influence of the odd/even nature of the methylene spacer," *Polymer*, vol. 41, no. 22, pp. 8113–8119, 2000.

[200] D. Batchelder, S. Evans, T. Freeman, L. Häussling, H. Ringsdorf, and H. Wolf, "Self-assembled monolayers containing polydiacetylenes," *J. Am. Chem. Soc.*, vol. 116, no. 3, pp. 1050–1053, 1994.

[201] T. Kim, Q. Ye, L. Sun, K. C. Chan, and R. M. Crooks, "Polymeric self-assembled monolayers. 5. synthesis and characterization of w-functionalized, self-assembled diacetylenic and polydiacetylenic monolayers," *Langmuir*, vol. 12, no. 25, pp. 6065–6073, 1996.

[202] K. C. Chan, T. Kim, J. K. Schoer, and R. M. Crooks, "Polymeric self-assembled monolayers. 3. pattern transfer by use of photolithography, electrochemical methods, and an ultrathin,

self-assembled diacetylenic resist," *J. Am. Chem. Soc.*, vol. 117, no. 21, pp. 5875–5876, 1995.

[203] M. D. Mowery and C. E. Evans, "Steric and substrate mediation of polymers formed within single molecular layers," *J. Phys. Chem. B*, vol. 101, no. 42, pp. 8513–8519, 1997.

[204] H. Menzel, M. D. Mowery, M. Cai, and C. E. Evans, "Vertical positioning of internal molecular scaffolding within a single molecular layer," *J. Phys. Chem. B*, vol. 102, no. 47, pp. 9550–9556, 1998.

[205] H. Menzel, M. D. Mowery, M. Cai, and C. E. Evans, "Surface-confined nanoparticles as substrates for photopolymerizable selfassembled monolayers," *Adv. Mater.*, vol. 11, no. 2, pp. 131–134, 1999.

[206] H. Menzel, M. D. Mowery, M. Cai, and C. E. Evans, "Fabrication of noncovalent and covalent internal scaffolding in monolayer assemblies using diacetylenes," *Macromolecules*, vol. 32, no. 13, pp. 4343–4350, 1999.

[207] N. D. K. Bhupathiraju, M. Sayeedi, W. Rizvi, S. Singh, J. D. Batteas, and C. M. Drain, "Practical, high-yield synthesis of thiol-terminated diacetylenes for formation of conductive monolayers," *Tetrahedron Lett.*, vol. 59, no. 40, pp. 3629–3631, 2018.

[208] J. E. Sader, I. Larson, P. Mulvaney, and L. R. White, "Method for the calibration of atomic force microscope cantilevers," *Rev. Sci. Instrum.*, vol. 66, no. 7, pp. 3789–3798, 1995.

[209] D. B. Asay, E. Hsiao, and S. H. Kim, "Corrected direct force balance method for atomic force microscopy lateral force calibration," *Rev. Sci. Instrum.*, vol. 80, no. 6, p. 066101, 2009.

[210] R. Snyder and J. Schachtschneider, "Vibrational analysis of the n-paraffins: assignments of infrared bands in the spectra of C_3H_8 through n-$C_{19}H_{40}$," *Spectrochim. Acta*, vol. 19, no. 1, pp. 85–116, 1963.

[211] R. Snyder, S. Hsu, and S. Krimm, "Vibrational spectra in the C-H stretching region and the structure of the polymethylene chain," *Spectrochim.*, vol. 34, no. 4, pp. 395–406, 1978.

[212] R. Snyder, H. Strauss, and C. Elliger, "Carbon-hydrogen stretching modes and the structure of n-alkyl chains. 1. long, disordered chains," *J. Phys. Chem.*, vol. 86, no. 26, pp. 5145–5150, 1982.

[213] O. Cavalleri, M. Prato, A. Chincarini, R. Rolandi, M. Canepa, A. Gliozzi, M. Alloisio, L. Lavagnino, C. Cuniberti, and C. DellErba, "Self-assembled monolayers of a novel diacetylene on gold," *Appl. Surf. Sci.*, vol. 246, no. 4, pp. 403–408, 2005.

[214] A. Lio, D. Charych, and M. Salmeron, "Comparative atomic force microscopy study of the chain length dependence of frictional properties of alkanethiols on gold and alkylsilanes on mica," *J. Phys. Chem. B*, vol. 101, no. 19, pp. 3800–3805, 1997.

[215] M. D. Mowery, S. Kopta, D. F. Ogletree, M. Salmeron, and C. E. Evans, "Structural manipulation of the frictional properties of linear polymers in single molecular layers," *Langmuir*, vol. 15, no. 15, pp. 5118–5122, 1999.

[216] A. Lio, A. Reichert, J. Nagy, M. Salmeron, and D. Charych, "Atomic force microscope study of chromatic transitions in polydiacetylene thin films," *J. Vac. Sci. Technol. B*, vol. 14, no. 2, pp. 1481–1485, 1996.

[217] A. Lio, A. Reichert, D. J. Ahn, J. O. Nagy, M. Salmeron, and D. H. Charych, "Molecular imaging of thermochromic carbohydrate-modified polydiacetylene thin films," *Langmuir*, vol. 13, no. 24, pp. 6524–6532, 1997.

[218] G. Poirier and E. Pylant, "The self-assembly mechanism of alkanethiols on Au (111)," *Science*, vol. 272, no. 5265, pp. 1145–1148, 1996.

[219] D. J. Trevor, C. E. Chidsey, and D. N. Loiacono, *In situ scanning-tunneling-microscope observation of roughening, annealing, and dissolution of gold (111) in an electrochemical cell*, pp. 209–212. Springer, 1989.

[220] F. Sette, T. Hashizume, F. Comin, A. MacDowell, and P. Citrin, "Coverage and chemical dependence of adsorbate-induced bond weakening in metal substrate surfaces," *Phys. Rev. Lett.*, vol. 61, no. 12, pp. 1384–1387, 1988.

[221] G. Yang and G.-y. Liu, "New insights for self-assembled monolayers of organothiols on Au(111) revealed by scanning tunneling microscopy," *J. Phys. Chem. B*, vol. 107, no. 34, pp. 8746–8759, 2003.

[222] A. Hanna and M. Tinkham, "Variation of the coulomb staircase in a two-junction system by fractional electron charge," *Phys. Rev. B*, vol. 44, no. 11, p. 5919, 1991.

[223] M. Amman, R. Wilkins, E. Ben-Jacob, P. Maker, and R. Jaklevic, "Analytic solution for the current-voltage characteristic of two mesoscopic tunnel junctions coupled in series," *Phys. Rev. B*, vol. 43, no. 1, p. 1146, 1991.